

Micromechanical and Three-Dimensional Microstructural Characterization of Nanoporous Gold-Epoxy Composites

Vom Promotionsausschuss der
Technischen Universität Hamburg-Harburg
zur Erlangung des akademischen Grades
Doktor-Ingenieur (Dr.-Ing.)
genehmigte Dissertation

von
Kaixiong Hu

aus
Wuhan, China
2017

Gutachtern der Dissertation:

Prof. Dr. Erica Lilleodden

*Institute of Materials Research, Materials Mechanics
Helmholtz-Zentrum Geesthacht, Germany.*

Prof. Dr. Cynthia Volkert

*Institute for Materials Physics
University of Göttingen, Germany.*

Vorsitzender des Prüfungsausschusses:

Prof. Dr.-Ing. habil. Bodo Fiedler

*Institute of Polymer Composites
Hamburg University of Technology, Germany.*

Tag der mündlichen Prüfung:

19th January 2017

Online Veröffentlichung durch TUBdok der TUHH:

[urn:nbn:de:gbv:830-88215433](https://nbn-resolving.org/urn:nbn:de:gbv:830-88215433)

Acknowledgements

I would like to express my sincere gratitude to all the people who encouraged and supported me during the last couple of years for my PhD studies. Without their guidance and support, the success of this thesis would not be possible.

First and foremost I would like to sincerely thank my supervisor Prof. Erica Lilleodden, who led me into the fields of Micromechanics and 3D Materials Science, for the precious and continuous support, the scientific guidance and training, the encouragement and the freedom I was given during my PhD period. Her enthusiasm, inspiration and scientific attitude will have a long-lasting impact on my future career.

I would like to express my deep gratitude to Dr. Markus Ziehmer, who is my unofficial supervisor. We worked together closely for over 4 years. His serious scientific attitude and the encouragement during tough times in my PhD deeply infected and inspired me. I was really touched when he said to me he was so happy that I successfully finished my PhD.

I also would like to express my deep acknowledgement to Prof. Dr.-Ing. Norbert Huber at the Institute of Materials Research in Helmholtz-Zentrum Geesthacht for all the supports during my PhD period. I appreciate the opportunity of working in Germany he offered me 5 years ago when I was in China. I appreciate the fruitful discussions with him, especially for FEM simulations. Many thanks to him for taking care of my future career as well.

My particular thanks to Prof. Cynthia A. Volkert at the Institute for Materials Physics in the University of Göttingen for agreeing to review this work and for her valuable suggestions regarding the completion of this study.

I would like to thank all my colleagues in the department of Experimental Materials Mechanics in Helmholtz-Zentrum Geesthacht for their warmth, encouragement and friendship. Thanks to them for giving me help and for sharing their knowledge.

I gratefully acknowledge to the collaboration with the Institut für Werkstoffphysik und Werkstofftechnologie in Hamburg University of Technology. Thanks to the support of Prof. Dr.-Ing. Jörg Weißmüller and Dr. Ke Wang for the sample synthesis.

I am grateful for the time spent with all my colleagues in Helmholtz-Zentrum

Geesthacht and Integriertes Graduiertenkolleg (MGK) of SFB 986 project, and all my Chinese friends in Germany.

Lastly but most importantly, I express my profound thanks to my family for the patience, support and understanding.

Financial support from the German Research Foundation (DFG) through SFB 986 “Tailor–Made Multi–Scale Materials Systems–M³” project B4 is gratefully acknowledged.

Abstract

Nanoporous gold (npg), a bicontinuous network of nanoscale gold ligaments and pores, displays tunable mechanical behavior through the variation of internal length-scales. However, it is severely limited by its lack of ductility in tension. By infiltrating the porous structure with epoxy, a composite material with enhanced tensile ductility and flow stress is achieved. The present work aims at a three-fold investigation of micromechanical behavior, mechanisms of deformation and failure of the npg-epoxy composite, focusing on 3D microstructural characterization, finite element simulation and micromechanical testing.

In order to understand the composite microstructure, high resolution 3D reconstructions of the npg ligament network were achieved with focused ion beam (FIB) based tomography, taking advantage of epoxy infiltration on FIB machining of porous media. It is assumed that the infiltration of epoxy does not significantly alter the geometry of the npg network. Samples of varying structural length-scales were used, with mean ligament diameters in the range of tens to hundreds of nanometers, as achieved through isothermal annealing of npg. Quantitative analyses of the 3D reconstructions were carried out in terms of metric properties (e.g., relative density, ligament diameter distribution and specific surface area), topological properties (e.g., connectivity density), and directional properties (e.g., directional tortuosity). Importantly, representative volumes (RVs) were identified, which reflects the global structural properties of the material. It was found that npg coarsens in a nearly self-similar manner. This allows the identification of structural parameters, which can be used to describe the mechanical behavior of the global npg structure over varying length scales. FEM simulations applied to meshed RVs of the 3D reconstructions strongly suggest that the effective relative density of the load bearing ligament structure is the critical structural parameter in determining the mechanical behavior of npg structural geometry, rather than the solid relative density alone, as is often assumed.

After infiltration with epoxy, the densification during deformation of npg-epoxy composites is strongly suppressed. This leads to a strongly enhanced strength compared to pure npg. However, the dependence of the yield strength on the mean ligament size is much weaker in the composite structure as compared to pure npg. The size effects in pure npg have been commonly attributed to dislo-

cation activities within the gold ligaments, whereas in the composite material the influence of the interface on the motion of the dislocations and the epoxy chains must be considered. The interfacial behavior leads to a strengthening effect in the composites but weakens the size effects. The comparisons of the elastic moduli from the analytical models predictions, the experiments and the FEM simulations demonstrated the influences of the connectivity, the effective relative density of the load bearing ligament structure, the directional tortuosity of the ligaments and the interface on the elastic behavior of the npg-epoxy composites. Interfacial failure was experimentally observed under compression and tension. The tension-compression asymmetry investigation revealed that the npg-epoxy composite is stronger in compression than in tension. These various observations point to the important roles that the hard phase, i.e., the interconnected ligament network, the soft phase, i.e., the continuous epoxy, and the interface between them play on the mechanical behavior of npg-epoxy composites.

Zusammenfassung

Nanoporöses Gold (NPG), ein bikontinuierliches Netzwerk aus nanoskaligen Goldligamenten und Poren, weist durch Variation der inneren Längenskalen ein abstimmbares mechanisches Verhalten auf. Allerdings ist es schwerwiegend eingeschränkt durch seinen Mangel an Verformbarkeit unter Zugspannung. Durch Infiltration der porösen Struktur mit Epoxid erhält man ein Kompositmaterial mit verbesserter Zugverformbarkeit und Fließspannung. Die vorliegende Arbeit strebt eine dreifache Untersuchung des mikromechanischen Verhaltens, der Verformungsmechanismen und des mechanischen Versagens von NPG–Epoxid Kompositen an, durch Fokussierung auf 3D Mikrostrukturcharakterisierung, Finite Elemente Simulation (FEM) und mikromechanische Prüfung.

Um die Kompositmikrostruktur zu verstehen wurden hochaufgelöste 3D Rekonstruktionen mit auf fokussierten Ionenstrahlen (focused ion beam, FIB) basierter Tomographie hergestellt, möglich gemacht durch den positiven Effekt der Infiltration mit Epoxid auf die Bearbeitung poröser Medien mit FIB. Dabei wird angenommen, dass die Epoxidinfiltration die Geometrie des NPG Netzwerks nicht signifikant ändert. Proben mit unterschiedlichen strukturellen Längen wurden verwendet, d.h. mit mittleren Ligamentdurchmessern im Bereich von einigen 10 bis mehrere 100 nm, erreicht durch isothermes Anlassen. Es wurden quantitative Analysen der 3D Rekonstruktionen durchgeführt hinsichtlich der metrischen Eigenschaften (z.B. relative Dichte, Verteilungen der Ligamentdurchmesser und spezifische Oberfläche), topologischen Eigenschaften (z.B. Konnektivitätsdichten) und richtungsabhängigen Eigenschaften (z.B. Richtungstortuosität). Von großer Wichtigkeit war die Identifikation von repräsentativen Volumen (RV), die die globalen Struktureigenschaften des Materials reflektieren. Es wurde herausgefunden, dass NPG nahezu selbstähnlich vergrößert. Dies erlaubt die Identifizierung struktureller Größen, die zur Beschreibung des mechanischen Verhaltens globaler NPG Strukturen über variierende Längenskalen verwendet werden können. FEM Simulationen angewendet auf vermaschte RV der 3D Rekonstruktionen weisen stark darauf hin, dass die effektive relative Dichte der lasttragenden Ligamentstruktur die kritische Größe in der Bestimmung des mechanischen Verhaltens der NPG Strukturgeometrie ist, eher als die relative Dichte der festen Phase wie oft angenommen.

Nach der Infiltration mit Epoxid ist die Verdichtung von NPG–Epoxid Kompos-

iten unter Verformung stark unterdrückt. Dies führt zu einer stark verbesserten Festigkeit im Vergleich zu reinem NPG. Allerdings ist die Abhängigkeit der Fließgrenze von der mittleren Ligamentgröße viel schwächer in der Kompositstruktur verglichen mit reinem NPG. Die Größeneffekte in reinem NPG sind üblicherweise Versetzungsaktivitäten in den Goldligamenten zugeordnet worden, wogegen im Kompositmaterial der Einfluss der Grenzfläche auf die Versetzungsbewegung und die Epoxidketten in Betracht gezogen werden muss. Das Grenzflächenverhalten führt zu einem Verstärkungseffekt in den Kompositen aber schwächt die Größeneffekte ab. Die Vergleiche der Elastizitätsmoduln aus den Vorhersagen der analytischen Modelle, den Experimenten und der FEM Simulationen demonstrierten die Einflüsse der Konnektivität, der effektiven relativen Dichte der lasttragenden Ligamentstruktur, der Richtungstortuosität der Ligamente und der Grenzfläche auf das elastische Verhalten der NPG–Epoxid Komposite. Grenzflächenversagen wurde experimentell beobachtet unter Kompression und Zug. Die Untersuchung der Zug–Druck Asymmetrie zeigte, dass das NPG–Epoxid Komposit stärker unter Druck als unter Zug ist. Diese unterschiedlichen Beobachtungen zeigen die wichtigen Rollen auf, die die harte Phase, also das verknüpfte Ligamentnetzwerk, die weiche Phase, d.h. das kontinuierliche Epoxid, und die Grenzfläche zwischen ihnen für das mechanische Verhalten von NPG–Epoxid Komposite spielen.

Contents

1	Introduction	1
1.1	Motivation and objectives	1
1.2	Structure of the thesis	4
2	Background	7
2.1	Mechanics of open-cell porous materials	7
2.1.1	Gibson–Ashby scaling relations	7
2.1.2	Nanoporous gold	9
	Hardness and yield stress relation	9
	Size dependent yield strength	10
	Elastic modulus	11
	Validity of Gibson–Ashby scaling relations for npg	11
	Tension–compression asymmetry	13
2.2	Mechanics of two-phase composites	13
2.2.1	Analytical models predictions	14
	Isostress and isostrain conditions	15
	Ravichandran model	16
	Tuchinskii model	17
2.2.2	Nanoporous gold–epoxy composites	18
	Compressive behavior	19
	Tensile behavior	19
2.3	3D microstructural analyses	20
3	Methods	23
3.1	Sample preparation	23
3.2	Microstructural characterization	23
3.2.1	FIB–SEM dual beam system	23
3.2.2	FIB–SEM tomography	25
3.3	Micromechanical behavior characterization	29

3.3.1	Nanoindentation	29
3.3.2	Microcompression	32
	Microcolumn fabrication	33
	Microcompression analysis	36
3.3.3	Microbeam bending	38
	Microbeam fabrication	39
	Microbeam bending analysis	40
3.3.4	Digital image correlation	42
	Basic principles of DIC	42
	DIC with <i>in-situ</i> SEM imaging	45
3.4	FEM simulation	45
3.4.1	FEM model meshing	45
3.4.2	Boundary conditions and material parameters	46
4	3D Microstructural Characterization of Npg	49
4.1	Image processing	49
4.1.1	Registration	49
4.1.2	Segmentation	50
4.1.3	3D visualization	51
4.1.4	3D skeletonization	52
4.2	Geometrical microstructural parameters definition	53
4.2.1	Relative density	53
4.2.2	Ligament diameter distribution	53
4.2.3	Specific surface area	55
4.2.4	Topology properties	55
4.2.5	Directional tortuosity	59
4.3	Representative volumes	61
4.3.1	RVs determination	61
4.3.2	Quantitative analyses of RVs	65
4.4	Conclusions	69
5	Mechanical behavior of Npg	71
5.1	Micromechanical characterization	71
5.1.1	Nanoindentation	71

5.1.2	<i>In-situ</i> microcompression	72
5.2	Mechanical behavior of structural geometry	74
5.2.1	Determination of a mechanical RV	74
5.2.2	Mechanical anisotropy	76
5.2.3	Mechanical behavior of a RV	76
5.2.4	Mechanical behavior self-similarity of RVs	77
5.3	Correlation between microstructure and mechanical behavior	79
5.3.1	Role of effective relative density	80
5.3.2	Role of directional tortuosity	83
5.4	Conclusions	84
6	Mechanical behavior of Npg-Epoxy Composites	87
6.1	Micromechanical characterization	87
6.1.1	Nanoindentation	87
	Hardness and elastic modulus	87
	Effect of strain rate	92
6.1.2	Microcompression	92
	Yield stress and elastic modulus	92
	Failure behavior	97
6.1.3	Microbeam bending	100
	<i>In-situ</i> microbeam bending	100
	Digital image correlation	101
	Neutral axis movement analysis	103
	Failure behavior	105
6.2	Mechanical behavior of structural geometry	106
6.3	Discussion	108
6.3.1	Size effect in hardness and yield strength	108
6.3.2	Elastic modulus predictions using analytical models	109
6.3.3	Interfacial failure	111
6.3.4	Tension-compression asymmetry	112
6.4	Conclusions	113
7	Summary and Future Work	115

7.1 Summary	115
7.2 Suggestions for future work	117
Bibliography	119

Nomenclature

α	power law exponent
a	reinforcement size
b	matrix thickness
$a_{u,plane},$ $a_{v,plane}$	plane parameters of least squares planes fit on the subset of the DIC measured displacement
A	indenter projected contact area in nanoindentation testing; cross section area of a microbeam
A_0	initial microcolumn cross section area
A_t	cross section area of the tension side in a microbeam
A_c	cross section area of the compression side in a microbeam
b_0	width of a microbeam at the support
$b(x)$	beam width as a function of x
BET	Brunauer, Emmett and Teller method for determining specific surface area of nanoporous materials
CSM	continuous stiffness measurement
c_1	dimensionless parameter in the Ravichandran model
c_2	dimensionless parameter in the Turchinskii model
C	connectivity
C_V	connectivity density
C_s	fitting coefficient of a modified scaling relation for npg considered the size effect
$C_1 \cdots C_5$	constants describing the area function of the indenter
$C_{sneddon}$	compliance of the substrate material underneath a microcolumn
C3D4	4-node linear tetrahedron elements of the FEM mesh
C3D10	10-node quadratic tetrahedron of the FEM mesh

C3D10M	10–node modified tetrahedron of the FEM mesh
d	unit cell length of the Tuchinskii model
D	ligament diameter
$\langle D \rangle$	mean ligament diameter
D_i	damping coefficient due to the air gaps in the capacitor plate displacement sensing system of a nanoindentation instrument
D_c	contact damping coefficient
D_0	initial diameter of a microcolumn
D_{mid}	initial microcolumn diameter at the mid–height
D_{bottom}	diameter of microcolumn at the bottom
D^*	flat punch indenter diameter
DIC	digital image correlation
DMA	dynamic mechanical analysis
E	elastic modulus of the tested material
E_{GA}	elastic modulus from Gibson–Ashby scaling predictions
E_{np}	elastic modulus of a (nano)porous material
E_s	elastic modulus of the cell wall material
E_r	reduced elastic modulus
E_i	elastic modulus of an indenter
E_{gold}	elastic modulus of gold
E_{epoxy}	elastic modulus of epoxy
E_f	elastic modulus of fiber
E_m	elastic modulus of matrix
$E_{composite}^{isostrain}$	elastic modulus of a fiber reinforcement composite material in isostrain condition
$E_{composite}^{isostress}$	elastic modulus of a fiber reinforcement composite material in isostress condition
$E_{low}^{Ravichandran}$	elastic modulus of lower bound of the Ravichandran model
$E_{up}^{Ravichandran}$	elastic modulus of upper bound of the Ravichandran model
$E_{low}^{Tuchinskii}$	elastic modulus of lower bound of the Tuchinskii model
$E_{up}^{Tuchinskii}$	elastic modulus of upper bound of the Tuchinskii model

f	reference image grayscale intensity functions at a specific location in DIC
f_m	mean grayscale values of the reference subsets
F	load
FIB	focused ion beam
FEM	finite element method
g	deformed image grayscale intensity functions at a specific location in DIC
g_m	mean grayscale values of the deformed subsets
G	genus
H	hardness
HS	Hashin and Shtrikman
H_v	Vickers hardness
H_0	initial height of a microcolumn
h	contact depth of indenter
h_{column}	displacement of a microcolumn
h_{raw}	raw displacement measured by the system, including load–frame displacement, microcolumn and substrate displacement
$h_{surface}$	initial contact position of the indenter and the microcolumn
$h_{substrate}$	substrate displacement
h_{max}	maximum displacement in nanoindentation testing
h_{LF}	load–frame displacement
$h(\omega)$	amplitude of the displacement oscillation in dynamic indentation mode
I	area moment of inertia of the beam in Gibson–Ashby model
IPC	interpenetrating phase composite
k	Hall–Petch type coefficient
K_s	stiffness of the column support springs of the nanoindentation instrument
K_f	load frame stiffness of the nanoindentation instrument
l	length of square beam in Gibson–Ashby model
l_0	actual path length of a curve along certain direction
L	distance of the support to the loading point of a microbeam

L_0	linear distance between the end points of a curve
L_p	arithmetic average shortest path length between two parallel planes of a volume with network structure
L_e	euclidean distance between top plane and bottom plane of a volume with network structure
L_{RV}	cubic length of a RV
LMIS	liquid metal ion source
m	indenter mass
M	bending moment per unit width at any point along a microbeam
M_t	bending moment of a microbeam
M_p	fully plastic moment of the cell edges in Gibson–Ashby model
n	the number of data points in subset Ω
npg	nanoporous gold
o	center of the largest sphere that fits in the ligament at a point p
p	any point in the ligament
P	reference subset center point of DIC
P^*	deformed subset center point of DIC
$P(x_0, y_0)$	image grayscale intensity function of reference subset center point
$P^*(x_0^*, y_0^*)$	image grayscale intensity function of deformed subset center point
P_{max}	peak load in nanoindentation testing
P_0	amplitude of the force oscillation in dynamic indentation mode
P_{column}	load applied on the microcolumn
Q	neighboring point of the reference subset center of DIC
Q^*	neighboring point of the deformed subset center of DIC
$Q(x_i, y_j)$	image grayscale intensity function of point Q
$Q^*(x_i^*, y_j^*)$	image grayscale intensity function of point Q^*
r	radius of the largest sphere that fits in the ligament at a point p
RV	representative volume
ROI	region of interest
S	initial unloading stiffness in nanoindentation
S_1	set 1 in addition theorem

S_2	set 2 in addition theorem
S_{column}	stiffness of microcolumn
$S_{substrate}$	stiffness of substrate
S_A	area fraction of gold phase on a 2D image
S_V	specific surface area
S_V^{-1}	inverse of specific surface area
S_{gold}	surface area of gold
SEM	scanning electron microscopy
m	strain-rate sensitivity
t	cross section width of square beam in Gibson–Ashby cubic model; thickness of microbeam
TLD	through the lens secondary electron detector
TEM	transmission electron microscopy
u	x -directional displacement component of DIC subset center points between the reference and the deformed subset
$u_{plane}(x, y),$ $v_{plane}(x, y)$	displacement field of least squares planes fit on the subset of the DIC measured displacement
U1, U2, U3	displacement in x,y,z direction
v	y -directional displacement component of DIC subset center points between the reference and the deformed subset; displacement in the loading direction of the microbending testing
V_s	volume of cell wall material of a porous material
V_{np}	volume of a (nano)porous material
V_{total}	sample volume, including ligament and epoxy
V_S^*	relative density of the fully interconnected features
V_{gold}	volume fraction of gold in npg–epoxy composites
V_{epoxy}	volume fraction of epoxy in npg–epoxy composites
V_f	volume fraction of the fiber phase in a composite material
V_m	volume fraction of the matrix phase in a composite material
x	distance of any point on the microbeam to the support
(x_0, y_0)	coordinate of P
(x_0^*, y_0^*)	coordinate of P^*

(x_i, y_i)	coordinate of Q
(x_i^*, y_i^*)	coordinate of Q^*
$x \times y$	pixel size
$x \times y \times z$	voxel size
z	thickness of slices in the slicing direction in Auto slice & view
δ	deflection of square beam in Gibson–Ashby model
ρ_{np}	density of a (nano)porous material
ρ_s	density of the cell wall material
ρ_{eff}	effective relative density
ρ_{np}/ρ_s	relative density of the cell wall material
σ_y	uniaxial yield stress
σ_{GA}	yield stress from Gibson–Ashby scaling predictions
$\sigma_{y,gold}$	yield stress of gold
$\sigma_{y,epoxy}$	yield stress of epoxy
σ_s	yield stress of the cell wall material
σ_{np}	yield stress of a (nano)porous material
σ_0	stress amplitude in dynamic indentation mode
σ_{eng}	engineering stress
σ_t	tensile stress of the microbeam
σ_c	compressive stress of the microbeam
$\sigma_{composite},$ $\sigma_{gold}, \sigma_{epoxy}$	stress in the composites, gold and epoxy, respectively
σ_f, σ_m	stress in the fiber and the matrix phases of a composite material, respectively
θ	angle between the interface normals and the loading direction
ε_0	strain amplitude in dynamic indentation testing
ε_{eng}	engineering strain
$\varepsilon_{composites},$ $\varepsilon_{gold}, \varepsilon_{epoxy}$	strain in the composites, gold and epoxy, respectively
ε_{xx}	longitudinal strain
ε_{xy}	shear strain

ε_{yy}	transverse strain
$\alpha_0, \alpha_1, \alpha_2, \alpha_3$	the number of voxel corners, edges, faces, volumes, respectively
β	indenter geometry constant that describes elastic contact stiffness
β_0	the number of components
β_1	the connectivity
β_2	the number of enclosed cavities
ν_i	Poisson's ratio of the indenter
ν	Poisson's ratio of the tested material
ϵ	indenter geometry constant that describe indenter contact depth
ω	frequency of displacement oscillation in dynamic indentation mode
ϕ	phase angle between load and displacement in dynamic indentation mode
χ	euler number
τ	distance metric tortuosity
τ_D	directional tortuosity
$\dot{\gamma}_{gold}$	work hardening rate of gold
$\dot{\epsilon}$	strain rate
Δ	DIC correlation criteria to find the best match of subsets between the reference and the deformed images
Ω	data point set in DIC subsets
3D	three dimensional

1. Introduction

1.1 Motivation and objectives

Nanoporous gold (npg) is an open-cell network structure material with pore and ligament size at the nanoscale. During the past decades, the interest in npg has been significantly increased due to its promising functionality and ease of fabrication. It has potential applications in catalysis, sensing and actuation because of its nanoscale porosity, high surface area to volume ratio and large reversible strain amplitude [1–5].

Dealloying is a commonly used method for producing npg from an alloy of Au and a less noble metal, such as Ag, Cu or Al [6–8]. During the dealloying process, the less noble constituent of the alloy is dissolved in the electrolyte, the remaining gold undergoes a self organization process and a three-dimensional bi-continuous nanoporous network of interconnected ligaments and pores which have dimensions in the order of tens of nanometers is formed [9,10], as shown in Figure 1.1. The mean ligament size of the porous structure can be easily tuned from a few nanometers to the very low micrometer scale by controlling the dealloying conditions, such as the applied potential, the dealloying time, the electrolyte composition, and mainly the post annealing [6,11].

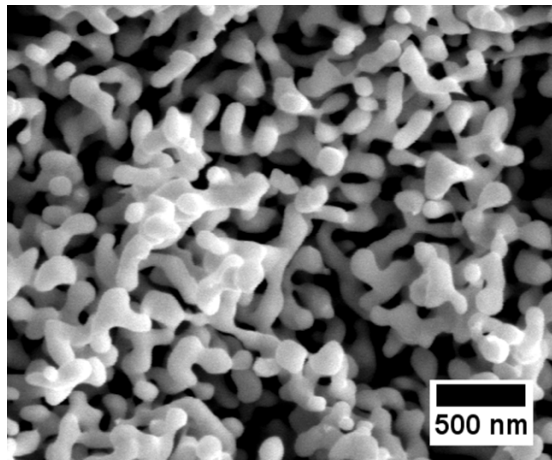


Figure 1.1: SEM micrograph of the nanoporous gold (npg) open-cell network structure. The bright phase is the ligament structure and the dark phase is the pore structure.

The mechanical behavior of npg is a critical aspect of its functionality. Due to the development of micromechanical testing in the last decades, equipments and experimental methods with a resolution down to the nanometer scale became accessible and made it possible to investigate the mechanical properties of npg at the length scale of the ligament size [12–15]. It was found that the mechanical properties of npg are strongly influenced by its microstructural parameters, such as ligament relative density and mean ligament size. For example, npg exhibits a strong ligament size dependent yield strength, i.e., the yield strength increases with decreasing mean ligament size. Similar size effects have been found for metals at sub-micrometer scale, which was attributed to dislocation activities [16–22]. The size effect in npg makes it a particularly useful material to study nanoscale plasticity, and potentially supports its application in micro/nano scale devices. However, it was also found that npg exhibits a strong tension-compression asymmetry in terms of the mechanical behavior, i.e., it shows a strong compressive ductility but macroscopic brittleness under tension [11, 23–29], which strongly limits its applications.

The commonly used Gibson–Ashby scaling relations for open-cell porous materials have been applied for the prediction of mechanical properties of npg, where the ligament volume fraction is the sole input structural parameter [30, 31]. However, it was found that there are big discrepancies in terms of the yield strength and elastic modulus of npg compared to the experimental results [28, 29, 32, 33]. It is unknown if there are any other structural parameters in determining the mechanical behavior of npg, considering the complex 3D microstructure of the interconnected ligament network.

Various experimental and analytical investigations on the understanding of the correlation of microstructure and mechanical behavior of npg have been carried out [27, 34–37]. The direct analyses of the 3D microstructure of npg have been carried out using various tomography methods, such as electron tomography [38, 39] and X-ray nanotomography [40, 41]. However, these methods either only considered the idealized structural geometry for analyses, or have the problem of representativity, i.e., the volumes investigated were not big enough to represent the global structure of the material. A 3D microstructural characterization approach that can provide sufficiently large volumes and a high resolution, and investigations on the correlation between the 3D structural parameters and the mechanical behavior are needed in order to understand the performance of npg.

Inspired by the observations of densification under compression with stable and uniform plastic flow and density reduction under tension with brittle failure of npg, a new material design strategy for improving the tensile ductility of npg by infiltrating epoxy into the pore structure was performed recently [42]. It is assumed that the infiltration of epoxy does not significantly alter the geometry of

the npg network, such that the continuous ligament network are preserved, which act as the reinforcing phase in this interpenetrating phase composite (IPC) with its bicontinuous network structure. This composite is fundamentally different from the conventional composite material, which usually consists of discontinuous reinforcements, e.g., isolated particles, and a continuous matrix. It was found that the npg–epoxy composite exhibits tensile ductility and a much higher strength than pure npg and pure epoxy, whereas the size effect in the yield strength remains [42–44]. To understand the mechanical response of this composite and to potentially optimize its performance, it is important to understand the correlation of the microstructure and the mechanical behavior of individual phases, i.e., the hard phase—the gold which is assumed to be equivalent to npg, and the soft phase—the epoxy, and their interactions at the interface between them. Three basic questions are raised:

- (1) How do the structural length–scales and 3D geometry of the gold phase influence the mechanical behavior?
- (2) How does the existence of the epoxy phase influence the composite mechanical response?
- (3) What are the deformation and failure mechanisms?

The present thesis is focused on the above three questions for npg–epoxy composites with different mean ligament diameters. A three–fold investigation of the composite was carried out, focusing on 3D microstructural characterization, finite element method (FEM) simulation and micromechanical testing, as illustrated in Figure 1.2.

The scientific approaches of the present thesis are as follows:

- Establish a comprehensive three–dimensional microstructural characterization approach for npg–epoxy composites using 3D FIB–SEM tomography, taking the advantages of epoxy infiltration on the FIB machining on porous medias. A list of microstructural parameters of the gold phase of the composites are identified. The representative volumes (RVs) of the 3D reconstructions are determined and quantitatively analyzed.
- With the meshed 3D reconstruction RVs, mechanical behavior of the structural geometry of npg and npg–epoxy composites are studied by FEM simulations to gain sufficient understandings of the influence of salient features of the microstructure on the overall mechanical response.
- Understanding the influence of the epoxy phase on the micromechanical properties, the mechanisms of deformation and failure of npg–epoxy composites using nanoindentation based micromechanical testing. The experimental results provide inputs and validate the model for the FEM simulation.

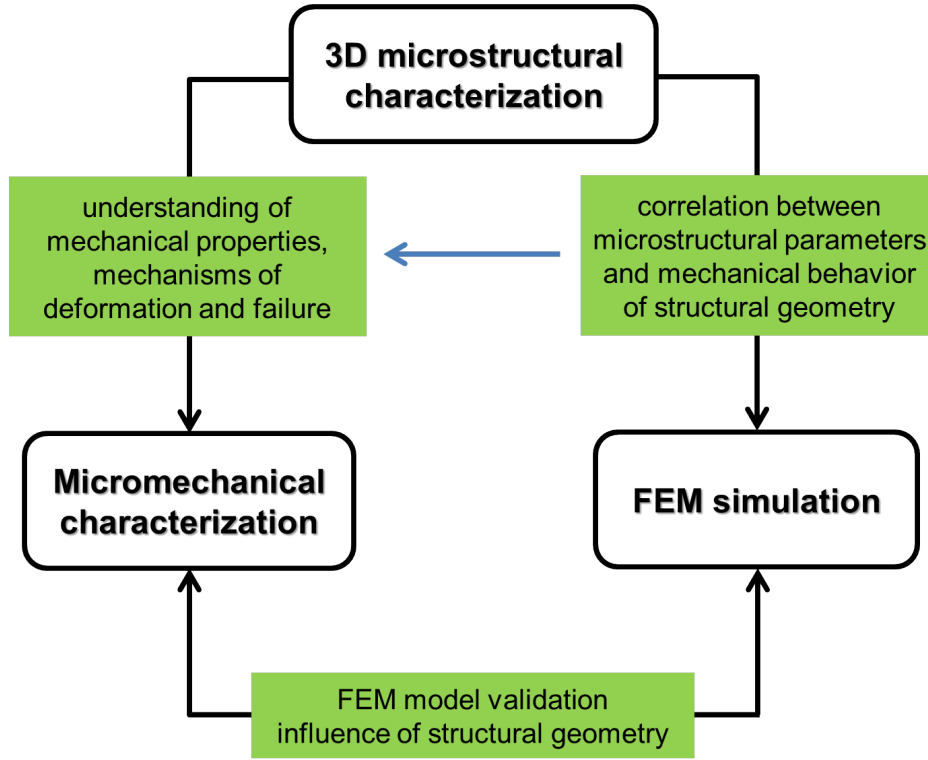


Figure 1.2: Schematic view of the scientific approaches and objectives in this thesis and their interrelations.

They are interpreted and discussed on the basis of the 3D microstructural characterization and FEM simulation results.

1.2 Structure of the thesis

Based on the objectives and the scientific approaches, this thesis is structured as follows:

- In Chapter 2, the background of the thesis is presented, including the mechanics of the open-cell porous materials, the two-phase composites and the 3D microstructural analyses. The mechanical behavior and the microstructure investigations of npg and npg-epoxy composites reported in the literature are reviewed.
- Chapter 3 introduces the experimental approaches of the 3D microstructural and the micromechanical characterization that have been used in this thesis, i.e., 3D FIB-SEM tomography and nanoindentation based micromechanical testing. The inputs for the FEM simulations based on the meshed 3D reconstructions are also presented.
- Chapter 4 is dedicated to the 3D microstructural characterization using FIB-SEM tomography for npg-epoxy composites of varying mean ligament diameters. Image processing and quantitative structural analyses of the 3D

reconstructions are presented. The microstructural representative volume (RVs) are identified and the characteristic structural parameters of the RVs are analyzed.

- In Chapter 5, the identification of the critical structural parameters of npg that determine its mechanical behavior is introduced, focusing on the micromechanical testing of npg and the FEM simulations on the meshed 3D reconstructions of the gold phase of the composites. The correlations between the microstructural parameters and the mechanical behavior of npg structural geometry are discussed.
- In Chapter 6, the effects of the infiltrated epoxy phase are investigated by nanoindentation based micromechanical testing, i.e., nanoindentation, microcompression and microbeam bending for the npg-epoxy composites firstly. A FEM simulation carried out on a 3D meshed reconstruction of the composite was introduced to explore the mechanical behavior of the structural geometry of npg-epoxy composites secondly. Lastly, the size effect, the correlation between the elastic modulus and the microstructural parameters, the failure behavior and the tension-compression asymmetry of the composites are discussed.
- In the last chapter, the findings in the present thesis are summarized and brief suggestions on future work are addressed.

2. Background

2.1 Mechanics of open-cell porous materials

2.1.1 Gibson–Ashby scaling relations

The mechanical behavior of open-cell porous materials is commonly described using the Gibson–Ashby scaling relations in terms of the yield stress and elastic modulus [30,31]. They are derived based on a simplified cubic model representing the cell of a porous material using beam bending theory. As shown in Figure 2.1, the model describes the open-cell structure as a cubic unit cell with connected beams. The beams have a length of l and square cross section with width of t . It is assumed that the beams exhibit large aspect ratios, which allows to model

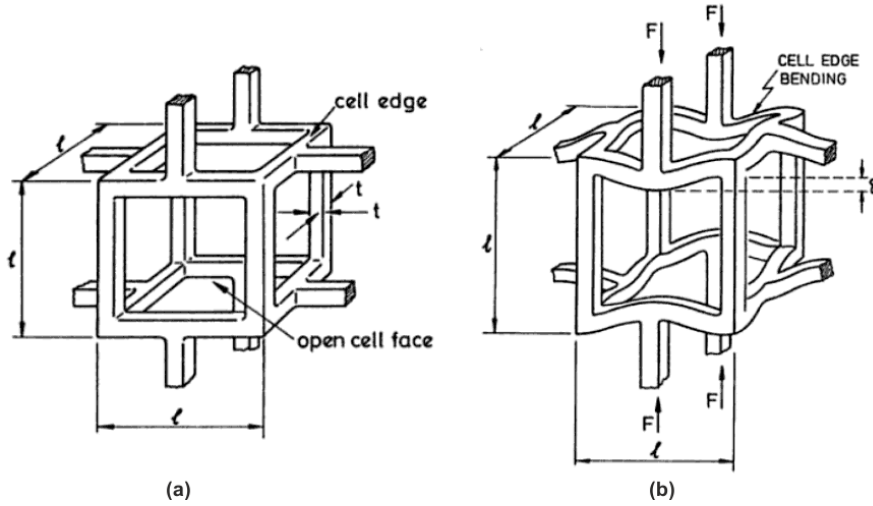


Figure 2.1: (a) A cubic model for an open-cell porous material showing connected beams with length of l and square cross section with width of t ; (b) linear-elastic deflection of the cell loaded at the midpoint of the beams by load F results in a deflection of δ . Three-point bending is the dominant deformation mode. (from [31], reprinted with permission from Cambridge University Press)

the beams as thin flexural components with three-point bending as the dominant deformation mode. The relative density of the cell ρ_{np}/ρ_s and the area moment

of inertia of the beam I are related to the beam dimensions by:

$$\frac{\rho_{np}}{\rho_s} \propto \left(\frac{t}{l}\right)^2 \quad (2.1)$$

$$I \propto t^4 \quad (2.2)$$

where ρ_{np} is the density of a porous material, and ρ_s is the density of the cell wall material. Their ratio actually equals to the volume fraction of the cell wall material, as given by:

$$\frac{\rho_{np}}{\rho_s} = \frac{V_s}{V_{np}} \quad (2.3)$$

where V_{np} is the volume of the porous material, and V_s is the volume of the cell wall material.

The elastic modulus of a porous material E_{np} is calculated from the linear-elastic deflection of a beam loaded at its midpoint by the load F , which is given by:

$$E_{np} = \frac{E_s I}{l^4} \quad (2.4)$$

Combining equations (2.1)–(2.4), the ratio of the elastic modulus of a porous material E_{np} and the cell wall material E_s is given by:

$$\frac{E_{np}}{E_s} = \left(\frac{\rho_{np}}{\rho_s}\right)^2 = \left(\frac{V_s}{V_{np}}\right)^2 \quad (2.5)$$

When the porous material is yielded, plastic collapse occurs when the moment exerted by the force F exceeds the fully plastic moment of the cell edges M_p . This moment is given by:

$$M_p = \frac{1}{4} \sigma_s t^3 \quad (2.6)$$

where σ_s is the yield stress of the cell wall material. The yield stress of the porous material σ_{np} is expressed as:

$$\sigma_{np} \propto \frac{M_p}{l^3} \quad (2.7)$$

Combining with equation (2.1), the ratio of the yield stress of a porous material and the cell wall material is given by:

$$\frac{\sigma_{np}}{\sigma_s} = 0.3 \left(\frac{\rho_{np}}{\rho_s}\right)^{3/2} = 0.3 \left(\frac{V_s}{V_{np}}\right)^{3/2} \quad (2.8)$$

Thus, simple power law relations between the mechanical properties and the cell wall volume fraction of an open-cell porous material are given by equations (2.5) and (2.8). These scaling relations are widely supported by experimental evidences in the case of porous materials with a low relative density $\rho_{np}/\rho_s \leq 0.1$.

2.1.2 Nanoporous gold

The majority of the studies on mechanical behavior of npg relies on nanoindentation testing, from which the hardness H and the elastic modulus E can be obtained directly [24, 27]. Microcompression testing carried out on npg microcolumns enabled extracting uniaxial stress-strain behavior [25, 26]. Additionally, microtensile and microbending experiments were used for the investigations of tensile and fracture behavior of npg [11, 28, 29, 33]. In this section, the experimental results are introduced and compared with the Gibson–Ashby predictions.

Hardness and yield stress relation

The stress-strain field underneath the indenter is quite complex. Extraction of uniaxial stress-strain constitutive relations require complex iterative methods. Some empirical relations between hardness and yield stress of materials have been established [31, 45]. It is generally assumed that the hardness is approximately equal to the yield stress for porous materials with an effective Poisson's ratio of nearly 0. For a fully dense material with an effective Poisson's ratio of 0.5, indentation produces multiaxial stresses which increase the hardness to 3 times the yield stress [31, 45], as shown in Figure 2.2.

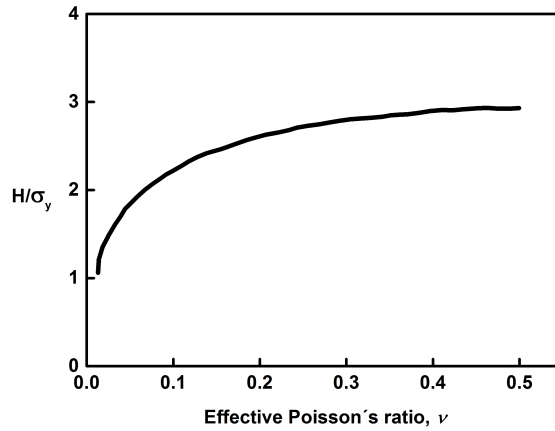


Figure 2.2: Ratio of indentation hardness H to uniaxial yield strength σ_y as a function of effective Poisson's ratio ν . For porous materials with an effective Poisson's ratio of nearly 0, the hardness is approximately equal to the yield stress. (from [31], reprinted with permission from Cambridge University Press)

Residual impressions of Berkovich indentations on bulk npg samples revealed that the region underneath the indenter was compressed and densified, while the region outside the indentation remained undisturbed [24, 27]. It was concluded that the deformation is localized underneath the indenter for npg. Thus, it seems $H \sim \sigma_{np}$ is a reasonable assumption. However, two exceptions were reported. By comparing the Vickers hardness and results from macrocompression tests, it was

found that $H \sim 3\sigma_{np}$ [46]. By uniaxial tensile tests, the elastic Poisson's ratio of npg was reported as 0.22 and it was suggested that $H \sim 2.65\sigma_{np}$ [37].

Size dependent yield strength

Through micromechanical testing, it was found that the yield strength of npg increases with decreasing ligament size, which is so-called "size effect" [25, 27, 46, 47]. It has been described by a power law relation $\sigma_{np} \propto \langle D \rangle^\alpha$, where $\langle D \rangle$ is the mean ligament size and α is the power law exponent. It was reported that α has values of (-1.0 ± 0.1) [43], (-0.91 ± 0.06) [46], -0.5 [48] and -0.551 [37] for npg. This length scale dependent effect is consistent with the sample size effects reported for submicron gold microcolumns and nanowires [16–22]. A good agreement between gold microcolumns and npg was found in [17], which gives a power law relation of $\sigma_y \propto D_0^{-0.61}$, where D_0 is the microcolumn diameter.

Applying the scaling equation (2.8) to npg, from which the yield stress of the gold ligament can be resolved, it was found that the yield stress of the ligaments increased from ~ 880 MPa to 4.6 GPa as the mean ligament size decreased from 40 to 10 nm, which is close to the theoretical shear stress $G/2\pi$ for gold (4.3 GPa) [25]. Similar results from microcompression testing revealed that the yield stress of ligaments with a mean diameter of about 15 nm was approaching 1.5 GPa [26]. These results are consistent with the high yield strength of gold microcolumns from microcompression testing [16–18, 20], which indicates that the strength of npg can be tailored by changing the mean ligament size.

There are several explanations of the mechanisms that lead to the size effects. One of the interpretations relates to the dislocation source limited deformation [17, 49–51], i.e., the applied stress needed to activate the dislocation source increases with decreasing mean ligament size until the theoretical shear strength is reached. This source activation stress depends on the active source size, internal stress fields, or the number of sources [49–51]. The lack of efficient dislocation sources in the small volumes leads to high stresses which are required to initiate yield. Another widely discussed mechanism is dislocation starvation [16, 18, 20], i.e, for submicron crystals, dislocations leave the crystal free surfaces more quickly than they multiply, which leads to the requirement of a high stress to nucleate new dislocations during the deformation. Additionally, a strain gradient plasticity model was proposed to explain the high strength of ligaments [48]. The deformation of a ligament is modeled as the plastic deformation of a cantilever, which is localized near the nodes of the structure where a plastic hinge is formed. A strain gradient in the plastic hinge is accommodated by the geometrically necessary dislocations, which results in enhanced strengthening of the material or strain gradient hardening. Through transmission electron microscope (TEM) it was found that deformation of npg is localized at the nodes with a high density

of microtwins and Shockley partial dislocations [52], which is consistent with the strain gradient plasticity model [48]. The dislocation mediated plasticity within ligaments was also observed by *in-situ* nanoindentation testing in TEM [53].

Elastic modulus

It was reported that the elastic modulus of porous materials is independent of the cell size as long as the solid phase modulus doesn't change [54]. At the nanoscale, the elastic modulus is not expected to increase with the decrease in the sample or microstructure size [55]. For npg, most of the available experimental results revealed that there were little or no ligament size effect in terms of the elastic modulus [56]. One exception was reported in [57]. The length scale dependence of the modulus was attributed to a combination of surface stress [58], a higher bending stiffness of smaller ligaments and a density increase caused by shrinkage and residual Ag [56, 57]. The density increase may also happen during plastic collapse of the structure under compressive stress, which leads to a densification of npg. Through finite element analyses, it was found that the densification of the porous structure occurred in a region immediately below the indenter and it had significant impact on the hardness obtained from indentation. The effect on the indentation modulus was however insignificant [59].

Validity of Gibson–Ashby scaling relations for npg

The Gibson–Ashby scaling equations only consider mechanical behavior as a function of relative density. Their validity for npg is still under investigation. On the one hand, the ligament length scale effect in yield strength as already stated is not taken into account. On the other hand, npg usually has a relative density much higher than the Gibson–Ashby model assumes. The mismatch between experiment and scaling relation predictions were found by various mechanical testings [28, 29, 32, 33, 60]. Figure 2.3 shows the normalized yield stress and the elastic modulus of npg reported in the literature as a function of relative density. The red solid line indicates the prediction from the Gibson–Ashby scaling relations. As can be seen from the figures, the strength predictions are much smaller than observed experimentally. The effect of relative density on the elastic modulus of npg seems to be much stronger than the one suggested by the predictions. Additionally, it was reported that the elastic modulus from molecular dynamics simulations increases during deformation but never approaches the prediction by the Gibson–Ashby scaling law [61]. All these information indicate that Gibson–Ashby scaling relations are not adequate to describe the mechanical behavior of npg. A reconsideration of the application of scaling relations to npg is required.

There are several experimental and analytical investigations on the understanding of the relationship between microstructure and mechanical behavior of npg

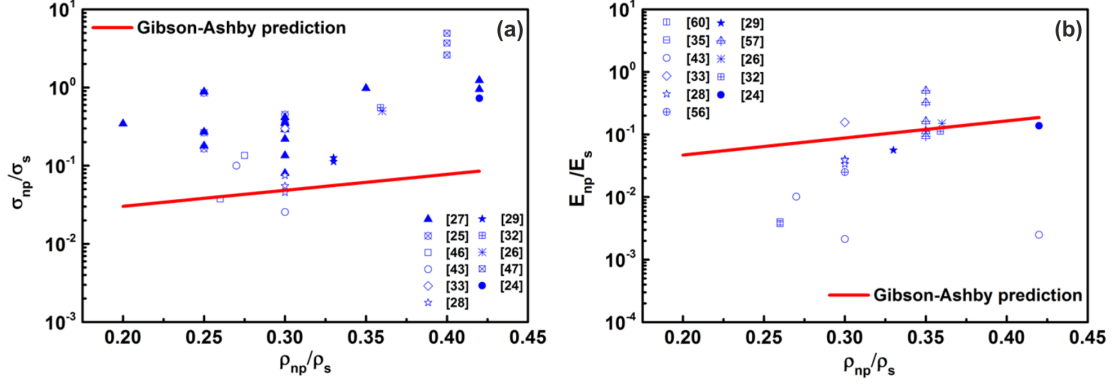


Figure 2.3: Normalized (a) yield stress and (b) elastic modulus of npg reported in the literature plotted as a function of the relative density of npg. The red solid line is the prediction from the Gibson–Ashby scaling relations. For comparison, the yield stress and the elastic modulus of fully dense gold are 200 MPa and 81 GPa, respectively.

[27, 34–37]. The size effect in the yield strength was taken into account in the Gibson–Ashby scaling equation by incorporating a Hall–Petch type relation [27], as given by:

$$\sigma_{np} = C_s(\sigma_{y,gold} + k\langle D \rangle^{-1/2})\left(\frac{\rho_{np}}{\rho_s}\right)^{3/2} \quad (2.9)$$

Where C_s is a fitting coefficient, $\sigma_{y,gold}$ is the bulk gold yield stress, k is the Hall–Petch type coefficient for the theoretical yield strength of gold in the regime of 10 nm to 1 μ m, and $\langle D \rangle$ is the mean ligament size. A similar scaling equation considering the ligament size effect was derived recently, which exhibited better agreement with experimental results [37]. Based on a modified rectangular unit cell model that accounted for the geometrical dimension of the additional mass at the nodes, a scaling relation for the dependence of the relative density and the relative modulus on the geometric parameters such as the mean ligament thickness and length, and the node size was derived [34]. A finite element simulation study based on a diamond beam model which consists of cylindrical beams connected by spherical nodes at randomized positions showed that the structural disorder in the network might have a strong impact on the elastic and plastic response [35, 62]. Recently, a phenomenological model of the npg structure was developed to predict the elastic response based on a statistical analysis of ligaments and nodes in terms of their characteristic lengths from the SEM images of npg. A cubic node connecting six half ligaments with square cross section and a parabolic thickness profile was used as the elementary structural unit. It was found that this model can predict the elastic response of npg correctly and the irregular shape of ligaments plays a critical role in the determination of the mechanical properties [36]. These investigations either considered ligament relative density and ligament size, or treated the npg structure as idealized models. Investigations

on the influence of real 3D microstructure of npg on the mechanical response is still lacking.

Tension–compression asymmetry

The mechanical behavior of npg under tension and compression is different, as observed from experiments and computer simulations. From compression testing, it was found that npg shows strong compressive ductility with densification which allows the pore/ligament compaction and a distribution of the applied load [25,26]. From three point bending testing, a ligament size controlled ductile–brittle transition behavior was observed [11]. Transverse fracture led to failure on the tension side of sample, which indicates that the material is stronger in compression than in tension [23]. As the crack propagated, the tensile regions spreaded through the whole sample until it failed in a macroscopically brittle manner. However, it was found that individual ligaments exhibit strong plastic flow with necking and slip. Similar observations were made from uniaxial microtensile experiments, performed on dogbone shaped npg microsamples [28,29]. The significant asymmetry manifested itself in the Poisson’s ratio. Combined with digital image correlation (DIC), performed on the sample surface, the average Poisson’s ratio of npg under tension was ranging from 0.16 to 0.22 [28,29]. This is much higher than the value of 0.08 estimated by measuring the dimensional change during compressive loading [46], which indicates densification of the npg structure. A molecular dynamics simulation study for a npg model with a mean ligament diameter of 1.8 nm and a relative density of 25% demonstrated that the elastic modulus under tension and compression are the same, but the yield strength and the flow stress are much higher in tension than in compression, which is due to the compressive state of the ligament surface that provides a bias favoring yielding in compression [63].

2.2 Mechanics of two–phase composites

Composite materials are multiphase materials obtained from the combination of two or more individual materials. They have properties that don’t exist in the individual components, such as low density, high strength and high conductivity [64]. For two–phase composites, one of the components is called the reinforcing phase and the other one in which it is embedded is called the matrix. The reinforcing phase could be in the form of fibers, particles, or flakes, whose microstructure are discontinuous, and the matrix phase materials are generally continuous [65]. The interpenetrating phase composites are fundamentally different from other composite materials because of their bicontinuous microstructure. Each phase is topologically interconnected throughout the microstructure [66,67] and contributes its own properties to the composite properties. For example, one phase may provide strength while the other provides transport properties [68]. Many parameters can

affect the overall elastic properties of the composite, such as material constants, volume fraction of the phases, geometrical shape of the phases, presence of discontinuities and damage such as voids, debondings and microcracks [66–68]. In this section, the analytical models used for the predictions of the elastic modulus of composite materials are reviewed firstly. Then the macroscopic mechanical behavior of npg–epoxy composites is presented.

2.2.1 Analytical models predictions

The elastic modulus of a composite material has been estimated by various analytical models, such as the Halpin–Tsai equation [69], the Hashin and Shtrikman (HS) model [70], the Ravichandran model [71] and the Tuchinskii model [72]. For all these models, it is commonly assumed that the bonding between the reinforcement and the matrix is perfect so that there is no debonding at the interface during loading, the possible effects of elastic interactions between the reinforcements were neglected, and the strain over the entire cross section of the composites under uniaxial loading condition were uniform [71].

Isostrain and isostress conditions are commonly used to establish the upper and lower bounds of the elastic modulus of the composite. The Halpin–Tsai equation is one of the widely used empirical expressions to predict the elastic modulus of the composite with randomly oriented short fibers [69]. However, it is difficult to determine the adjustable parameter in the equation, which is a measure of the reinforcement geometry. The commonly used Hashin and Shtrikman model was derived based on the variation principles of linear elasticity without incorporating microstructural geometry information [70, 73, 74]. It has been applied to all composites with arbitrary phase geometry. However, it was found that the accuracy of this model is limited to the case that the difference in moduli of the two phases is small [71, 73]. Additionally, knowledge of the bulk and shear moduli of the components are required for the predictions [71].

The Ravichandran model and the Tuchinskii model were derived based on the idealized unit cells which are approximations of the real microstructure of the composites [71, 72], assuming the composites are homogeneous and isotropic. It is possible to derive the elastic modulus solely from the elastic moduli of the components of the composites. The Ravichandran model was applied to composites with discontinuous reinforcements [71]. For the interpenetrating phase composites, whose interpenetrating phase cannot be extracted as dispersed inclusions [75], the Tuchinskii model was used [72]. The unit cells of these two models were decomposed into parallel and series elements, which are loaded in isostrain and isostress conditions, respectively. As a result, there are two bounds for each model. In this section, the isostress and isostrain conditions, the Ravichandran and the Tuchinskii models are briefly reviewed.

Isostress and isostrain conditions

When the reinforcement is provided by continuous fibers, two idealized conditions, i.e., isostrain and isostress [64, 76] can be envisaged by considering the directions of the applied load relative to the ideal arrangements of the fibers to predict the elastic modulus of the composite, as illustrated in Figure 2.4.

In the isostrain condition, the composite is loaded parallel to the fiber axis. Both the fiber and the matrix are strained at the same amount, as expressed by:

$$\varepsilon_{composite} = \varepsilon_f = \varepsilon_m \quad (2.10)$$

where $\varepsilon_{composite}$, ε_f and ε_m are the strain in the composite, the fiber and the matrix phases, respectively. This load is shared by the fiber and the matrix according to

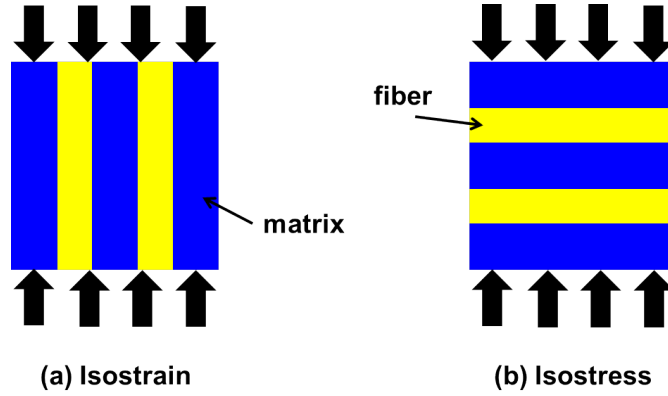


Figure 2.4: Schematic illustration of isostrain and isostress conditions of a fiber reinforcement composite material. Yellow is the fiber phase and blue is the matrix phase. (a) isostrain: the load is parallel to the fibers; (b) isostress: the load is perpendicular to the fibers.

the cross section area occupied by the two phases. The resulting stresses in the two phases are different because the material with higher compliance requires a lower stress to be extended by the same amount as the stiffer material. The stress is distributed in the composite according to rule of mixtures:

$$\sigma_{composite} = V_f \sigma_f + V_m \sigma_m \quad (2.11)$$

where $\sigma_{composite}$, σ_f and σ_m are the stress in the composite, the fiber and the matrix phases, and V_f and V_m are the volume fraction of the fiber and the matrix phases, respectively. Thus, the elastic modulus of the composite is given by the weighted arithmetic mean of the elastic moduli of the two phases:

$$E_{composite}^{isostrain} = V_f E_f + V_m E_m \quad (2.12)$$

where $E_{composite}^{isostrain}$, E_f and E_m are the elastic modulus of the composite, the fiber and the matrix phases, respectively.

In contrast, in isostress condition, the composite is loaded perpendicular to the fiber phase. In this case, the cross section area perpendicular to the stress is the same for the two phases. As a result, the stresses in both the fiber and the matrix are the same, as expressed by:

$$\sigma_{composite} = \sigma_f = \sigma_m \quad (2.13)$$

According to rule of mixtures, the strain in the composite is expressed as:

$$\varepsilon_{composite} = V_f \varepsilon_f + V_m \varepsilon_m \quad (2.14)$$

Therefore, the elastic modulus of the composite is given by the weighted harmonic mean of the elastic moduli of the two phases:

$$E_{composite}^{isostress} = \left(\frac{V_f}{E_f} + \frac{V_m}{E_m} \right)^{-1} \quad (2.15)$$

where $E_{composite}^{isostress}$ is the elastic modulus of the composite.

Ravichandran model

The Ravichandran model considers discontinuous reinforcements embedded in the continuous matrix. The idealized microstructure of this model consists of a periodic arrangement of cubic reinforcements, uniformly distributed in a continuous matrix, as illustrated in Figure 2.5(a).

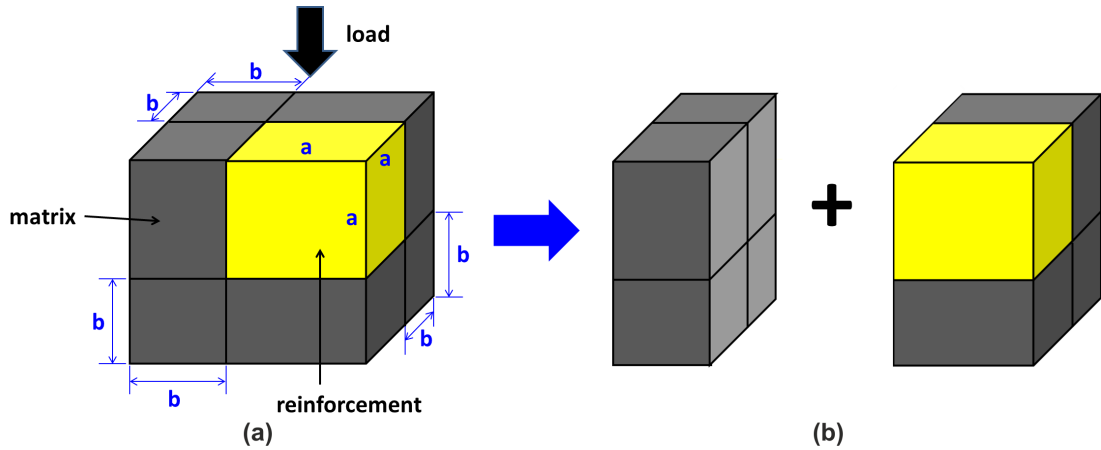


Figure 2.5: (a) Unit cell of the Ravichandran model. The load is applied on the top surface. The reinforcement is shown in yellow with a cubic length of a . The matrix is shown in grey with a thickness of b ; (b) the unit cell is divided into two parts parallel to the loading direction, which is the case of isostrain condition for the unit cell.

In order to predict the elastic modulus of the composite, the unit cell is firstly

divided into two parts, either parallel or perpendicular to the loading direction. Figure 2.5(b) gives an example of dividing the unit cell into two parallel parts. The elastic modulus of each part is calculated according to either isostrain or isostress condition. Then the two parts are reunited and they act as the two phases of the composite. The elastic modulus of the unit cell is calculated according to the loading conditions, either isostrain or isostress. Figure 2.5 is an example of isostrain condition since the load is parallel to the two divided parts. The unit cell reinforcement has cubic length of a and the matrix has thickness of b . The volume fraction of the reinforcement V_f is related to the ratio $c_1=b/a$, as expressed by:

$$c_1 = \frac{b}{a} = \left(\frac{1}{V_f}\right)^{1/3} - 1 \quad (2.16)$$

The lower bound of the elastic modulus of the unit cell is expressed as:

$$E_{low}^{Ravichandran} = \frac{(c_1 E_f E_m + E_m^2)(1 + c_1)^2 - E_m^2 + E_f E_m}{(c_1 E_f + E_m)(1 + c_1)^2} \quad (2.17)$$

The upper bound is given by:

$$E_{up}^{Ravichandran} = \frac{[E_f E_m + E_m^2(1 + c_1)^2 - E_m^2](1 + c_1)}{(E_f - E_m)c_1 + E_m(1 + c_1)^3} \quad (2.18)$$

It was found that the Ravichandran model offers predictions of elastic moduli much closer to experimental results, particularly for composites with phases having large differences in elastic moduli [71].

Tuchinskii model

The Tuchinskii model considers a bicontinuous network structure, whose cubic unit cell is illustrated in Figure 2.6(a). The interpenetrating phase with square cross section is symmetric in the unit cell. A periodic arrangement of the unit cell forms a composite with topologically interconnected reinforcement and matrix phases.

The elastic modulus of the unit cell is calculated using a similar approach as for the Ravichandran model. Firstly, the unit cell is divided into different parts, either parallel or perpendicular to the loading direction. Figure 2.6(b) gives an example of dividing the unit cell into three parallel parts. The elastic modulus of each part is calculated according to the isostrain and isostress conditions with respect to the loading direction. The three parts are then reunited and the elastic modulus of the whole structure is calculated according to either isostrain or isostress condition [72, 74, 75]. Figure 2.6 is an example of isostrain condition since the load is parallel to the three divided parts. As can be seen, the square cross section length of the reinforcement is a and the unit cell cubic length is d . The volume fraction of the

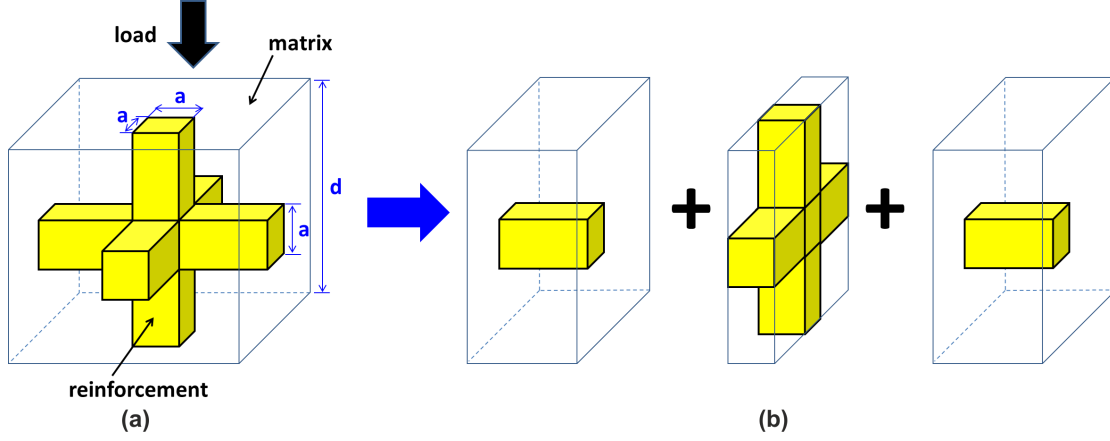


Figure 2.6: (a) Unit cell of the Tuchinskii model with cubic length of d . The yellow reinforcement has a square cross section with a length of a . The matrix is transparent. The load is applied on the top surface; (b) the unit cell is divided into three parts parallel to the loading direction, which is the case of isostrain condition for the unit cell.

reinforcement V_f is related to the ratio $c_2 = a/d$, as expressed by:

$$V_f = (3 - 2c_2)c_2^2 \quad (2.19)$$

The lower bound of the elastic modulus of the unit cell is expressed as:

$$E_{low}^{Tuchinskii} = c_2^2 E_f + (1 - c_2)^2 E_m + 2c_2(1 - c_2) \left(\frac{c_2}{E_f} + \frac{1 - c_2}{E_m} \right)^{-1} \quad (2.20)$$

The upper bound is given by:

$$E_{up}^{Tuchinskii} = \left[\frac{1 - c_2}{(1 - c_2^2)E_m + c_2^2 E_f} + \frac{c_2}{(1 - c_2)^2 E_m + (2 - c_2)c_2 E_f} \right]^{-1} \quad (2.21)$$

2.2.2 Nanoporous gold–epoxy composites

Inspired by the observations of densification under compression with stable and uniform plastic flow and density reduction under tension with brittle failure of npg, a new material design strategy to prevent the density change under load was proposed by vacuum-impregnating npg with epoxy into the pore structure to obtain a npg–epoxy composite material [42–44]. This nanocomposite is an interpenetrating phase composite, where the interconnected ligaments are the reinforcing phase and the continuous epoxy is the matrix. It is light-weight and exhibits a number of unusual mechanical properties under compression and under tension compared to pure npg [42].

Compressive behavior

Similar to pure npg, npg–epoxy composites show a ligament length scale dependent effect in the yield strength. Figure 2.7 shows the macroscopic compression behavior of neat epoxy, npg and npg–epoxy composites with different mean ligament sizes. It was found that the yield strength of the composite increases with decreasing mean ligament size. Moreover, the stress–strain behavior of the npg–epoxy composite follows the trend of the neat epoxy with strongly reduced work hardening compared to pure npg, and the yield strength of the composite is much higher than pure npg and neat epoxy.

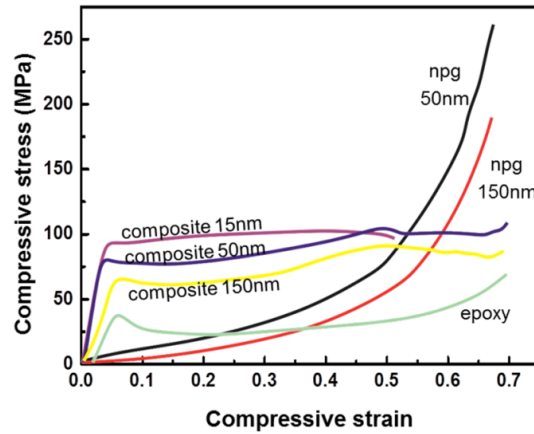


Figure 2.7: Macroscopic compression behavior of neat epoxy, and npg and npg–epoxy composite with different mean ligament sizes. The composite follows the trend of the neat epoxy with strongly reduced work hardening compared to pure npg, and the yield strength of the composite is much higher than pure npg and neat epoxy. (from [42], reprinted with permission from John Wiley & Sons, Inc.)

Tensile behavior

The mechanical behavior of npg–epoxy composites under tension was studied by bending and uniaxial tensile testing [43]. Figure 2.8 shows npg and npg–epoxy composites with the same mean ligament size after three-point bending testing. It was found that the npg–epoxy composites show a considerable tensile ductility while pure npg is macroscopically brittle. This demonstrates that the infiltration of npg with epoxy leads to a ductilization of the composites. By infiltrating different epoxies or polyurethane with different ductilities, the mechanical behavior of the composites can be controlled [43].

Due to the ligament length scale dependence, the strength of the composite can be significantly enhanced by decreasing the mean ligament size, which can be tuned down to 4–5 nm, or by using npg with a hierarchical structure [77]. Except for the ligament size effect, it is unknown if there are other strengthening mechanisms. For example, it is possible that the interface between gold and epoxy

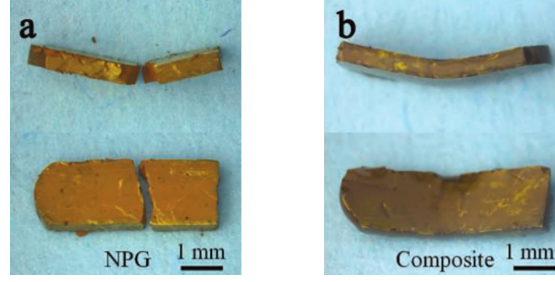


Figure 2.8: (a) npg and (b) npg-epoxy composite with the same mean ligament size after three-point bending testing. Pure npg shows brittle failure and npg-epoxy composite shows considerable tensile ductility. (from [42], reprinted with permission from John Wiley & Sons, Inc.)

phases or a interphase contributes to the strengthening of the material. All the mechanical investigations on the npg-epoxy composites reported were based on macroscale mechanical testing. Understanding the microstructure and its relation to mechanical behavior of npg-epoxy composites at the microscale as well as deformation and failure mechanisms are however lacking.

2.3 3D microstructural analyses

In view of the 3D bicontinuous network structure of npg, it is interesting to know if there are any other structural parameters that control the mechanical behavior except for ligament relative density and mean ligament size. Such parameters may include geometric properties of the 3D structure, such as specific surface area, ligament size distribution, or topological and directional properties, such as connectivity and tortuosity. Obtaining a 3D representation of the microstructure of npg is of critical importance in evaluating and predicting its performance.

Typical imaging methods for structural characterization of materials are optical and electron microscopies, which cannot provide direct quantitative information about the internal nature of materials. In recent years, there has been an increasing interest in the generation of structural information in 3D. Quantitative stereology is a powerful mathematical method that allows to extract 3D geometric properties from 2D sections. However, it usually requires a prior knowledge or simplifying assumptions on the microstructural features [78]. Moreover, a number of important geometric properties of complex microstructure cannot be easily provided by stereology, such as connectivity of microstructural features, 3D shape and size of specific features, the number of features per unit volume, and spatial distribution information [79]. An unbiased, accurate, and complete description of 3D microstructural features is required.

Various techniques have been applied to achieve 3D microstructural characterization for materials. As shown in Figure 2.9, 3D atom probe tomography,

electron tomography, FIB–SEM tomography, X–ray tomography and mechanical serial sectioning can be applied at different length scales with different resolutions. 3D atom probe tomography and electron tomography have high resolution, however, the sample volume that can be analyzed is quite small ($<(1\ \mu\text{m})^3$), which may lead to a representativity problem, i.e., the investigated volume may not be large enough to ensure that the structural analysis is representative of the global structure of the sample [80]. X–ray tomography has resolution typically limited to the micron scale. A spatial resolution down to 100 nm can be achieved with scanning transmission X–ray microscopy using synchrotron or advanced photon sources, which is known as X–ray nanotomography [40, 81]. FIB–SEM tomography has a typical resolution in the range of tens of nanometers to hundreds of nanometers. Site-specific investigation on rather large sample ($>(10\ \mu\text{m})^3$) can be achieved [80, 82]. Moreover, compared to other techniques, FIB–SEM tomography requires little or no sample preparation and is readily applicable to a wide range of materials [79, 82–84].

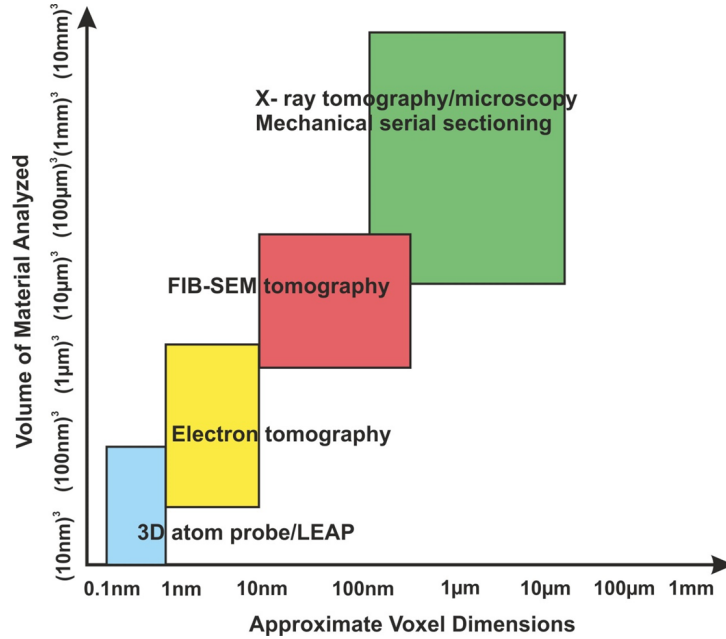


Figure 2.9: 3D microstructural characterization methods applicable to different length scales. (from [79], reprinted with permission from Cambridge University Press)

Electron tomography [38, 39] and X–ray nanotomography [40, 41] have been used for 3D microstructural characterization of npg for the understanding of structural properties and coarsening behavior. The 3D reconstructions were quantitatively analyzed to obtain relative density, ligament and pore size distributions, surface area, ligament and pore channel lengths, local curvatures, surface orientation distribution and genus. For example, a quantitative analysis based on electron tomography for npg with mean ligament size of about 7.5 nm dealloyed from a

thin gold leaf sample (~ 100 nm) showed that ligaments and pores were topologically and morphologically equivalent [39]. A X-ray nanotomography analysis was performed for a ~ 10 μm diameter and ~ 20 μm height npg sample with a characteristic length (determined as the inverse of specific surface area) of about 145 nm. It was shown that the morphology of the npg structure was anisotropic and the topology was similar to bicontinuous structures created by simulated phase separation [40]. Using the same experimental technique and microbeam Laue diffraction experiments, the structural evolution during isothermal coarsening of npg was studied [41] for npg samples with mean ligament sizes larger than 100 nm. The surface normal orientation, interfacial curvature and mean ligament size (determined as the inverse of specific surface area) were measured as a function of the coarsening time from 2 to 320 min. It was reported that the scaled interface shape distributions are not self-similar over time and it was concluded that the coarsening of npg didn't occur in a self-similar manner. Although these two tomography methods enable quantitative analysis of npg microstructure in 3D, there are limitations on the samples in terms of ligament size and sample volume. For example, electron tomography requires thin samples (~ 100 nm) with ligament sizes smaller than 10 nm. In this work, FIB-SEM tomography was used in order to get 3D microstructure information of sufficiently large volumes for npg structures with mean ligament sizes from several tens of nanometers to several hundreds of nanometers, which is introduced in Chapter 3.

3. Methods

3.1 Sample preparation

The npg samples used in this work were prepared by electrochemical dealloying of mm-sized polycrystalline $\text{Ag}_{75}\text{Au}_{25}$ alloys with mean grain sizes of about 50 μm . The as-dealloyed npg samples were annealed in air at 300°C with annealing time of 2 min, 30 min, 240 min and 420 min. As a result, npg samples with mean ligament sizes of about 20 nm (as-dealloyed), 50 nm, 200 nm, 350 nm and 400 nm estimated at first by SEM imaging were achieved. The open-porous structures were then infiltrated with Bisphenol F epoxy resin (BER 20, Buehler, Germany) and amine hardener (BEH 20, Buehler, Germany) in a commercial vacuum impregnation unit (CitoVaca, Struers, Germany). Detailed descriptions of the synthesis procedure of npg and npg-epoxy composites are given in the experimental section of references [42,43]. The composites samples with dimension of 1.0 mm \times 1.0 mm \times 1.7 mm were then embedded in large epoxy blocks to make them easy to handle for subsequent mechanical polishing. After polishing, the samples were cut using a diamond wire saw to reduce the overall size to be mounted on standard SEM sample stubs. The samples were fixed using silver paste to eliminate charging during electron imaging due to the nonconductive epoxy phase. In the following context, the pure npg sample with mean ligament diameter of about 400 nm is named as npg_400nm, and the five composite samples are named as composite_20nm, composite_50nm, composite_200nm, composite_350nm and composite_400nm. Figure 3.1 shows a SEM micrograph of a mechanically polished surface of sample composite_400nm with small scratches. The gold phase is shown bright and the epoxy is invisible.

3.2 Microstructural characterization

3.2.1 FIB-SEM dual beam system

During the last decades, focused ion beam (FIB) has become an essential tool for fundamental material science studies (e.g., microstructural analysis and TEM sample preparation) and technological applications (e.g., circuit editing and prototype nanomachining). It offers capabilities for both high resolution imaging and flexible micromachining at length scales of a few nanometers to hundreds of mi-

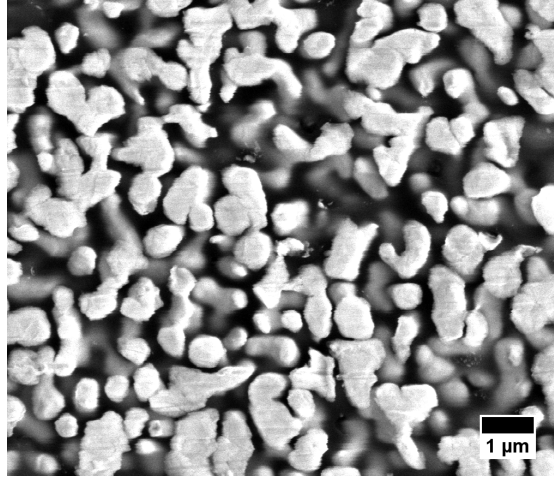


Figure 3.1: A SEM image of a mechanically polished surface of sample composite_400nm with gold shown bright and epoxy transparent.

crometers within a single platform [85].

A typical configuration of a dual beam system incorporates a tilted focused ion beam column and a vertical electron beam column in a single platform, as illustrated in Figure 3.2. In a FIB–SEM dual beam system, the electron beam column provides focused electrons that are accelerated and scanned over the sample surface to create an image. The FIB column operates in a similar approach to the SEM column except that it uses a highly focused beam of ions generated from a liquid metal ion source (LMIS, usually Ga^+). This high energetic ions can be focused to an extremely small spot size, usually on the order of 5–20 nm. This small spot size combined with a rastered movement of the ion beam enables the controlled removal of material at the nanoscale by ion sputtering interactions, leaving the sample surface as either sputtered ions, secondary electrons or neutral atoms. The signals from the sputtered ions or secondary electrons can be collected to form an image [85].

In order to enable ion milling and electron imaging of the sample in the same region, the sample should be firstly located at the eucentric height and the dual beams are adjusted so that they have a coincident point where they cross at the same point of the sample. This combination is especially useful for cross section sample preparation. The electron beam is used to view the cross section while the ion beam mills the sample. The dual beam system is therefore extremely suitable for precisely locating cross sections through highly localized regions of interest [84–86].

The main disadvantage of FIB imaging and machining is the damage created by the ion beam. The ion impact on the sample surface not only leads to material removal by the sputtering process, but also to the formation of a damaged layer which may extend several tens of nanometer into the material. The depth

of this layer from Ga^+ implantation has been estimated to be about 60 nm at 30 kV beam under normal incidence for copper [87]. Depending on the material and temperature, the ion beam damage can lead to sample surface amorphization, point defect creation, dislocation formation, phase formation, grain modification, or other unusual effects [85, 88]. Any surface modification by ion bombardment and implantation may critically alter the mechanical properties of materials. Care needs to be taken for samples with low heat conductivity and micromachined by FIB for micromechanical testing [89–93].

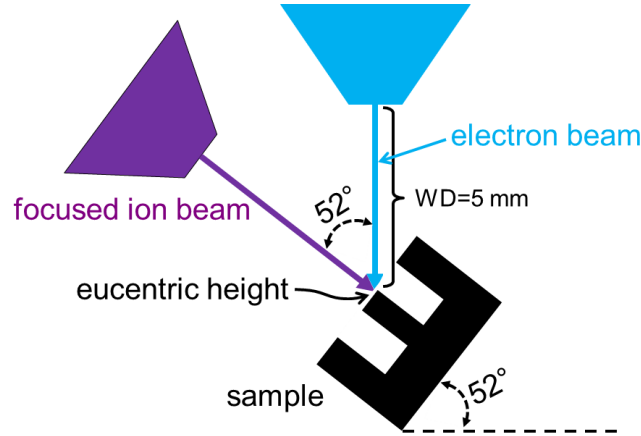


Figure 3.2: A schematic illustration of a FIB–SEM dual beam system with a sample in the standard milling position. The sample is at the eucentric height. The electron beam and the focused ion beam cross at the same point of the sample surface at working distance of 5 mm.

Within this work, a Nova Nanolab 200 dual beam system (FEI) was used for sample imaging, microspecimen (microcolumns, microbeams) preparation and site-specific 3D microstructural characterization. As shown in Figure 3.2, the ion beam is located at an angle of 52° with respect to the electron beam. The two beams coincide at a working distance of 5 mm which is the eucentric height of the system. The sample is tilted to 52° for milling at normal incidence.

3.2.2 FIB–SEM tomography

FIB–SEM tomography is based on a serial sectioning procedure. As shown in Figure 3.3, a planar surface of a region of interest in the sample is firstly created through an ion beam milling process. After sectioning, the freshly exposed surface is imaged using the electron beam. This process of sectioning and imaging is repeated until the desired volume of the material is achieved. In Nova Nanolab 200 dual beam system, the “auto slice and view” script can be used to run this procedure automatically. The following parameters in the script for the region of interest need to be set [94]: (1) milling parameters; (2) number and size of slices to be milled; (3) scan parameters for electron beam imaging. In the milling step, the system creates and saves an electron beam image of the milled surface, then

removes material with the ion beam, repeating these operations until the specified number of slices has been made. Therefore, during the whole procedure, the sample doesn't get moved. The beam shift operation is used to locate the material for the next slicing automatically. After the images acquisition procedure is completed, the stack of images can be transformed into a voxel-based data volume for quantitative analysis using imaging processing and visualization algorithms [79].

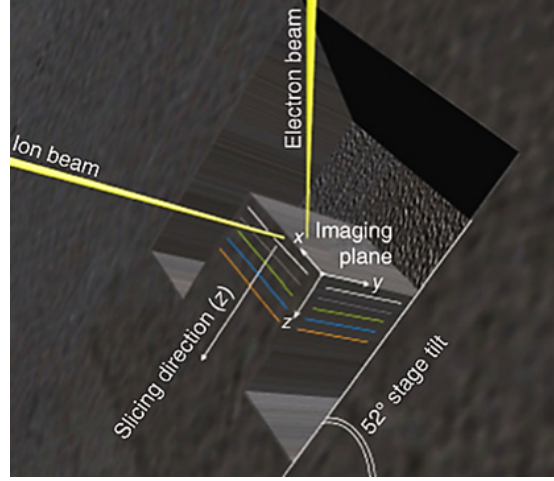


Figure 3.3: Schematic illustration of FIB-SEM tomography within a dual beam system. A planar surface of the region of interest is created by the ion beam milling process. The freshly exposed surface is imaged using the electron beam. This process of sectioning and imaging is repeated until the desired volume of the material is achieved. (from [80], reprinted with permission from John Wiley & Sons, Inc.)

FIB-SEM tomography was used for the 3D reconstruction of npg-epoxy composites in the present work. Due to the epoxy infiltration, very sharp FIB milled cross sections can be obtained for npg-epoxy composites. This is not the case for pure npg, where redeposition of the material during FIB milling will accumulate in the pores. This effect will change the morphology of ligaments artificially, which falsifies the analysis.

During the experiment, because of the oblique imaging angle, dynamic focus and tilt correction of -38° was preset to acquire non-stretched images of the cross sections. Before running the “auto slice and view” script, some rough milling steps for producing the region of interest (ROI) were needed. In order to eliminate shadowing effects which may cause a variation of image intensity and to prevent redeposition of the sputtered material back onto the cross section surface during the image acquisition, a U-shaped trench was fabricated on the sample where the ROI was located. The FIB currents used to cut the trench were 7 nA–20 nA, depending on the ROI size. A protective layer of Pt with thickness of 20 nm–100 nm was deposited on top of the ROI to prevent the material from Ga^+ induced damage and to help reducing curtaining effects. Figure 3.4(a) shows a

U-shaped trench and the direction of the ion beam and the electron beam relative to the ROI. Figure 3.4(b) shows a top view of the trench and the ROI seen in the direction of the ion beam. The amount of material to be milled was covered with a rectangular FIB milling pattern created by the “auto slice and view” script.

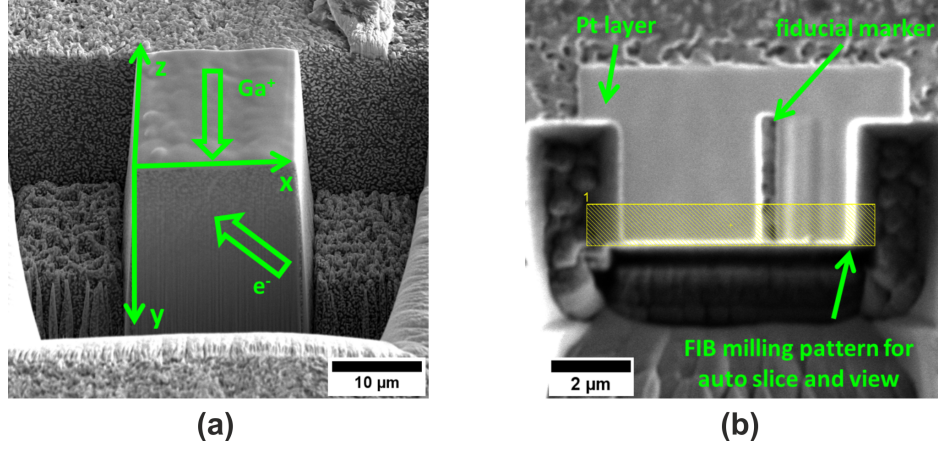


Figure 3.4: (a) A 52° tilted view of the sample shows a U-shaped trench surround the ROI and the direction of the ion beam and the electron beam relative to the ROI; (b) a top view of the sample shows the fiducial marker, the Pt layer and the FIB milling pattern for the “auto slice and view” script.

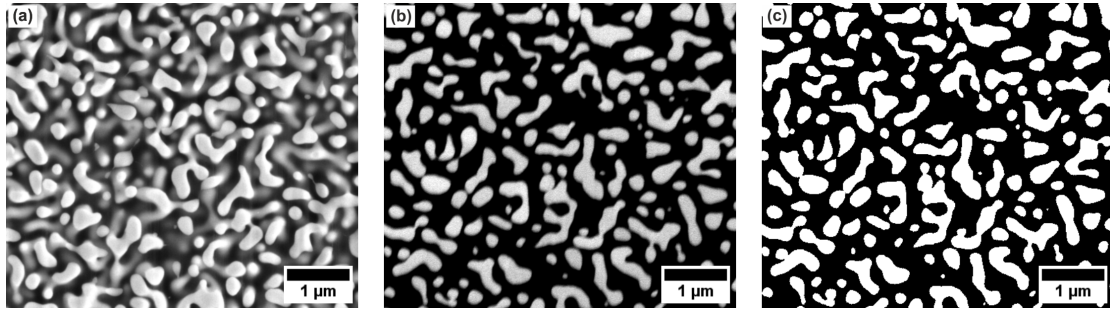


Figure 3.5: SEM image of FIB milled cross sections of sample composite_200nm obtained with electron beam voltages of (a) 10 KV and (b) 2 KV (image (b) and (a) were taken from different regions of the sample); (c) after segmentation process for image (b).

After the ROI was prepared, the voltage, current, magnification, brightness and contrast parameters of the slicing and imaging system were properly adjusted, so that sharp SEM images can be obtained. The Ga^+ beam voltage was set to 30 KV with aperture currents of 0.1–0.3 nA for the “auto slice and view” milling. The through the lens secondary electron detector (TLD) was switched on in the immersion mode for ultra-high resolution imaging and the voltage and currents were set to 2 KV and 0.21–0.54 nA respectively. With these settings, the geometry of the ligaments are distinguished easily without interference of the ligament network

structure underneath the cross sections. Figure 3.5(a) and (b) show SEM micrographs of FIB milled cross section of sample composite_200nm with an electron beam voltage of 10 KV and 2 KV, respectively. Here, it is easy to distinguish the ligaments in these two images. However, when the voltage was 10 KV, ligaments underneath the top surface are also observed. This complicates the segmentation procedure needed in the 3D reconstruction process because it is hard for the software to determine if the ligaments underneath belong to the cross section or not. The area fraction of the ligaments on the cross section could be overestimated since the ligaments underneath might be taken into account. When the voltage was 2 KV, only the ligaments on the surface of the cross section were observed. This is because of the smaller penetration depth and diffusion area of the electron beam at lower voltages. In Figure 3.5(b) the epoxy is shown in black because of the high contrast imaging conditions.

The voxel size determination is very critical for the 3D reconstruction and quantitative analysis. For each reconstruction, normally 400 to 600 consecutive slices through the region of interest were obtained. The number of slices depends on the resolution desired and the volume to be studied. Moreover, the slice thickness in the z direction should have similar dimension to the pixel resolution ($x \times y$) in the imaging plane and the image window size must be adjusted according to the structural size of the sample. The pixel resolution information can be easily obtained from the SEM images with the “.tif” format directly. However, the determination of z value is more challenging. During the FIB milling, there is image drift caused by vibration of the environment and the instrument conditions, which leads to a spatial position error of the slices. In order to estimate this error in the slicing direction, a rectangular fiducial marker was fabricated on the Pt layer surface (Figure 3.4(b)). The difference of the distances between the fiducial marker and the FIB pattern before milling and after milling were measured. This difference was then divided by the number of slices to estimate the mean slice spacing. The voxel size of the 3D reconstructions of the five samples are summarized in Table 3.1.

Table 3.1: Voxel size of the 3D reconstructions of the five npg-epoxy composites

Sample	Voxel size: $x \times y \times z$ (nm) ³
composite_20nm	$3.6 \times 3.6 \times 3.0$
composite_50nm	$5.0 \times 5.0 \times 5.0$
composite_200nm	$12.5 \times 12.5 \times 10.0$
composite_350nm	$25.0 \times 25.0 \times 20.0$
composite_400nm	$17.9 \times 17.9 \times 23.0$

3.3 Micromechanical behavior characterization

3.3.1 Nanoindentation

Nanoindentation testing has been commonly used for the evaluation of mechanical properties of materials in small volumes with a spatial resolution at the nanometer to micrometer range. It is quite versatile for a large variety of materials, such as polymer, ceramics, biological materials and cellular materials.

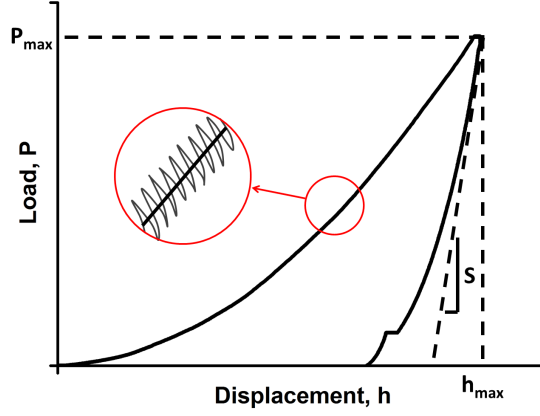


Figure 3.6: A schematic representation of load P versus displacement h for a typical nanoindentation experiment. The continuous stiffness measurement (CSM) mode is implemented during the loading portion. P_{max} and h_{max} are the peak load and displacement respectively. S is the initial unloading stiffness.

A typical nanoindentation experiment consists of the penetration of an indenter with a specific geometry into the material surface and a continuous measurement of the load as a function of the penetration depth as the indenter is driven into and withdrawn from the material [12, 13]. Different types of indenters can be used, such as spherical, Vickers, Berkovich, cube corner, flat punch and Knoop indenter. The Berkovich indenter is used routinely because it is more readily manufactured to a sharper point, ensuring a more precise control over the indentation process [95].

The Oliver–Pharr method is most frequently used to calculate the hardness and the elastic modulus of a material from nanoindentation with one complete loading and unloading cycle [12, 13]. Assuming that the material deforms both elastically and plastically during loading and only elastic deformation is recovered during unloading, the initial slope of the unloading curve is regarded as the elastic contact stiffness S . It is related to the projected contact area of the indenter A by:

$$S = \left(\frac{dP}{dh} \right)_{h=h_{max}} = 2E_r \beta \sqrt{\frac{A}{\pi}} \quad (3.1)$$

where β is a constant, depending on the geometry of the indenter (for Berkovich indenter, $\beta=1.034$; for flat punch indenter, $\beta=1$) and E_r is the reduced elastic modulus that includes deformation of the indenter:

$$\frac{1}{E_r} = \frac{1 - \nu^2}{E} + \frac{1 - \nu_i^2}{E_i} \quad (3.2)$$

where E_i and ν_i are elastic modulus and Poisson's ratio of the indenter, and E and ν are elastic modulus and Poisson's ratio of the investigated material, respectively.

As the geometry of the indenter is known, a big advantage of nanoindentation over conventional indentation testing is that the projected contact area of the residual indent impression can be directly obtained from the calculation of the contact depth of the indenter h using the area function:

$$A = C_1 h^2 + C_2 h + C_3 h^{\frac{1}{2}} + C_4 h^{\frac{1}{4}} + C_5 h^{\frac{1}{8}} + \dots \quad (3.3)$$

The constants $C_1 \dots C_5$ need to be determined by curve fitting of indentation data from indentation into material with known material constants, usually fused silica. Assuming there is sink-in at the rim of the indentation, the contact depth of the indenter h is given by:

$$h = h_{max} - \epsilon \left(\frac{P_{max}}{S} \right) \quad (3.4)$$

where ϵ is a constant that depends on the geometry of the indenter (for Berkovich indenter, $\epsilon=0.75$; for flat punch indenter, $\epsilon=1$). Then the hardness H of the material is determined by:

$$H = \frac{P_{max}}{A} \quad (3.5)$$

where P_{max} is the maximum load.

In addition to the quasi-static indentation measurement, dynamic indentation techniques have been developed [12,13] for the determination of mechanical properties as a function of indenter depth. A “continuous stiffness measurement” (CSM) technique is used for measuring the stiffness continuously during the loading segment. As shown in Figure 3.6, CSM is accomplished by imposing a small dynamic oscillation with high frequency on the force (or displacement) signal during the loading and measuring the amplitude and phase of the corresponding displacement (or force) signal continuously as a function of indentation depth with a frequency specific amplifier [12,13]. The amplitude of the force oscillation is sufficiently small so that the deformation process is not significantly influenced by its addition. The dynamic response of the system is illustrated with a dynamic indentation model shown in Figure 3.7. In this model, m is the mass of the indenter, K_s is the stiffness of the column support springs, D_i is the damping coefficient due to the air gaps in the capacitor plate displacement sensing system, K_f is the load frame

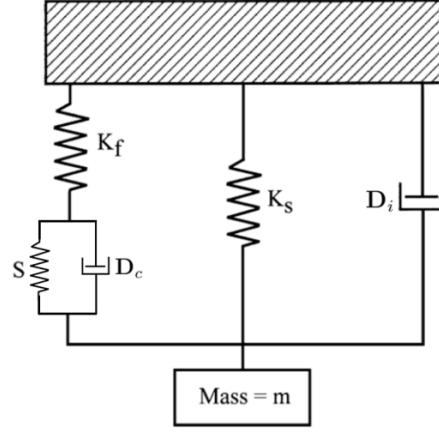


Figure 3.7: A schematic illustration of dynamic indentation model. (from [12], reprinted with permission from Cambridge University Press)

stiffness, and S and D_c are the elastic contact stiffness and the contact damping, respectively. An analysis of the model gives the following equations, from which S can be resolved:

$$\left| \frac{P_0}{h(\omega)} \right| = \sqrt{\{(S^{-1} + K_f^{-1})^{-1} + K_s - m\omega^2\}^2 + \omega^2(D_i + D_c)^2} \quad (3.6)$$

$$\tan \phi = \frac{(D_i + D_c)\omega}{(S^{-1} + K_f^{-1}) + K_s - m\omega^2} \quad (3.7)$$

where P_0 is the amplitude of the force oscillation, ω is the frequency, $h(\omega)$ is the amplitude of the displacement oscillation, and ϕ is the phase angle between load and displacement.

The CSM is especially useful for material with depth dependent properties since the variation of properties with depth can be obtained through a single test. It also offers particular advantage for the determination of the initial contact point of the indenter by inspecting the stiffness changes. Importantly, at high frequencies, the test is less sensitive to thermal drift and a time-dependent plasticity effect can be avoided, which makes it especially useful for measuring mechanical properties of polymeric materials.

In this work, nanoindentation experiments were carried out using a Nanoindenter XP (Agilent Technologies) instrument for pure npg, pure epoxy and npg-epoxy composites. A Berkovich indenter was used and the CSM mode with a 2 nm oscillation and a frequency of 45 HZ at a constant strain rate of 0.005/s was employed for all the samples. The samples were loaded to the maximum indentation depth and hold for 10 s, and then fully unloaded. Additionally, it is well known that epoxy is a viscoelastic material and its deformation behavior is time and rate dependent. In order to investigate the effect of strain rate on the mechanical behavior of npg-epoxy composites, nanoindentation testing with a Berkovich indenter with

strain rates ranging from 0.001/s to 0.1/s were carried out.

For the pure npg samples, additional nanoindentation testing using a flat punch indenter with a diameter of 15 μm were carried out with the indentation depths ranging from 1000 nm to 4000 nm to obtain elastic moduli at different indentation depths. The elastic modulus was calculated using Sneddon's equation [96], which considers the sink-in effect of a cylindrical punch indenting into an elastic half space. An analytical formula to calculate the compliance associated with the deformation of the half space material is given by:

$$C_{\text{sneddon}} = \frac{(1 - \nu^2)\sqrt{\pi}}{2E\sqrt{A}} \quad (3.8)$$

where C_{sneddon} is the compliance of the half space material, E and ν are the Young's modulus and Poisson's ratio of the substrate material, respectively, and A is the contact area of the flat punch. Therefore, the relation between the elastic contact stiffness S and the elastic modulus of npg E_{np} is given by:

$$E_{\text{np}} = \frac{S}{D^*}(1 - \nu^2) \quad (3.9)$$

where D^* is the flat punch diameter. S can be computed from the initial unloading slope of the load-displacement curves. It should be noticed that the flat punch is manufactured from a conical diamond indenter. As the penetration depth increases, the diameter of the contact area is increasing. Therefore, D^* used in the calculation was calibrated according to the geometry of the indenter and the indentation depth.

3.3.2 Microcompression

Microcompression experiments scale conventional uniaxial compression testing to the microscale. In this type of experiment, a microcolumn with circular or square cross section is compressed with a flat punch indenter in a nanoindentation instrument *ex-situ* or *in-situ* the SEM to obtain the stress-strain response. It has been frequently used to determine the mechanical response of various materials in the micrometer and sub-micrometer range since it was firstly reported by Uchic et al. [14, 21, 97]. Figure 3.8 shows a schematic of microcompression testing for a cylindrical microcolumn, with initial height H_0 and diameter D_0 .

Compared to conventional nanoindentation testing which usually produce a complex stress-strain field underneath the indenter, microcompression testing has many advantages. Most importantly, it imposes a nominally uniform, uniaxial stress state within a nominally constant deformation volume, which enables a relatively straight forward stress-strain analysis. In this work, a Nanoindenter XP (Agilent Technologies) instrument equipped with a flat punch indenter with a di-

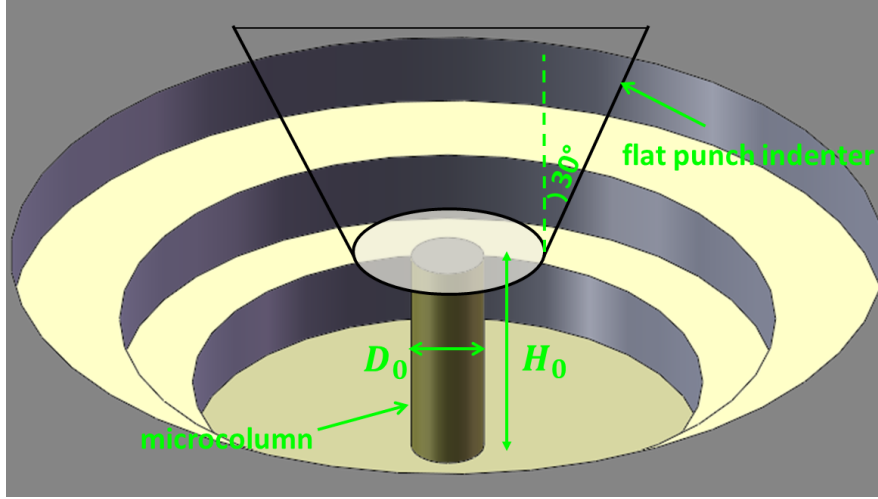


Figure 3.8: A schematic of the microcompression testing. A flat punch indenter is compressed on the top of a cylindrical microcolumn. The height and diameter of the column are H_0 and D_0 , respectively.

ameter of $15\ \mu\text{m}$ and an InSEM nanoindentation system (Nanomechanics, Inc.) equipped with a flat ended conical diamond indenter with a diameter of $20\ \mu\text{m}$ were used for the *ex-situ* and *in-situ* microcompression experiments, respectively. The CSM mode with a $2\ \text{nm}$ oscillation and a frequency of $45\ \text{Hz}$ at a constant strain rate of $0.001/\text{s}$ was employed. A typical experiment consists of two to four loading-unloading segments, then reloading to a prescribed maximum displacement, followed by a $30\ \text{s}$ hold segment prior to final unloading.

Microcolumn fabrication

Microcolumns with sizes in the micrometer and sub-micrometer scale were fabricated using FIB machining. Two types of cylindrical microcolumn fabrication approaches were used: annular milling and lathe milling. Annular milling is easy to carry out [17] but it creates a slightly tapered side wall along the column by fabricating under perpendicular ion impact [98], which leads to increasing cross section areas from the top to the bottom of the column. As a result, uniaxial stress-strain behavior cannot be achieved. Moreover, the column height is difficult to control and the redeposition on the microcolumn surface is very hard to be removed, especially for heterogeneous materials because of different milling rates, which results in a relatively complicated stress-strain analysis. Figure 3.9(a) shows an annular milled microcolumn of a npg-epoxy composite. The expected diameter is $5\ \mu\text{m}$. The taper angle of the microcolumn fabricated using ion beam current of $3\ \text{nA}$ is $\sim 7^\circ$. This leads to a $\sim 40\%$ variation in cross sectional area for the microcolumn with a height/diameter aspect ratio of 3:1. The microcolumn foot is also not well defined.

Taper-free microcolumns with well controlled diameters were fabricated using

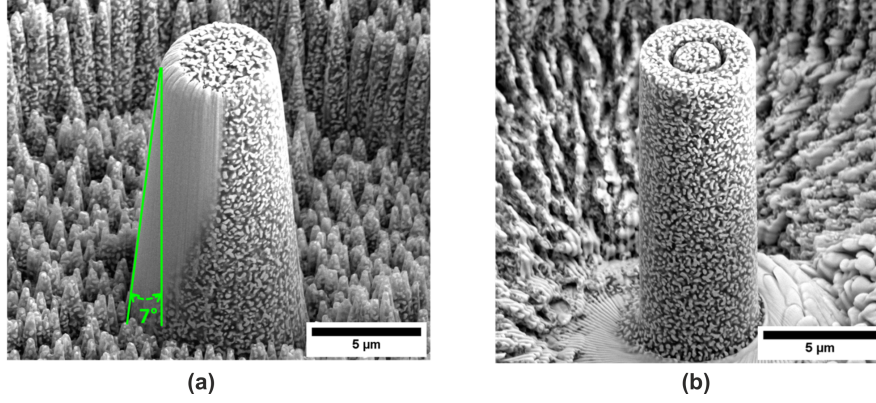


Figure 3.9: Microcolumns of sample composite.200nm fabricated using (a) annular milling; (b) lathe milling. There is a big taper on the annular milled microcolumn. The redeposition on the column surface is strong and cannot be removed completely. The lathe milled microcolumn is taper-free without redeposition on the surface.

lathe milling, which was developed by Uchic and coworkers [14, 97]. A typical microcolumn of sample composite.200nm fabricated with lathe milling is shown in Figure 3.9(b). The fabrication procedure involves several milling steps [99]. In the first step, a ring with two circular patterns is fabricated on the material using a high current ion beam at normal incidence. The inner diameter of the ring is several microns larger than the desired column diameter and the outer diameter is big enough to guarantee that the indenter is only in contact with the column and is not touching the outer ring. The big ring is also needed for enabling oblique imaging of the microcolumn and reducing the probability that sputtered material redeposit back to the freshly milled surface during subsequent milling steps. In order to decrease the milling time, a sequence of rings with decreasing outer diameters but the same inner diameter and depth are usually used. The sum of the milling depth of each ring is equal to the height of the column, as shown in Figure 3.8. After this big ring is milled with a depth close to the targeted final column height, a circular fiducial marker on the top of the column is milled which is small enough to not affect the mechanical behavior of the column but big enough for ion beam imaging. The sample is then tilted to a small angle relative to the ion beam to make sure that the ion beam mills the material from the column's sidewalls, as shown schematically in the green rectangular pattern in Figure 3.10. After the rectangular milling, the stage rotates at a specified angle automatically using a script developed by Shade and Uchic, and then begin a new rectangular milling at the new position. After rotating 360° , a cylindrical column is fabricated. The rectangular pattern actually determines the size of the column. An ion beam image of the fiducial marker is taken before the milling and it is used by a built-in image recognition script for stage reposition for the next milling step after each incremental rotation. For some heterogeneous materials and microcolumns with a

diameter smaller than $2\ \mu\text{m}$, the circular fiducial marker may not be recognizable by the script. In this case, a thin layer of Pt is deposited on top of the column before the second milling step. The fiducial marker fabricated on the Pt layer has a better brightness and contrast to be recognized.

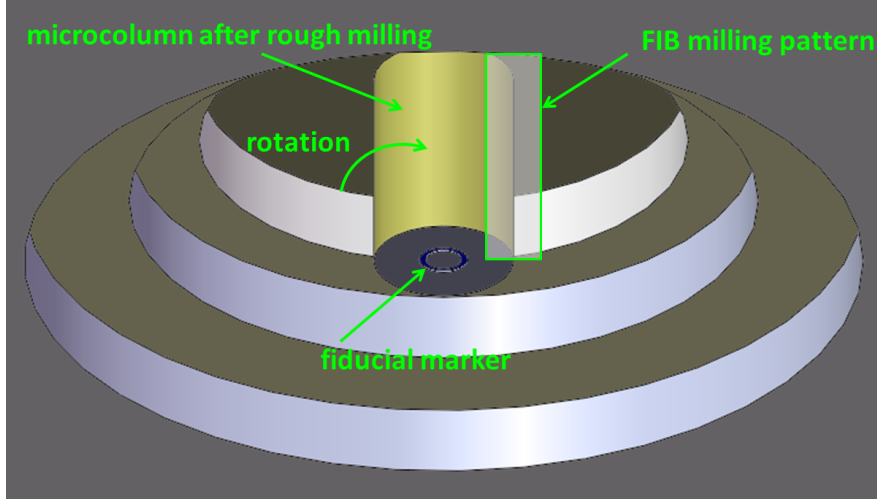


Figure 3.10: A schematic illustration of lathe milling. The rectangular pattern with green frame is used to mill the material on the side wall of the microcolumn. The small circular fiducial marker is used for positioning the stage as it is rotating. A microcolumn of desired geometry is achieved with well controlled diameter and height.

During lathe milling, the ion beam current chosen should be considered carefully, taking into account the milling time for each rotation and Ga^+ damage during the ion beam imaging. Since the column is imaged with the ion beam directly, FIB damage is significant compared to annular milling where the ion beam is parallel to the side wall of the column and no ion beam imaging is needed. Depending on the material and the tested volume, the ion beam damage can vary [99]. In this work, a set of microcolumns with diameters from $2\ \mu\text{m}$ to $12\ \mu\text{m}$ for npg-epoxy composites samples were fabricated using lathe milling, in order to consider possible artifacts from the FIB milling process. As will be shown in Chapter 6, a microcolumn with diameter of $10\ \mu\text{m}$ was found to be sufficiently large to avoid such artifacts.

Except for the cylindrical microcolumns, a microcolumn with a square cross section was used for the *in-situ* microcompression testing for a pure npg sample. The benefit of this microcolumn is that digital image correlation (DIC) measurement can be performed for the planar side surface during deformation. The square microcolumn was fabricated using ion impact perpendicular to the side plane of the column with rectangular FIB patterns. A square microcolumn of pure npg with mean ligament diameter of about $400\ \text{nm}$ is shown in Chapter 5.

Microcompression analysis

Extracting the stress–strain response from a microcompression test requires to consider several critical issues, such as the geometry of the microcolumn in terms of the aspect ratio, the misalignment between the microcolumn and the flat punch, the deformation of the underlying material, the contact friction between the indenter and the microcolumn top surface, and the confined lateral sample displacement [21, 100–102]. A height/diameter aspect ratio between 2:1 and 4:1 has been proved to be a good compromise between barreling and buckling [100]. A misalignment angle greater than 1° leads to a number of test artifacts, such as an underestimated yield point and elastic modulus, changes to the strain–hardening response and buckling [21].

During microcompression testing, the overall compliance includes the combined effect of the compliance of the microcolumn itself, the compliance associated with the column acting like a flat punch indenter elastically pushing into the substrate, and the load frame compliance. Given that compliances are additive here, the displacement of the column h_{column} is given by:

$$h_{column} = h_{raw} - h_{surface} - h_{LF} - h_{substrate} \quad (3.10)$$

where h_{raw} is the raw displacement measured by the system, $h_{surface}$ is the surface position identified at initial contact, h_{LF} is the load frame displacement and $h_{substrate}$ is the substrate displacement. h_{LF} is determined by:

$$h_{LF} = \frac{P_{column}}{K_f} \quad (3.11)$$

where P_{column} is the load applied on the column. The substrate displacement is determined using Sneddon’s equation [96], as shown in equation 3.8. It is expressed as:

$$h_{substrate} = \frac{P_{column}}{S_{substrate}} = \frac{(1 - \nu^2)P_{column}}{ED_{bottom}} \quad (3.12)$$

where $S_{substrate}$ is the substrate stiffness, and D_{bottom} is the diameter of the column at the bottom.

Combining with equations (3.11) and (3.12), it is able to resolve the microcolumn displacement. The resulting expressions for the engineering strain ε_{eng} , the engineering stress σ_{eng} and the elastic modulus E are derived by:

$$\varepsilon_{eng} = \frac{h_{column}}{H_0} \quad (3.13)$$

$$\sigma_{eng} = \frac{P_{column}}{A_0} = \frac{P_{column}}{\frac{\pi}{4}D_0^2} = E \frac{h_{column}}{H_0} \quad (3.14)$$

$$S_{column} = \frac{dP}{dh} = \frac{EA_0}{H_0} \quad (3.15)$$

$$E = \frac{S_{column}H_0}{A_0} = \frac{P_{column}H_0}{h_{column}A_0} \quad (3.16)$$

where A_0 is the initial microcolumn cross section area, and S_{column} is the stiffness of the microcolumn.

With the above equations, it is able to extract the stress–strain curves from microcompression testing. Macroscopically, the yield stress is typically identified using the 0.2% strain offset convention. In this work, an approach based on the loading stiffness of the microcompression testing was used to determine the yield stress from the stress–strain curve, as first described in [103, 104]. The loading stiffness is defined as the slope of every two neighbor points in the loading segment of the load–displacement curve. Due to the misalignment and surface roughness of the microcolumn, the initial contact point is not consistent with the full contact point, which is associated with the maximum loading stiffness. As illustrated in Figure 3.11(a), the yield point is defined as the point where the loading stiffness becomes less than a threshold value of 20% of its maximum value. The yield stress is then taken as the corresponding stress value. Moreover, since the CSM mode was employed in the loading profile, variations of the elastic modulus as the strain increases can be captured, as illustrated in Figure 3.11(b). The elastic modulus of the microcolumn is taken from the plateau area when the indenter was fully contacted with the microcolumn.

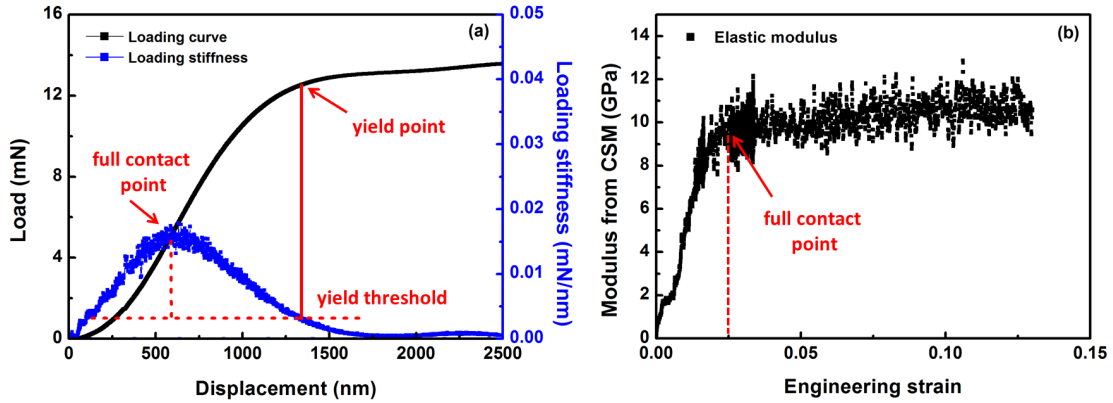


Figure 3.11: (a) The yield point is defined as the point where the loading stiffness becomes less than a threshold value of 20% of its maximum value; (b) the elastic modulus from CSM of the microcompression testing is taken from the plateau area when the indenter was fully contacted with the microcolumn.

3.3.3 Microbeam bending

Microbeam bending experiments have been previously used to assess the fracture properties of internal interfaces of material [104–106], and to study size effects and reversible plasticity [87, 107–109]. The microbeams used in those studies are normally fabricated to rectangular shapes, which produce stress gradients with maximum stresses at the support. A microbeam bending experiment using a triangular in-plane geometry has been developed by Florando and Nix for determining stress–strain relations of thin metal films on silicon substrates [15, 110]. The geometry of this microbeam is shown in Figure 3.12. With this triangular in-plane shape, the microbeam is subjected to a constant tensile strain on the top surface and a compressive strain on the bottom surface simultaneously, which allows to investigate tension–compression asymmetry of materials by evaluating the neutral axis movement.

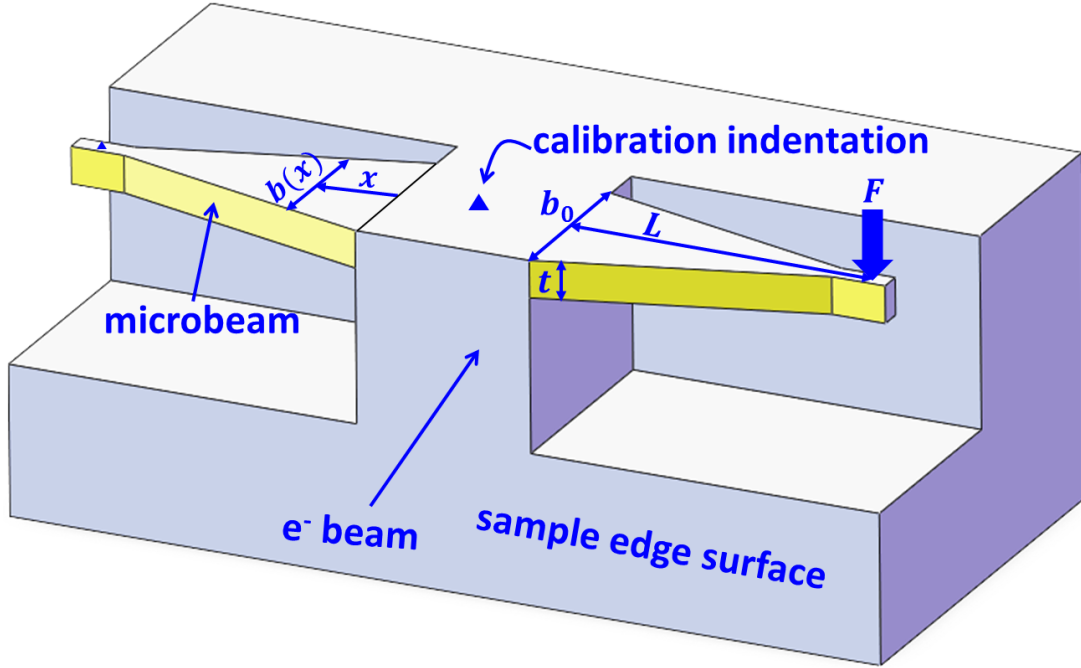


Figure 3.12: A schematic illustration of two microbeams with triangular in-plane shape fabricated at the edge of a sample. On the left beam, x is the distance of any point on the beam to the support, $b(x)$ is the beam width as a function of x . On the right beam, L is the distance of the support to the loading point, b_0 is the width of the beam at the support, t is the beam thickness, and F is the load. An indentation for displacement calibration is shown near the support. The electron beam is perpendicular to the sample edge plane. The projected view of the microbeam side surface is imaged.

Microbeam bending testing in the SEM gives the possibility to observe the deformation of the side surface of the beam and use the digital image correlation

(DIC) technique to measure the full-field displacement and strain directly. In this work, an InSEM nanoindentation system (Nanomechanics, Inc.) equipped with a cube corner indenter was used for the *in-situ* microbeam bending experiment. The indenter was used since it is sufficiently sharp to create visible indents on the beam, avoiding misalignment problems at the contact. It was mounted inside the microscope chamber with the loading axis parallel to the floor. The sample was mounted on a 90° tilted holder and placed in front of the indenter so that it was able to load perpendicular to the top surface of the microbeam, while the electron beam was imaging from the side surface of the microbeam and high quality images were taken throughout the testing simultaneously for DIC measurement. Here, it is worth to mention that with this setup, the SEM images used in the DIC analyses were actually taken from the projected view of the microbeam side surface, as shown in Figure 3.12. This doesn't bring problems to the analysis since the target of the present work is to evaluate the position of the neutral axis qualitatively. Before taking the images, the imaging area of the sample was carefully adjusted so that the microbeam was always in the field of view as it was deflected. The magnification, brightness, contrast of the image and scan speed of the electron beam were carefully adjusted. A typical microbending experiment consists of two loading-unloading segments at a constant strain rate of 0.05/s with hold time of 30 s before unloading, then reloading to a prescribed maximum displacement, followed by a hold-load segment prior to final unloading. The experiment was carried out for the sample composite_400nm.

Microbeam fabrication

The triangular in-plane geometry microbeam fabrication basically includes four steps. In the first step, the sample is tilted to 52°. A near edge region of the sample was chosen in order to minimize the amount of material to be milled by the FIB. With the ion beam normal to the sample surface, a straight edge of the material is milled and a trench of the material parallel to the edge is removed using 30 KV voltage and 7–20 nA ion beam currents. The rest of the material between the edge and the trench should be wider and longer than the final width and length of the desired beam. The milling depth should be sufficiently deep for subsequent cuts to release the microbeam from the material below. In the second step, the stage is rotated by 180° to allow the ion beam mill the material normal to the side surface of the sample and the material below the microbeam is removed, leaving sufficient space for the beam deflection. The same ion beam parameters as for the trench milling are used. After this step, a rectangular microbeam has been fabricated. Thirdly, the stage is rotated again by 180° and the rectangular microbeam is cut into an in-plane triangular shape using a lower ion current (30 KV, 1–3 nA). It should be noted that during milling only the regions adjacent to the microbeam

are allowed to be imaged and the microbeam should not be exposed to the ion beam as much as possible. In order to reduce possible ion beam damage and to remove the redeposition on the surface, a thin layer of the microbeam surface is milled using ultra low ion current (30 KV, 0.1 nA). Importantly, in order to make sure that the SEM images of the side surface of the microbeam are sharp enough for DIC imaging, the last step of the microbeam fabrication is to make a cross section cut for the side surface which facing the electron beam. Moreover, as shown in Figure 3.12, a rectangular pad at the end of the beam is fabricated to provide a location for the nanoindenter to bend the beam. This pad makes the beam slightly stiffer than an ideal triangular geometry. However, it was found that the results will converge to the ideal triangular geometry if the beam is sufficiently long [110].

The microbeam dimension is critical for a reasonable analysis. In order to use the plane strain bending theory, the lateral dimensions of the beam must be large compared to the thickness. In order to obtain high quality SEM images for DIC measurement on the side surface of the beam (surface with yellow color in Figure 3.12), during *in-situ* testing, the beam thickness must not be too small compared to the mean ligament size. The microbeams utilized in the present work had approximated aspect ratios of $L : b_0 : t$ of 7:3:1. The thickness is about 11 times of the mean ligament diameter.

Microbeam bending analysis

As already stated, the triangular beam has the advantage that the beam surface is subjected to a uniform state of plane strain as the beam is deflected, with the top being under tension and the bottom under compression. The bending moment per unit width at any point along the beam (M) is expressed as:

$$M = \frac{M_t}{b(x)} = \frac{F(L-x)}{b_0((L-x)/L)} = \frac{FL}{b_0} = \text{constant}. \quad (3.17)$$

where x is the distance of any point on the beam to the support, $b(x)$ is the beam width as a function of x , M_t is bending moment at any point on the beam. As can be seen from this equation, the beam is subjected to a constant moment per unit width. During bending, it develops a uniform curvature. As a consequence, the material on the top surface of the beam is expected to yield simultaneously at all points along the beam, assuming the material is isotropic. This is different from the standard rectangular geometry beam where yielding first occurs at the support.

A simply way to evaluate tension-compression asymmetry of the beam bending is to analyze the neutral axis movement. The neutral axis is defined as the longitudinal plane in the cross section of the beam which does not experience any

stress and strain and changes in length when the beam is under bending. For a homogeneous, isotropic material, the neutral axis is at the geometric center of the beam. As shown in Figure 3.13, all material above the mid-line of the 2D beam is in a state of tension, while that on the opposite side is in compression. In any transverse cross section of the beam, the equilibrium equation of forces is expressed as:

$$\int_A \sigma dA = \int_{A_t} \sigma_t dA + \int_{A_c} \sigma_c dA = 0 \quad (3.18)$$

where A_t and A_c are the cross section area in the tension side and compression side, respectively; σ_t and σ_c are tension stress and compression stress, respectively. If the material of the microbeam is heterogeneous and anisotropic, the neutral axis might move towards to the tension side or compression side in order to balance the force, depending on which side is stronger. One example is given in Figure 3.13, where the neutral axis moves to the compression side during deflection due to the progression of plastic deformation on the tension side. Knowledge of the location of the neutral axis, which can be characterized using DIC technique, would give a better understanding of the mechanical behavior of the material.

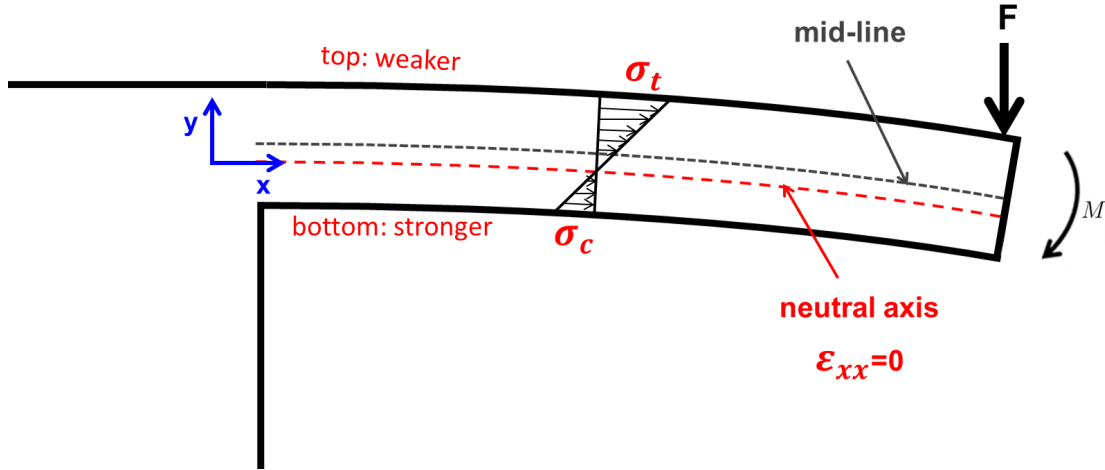


Figure 3.13: The neutral axis of the microbeam moves towards to the stronger side due to the progression of plastic deformation on the weaker side in the example given. This neutral axis movement is dependent on the mechanical behavior of the investigated material.

A critical issue in the beam bending experiment is that when the sharp diamond indenter comes into contact with the beam, the measured displacement consists of the beam deflection and the displacement due to indentation into the beam. Depending on different materials and the total displacement, the contribution of the indentation depth can be significant or can be negligible. In order to evaluate the displacement due to indentation, separate indentation tests were performed on the support of the beam, which experienced the same ion beam milling process as the microbeam surface. The indentation for the displacement calibration is

illustrated in Figure 3.12. It is assumed that for a given load, the indentation displacement is the same no matter if the indenter is indenting a beam or the well-supported material [110].

3.3.4 Digital image correlation

Digital image correlation (DIC) is a practical and effective tool for quantitative in-plane deformation measurements on a planar surface. This technique has been widely used in the field of experimental mechanics because of its non-destructive and non-contact nature [111–115]. It allows to extract the deformation field by comparing images before and after deformation through tracking the movement of a high contrast and randomly distributed speckle pattern on the sample surface. The output is the full-field displacement with sub-pixel accuracy and the full-field strain distribution which is differentiated from the obtained full-field displacement. The images can be obtained from optical microscope for macroscale measurement or SEM for microscale measurement [116–118].

Basic principles of DIC

The DIC technique is based on finding the best match between the local grayscale distribution on the undeformed image (reference image) and the deformed images. In order to provide sufficient local grayscale intensity variations, a suitable randomly distributed tracking speckle pattern with high contrast on the measured surface is very critical. The pattern can be natural surface features or artificially obtained by sputtering and physical deposition techniques, such as air brushing, deposition of nanoparticles, and chemical depositions [119]. It was reported that a good speckle pattern should have a large mean intensity gradient [115]. In the DIC analysis, a region of interest (ROI) in the reference image is firstly defined. It is divided into small regions which are regarded as subsets. The subsets are contiguous square or circular groups of pixel points in the reference image [120]. They should be fine enough for measuring local displacements on the scale of the microstructural features of the material and big enough to include sufficient distinctive features [121]. The deformation is assumed to be homogeneous in each subset and computed by tracking the same points between the reference image and the deformed images, as illustrated in Figure 3.14. In this figure, the reference subset is centered at point P . After deformation, the subset center moves to point P^* . The image grayscale intensity function in these two center points are $P(x_0, y_0)$ and $P^*(x_0^*, y_0^*)$, respectively. The displacement between P and P^* can be described as a x -directional displacement component u and a y -directional displacement component v . Any neighboring point $Q(x_i, y_j)$ in the reference subset is mapped to point $Q^*(x_i^*, y_j^*)$ in the deformed image. The coordinate of point Q^*

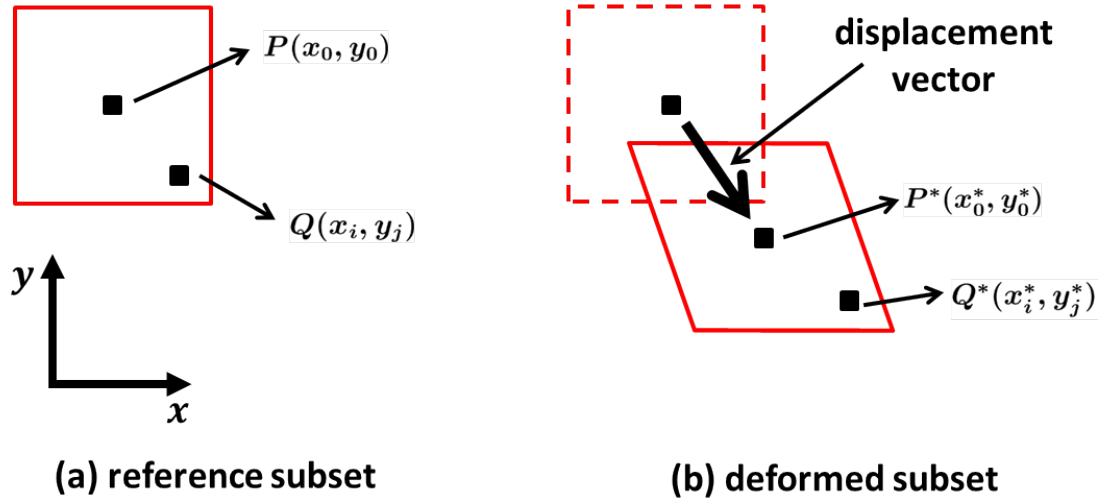


Figure 3.14: Schematic illustration of a reference square subset before and after deformation. The deformation is computed by tracking the same points between the reference image and deformed images. The subset center moves from point $P(x_0, y_0)$ to point $P^*(x_0^*, y_0^*)$. Any neighboring point $Q(x_i, y_j)$ in the reference subset is mapped to point $Q^*(x_i^*, y_j^*)$ in the deformed image. (from [114], reprinted with permission from IOP Publishing)

is expressed as:

$$x_i^* = x_i + u + \frac{\partial u}{\partial x}(x_i - x_0) + \frac{\partial u}{\partial y}(y_i - y_0) \quad (3.19)$$

$$y_i^* = y_i + v + \frac{\partial v}{\partial x}(x_i - x_0) + \frac{\partial v}{\partial y}(y_i - y_0) \quad (3.20)$$

In order to find the best match of the subsets between the reference and deformed images, a correlation criteria must be applied for comparison. There are different definitions of correlation criteria [114, 115, 122, 123]. In this work, the open source 2D DIC software Ncorr [120, 124] based on Matlab has been used. As demonstrated in [125], results generated from Ncorr is in good agreement with a commercial DIC software. The correlation criteria used in Ncorr is given by:

$$\Delta = \frac{\sum_{(i,j) \in \Omega} [f(x_i, y_j) - f_m][g(x_i^*, y_j^*) - g_m]}{\sqrt{\sum_{(i,j) \in \Omega} [f(x_i, y_j) - f_m]^2 \sum_{(i,j) \in \Omega} [g(x_i^*, y_j^*) - g_m]^2}} \quad (3.21)$$

$$f_m = \frac{\sum_{(i,j) \in \Omega} f(x_i, y_j)}{n} \quad (3.22)$$

$$g_m = \frac{\sum_{(i,j) \in \Omega} g(x_i^*, y_j^*)}{n} \quad (3.23)$$

where f and g are the reference and deformed image grayscale intensity functions at a specific location. f_m and g_m are the mean grayscale values of the reference and the deformed subsets. n is the number of data points in subset Ω . A best match of the subsets generates a maximum Δ value. Once the best match is found, the target deformed subset can then be determined and the displacements u and v can be obtained. In the comparison procedure, the grayscale intensity function of a point is very critical. The grayscale value of an integer pixel location is easily obtained from the image. A pixel accuracy of displacements can thus readily be achieved. As for the points located between the pixels, a certain sub-pixel interpolation scheme should be used to get their grayscale intensity [114, 115]. Ncorr uses the Inverse Compositional Gauss–Newton method as the nonlinear optimizer to get sub-pixel resolution results and a Reliability Guided DIC method to obtain displacement values for all the subsets [120]. The strain calculation involves differentiation of the displacement. Any noise in the displacement field will magnify errors in the strain field. Therefore, the displacement gradients must be smoothed before calculating the strain fields. The method used in Ncorr is to apply a least squares planes fit on a subset of displacement data to find the plane parameters given in equation (3.24) and (3.25):

$$u_{plane}(x, y) = a_{u,plane} + \left(\frac{\partial u}{\partial x_{plane}}\right)x + \left(\frac{\partial u}{\partial y_{plane}}\right)y \quad (3.24)$$

$$v_{plane}(x, y) = a_{v,plane} + \left(\frac{\partial v}{\partial x_{plane}}\right)x + \left(\frac{\partial v}{\partial y_{plane}}\right)y \quad (3.25)$$

where $u_{plane}(x, y)$ and $v_{plane}(x, y)$ are the displacement field components. $a_{u,plane}$, $a_{v,plane}$ and the displacement gradients on the plane are solved.

Once the displacement field is obtained, the Green–Lagrangian strain used in Ncorr can be obtained by using the four displacement gradients as expressed below:

$$\varepsilon_{xx} = \frac{1}{2} \left[2 \frac{\partial u}{\partial x} + \left(\frac{\partial u}{\partial x}\right)^2 + \left(\frac{\partial v}{\partial x}\right)^2 \right] \quad (3.26)$$

$$\varepsilon_{xy} = \frac{1}{2} \left[\frac{\partial u}{\partial y} + \frac{\partial v}{\partial x} + \frac{\partial u}{\partial x} \frac{\partial u}{\partial y} + \frac{\partial v}{\partial x} \frac{\partial v}{\partial y} \right] \quad (3.27)$$

$$\varepsilon_{yy} = \frac{1}{2} \left[2 \frac{\partial v}{\partial y} + \left(\frac{\partial u}{\partial y}\right)^2 + \left(\frac{\partial v}{\partial y}\right)^2 \right] \quad (3.28)$$

When dealing with large deformations, the deformed images may change dramatically and a good correlation of DIC subsets between reference and deformed image is not possible. However, any two adjacent deformed images may not change too much to cause correlation problems. An algorithm for using each deformed state as the reference for the subsequent steps and updating the ROI for the deformed

images is implemented in Ncorr. The Eulerian–Almansi displacement is solved, which can be transformed to Green–Lagrangian displacement.

DIC with in-situ SEM imaging

The combination of SEM and DIC enables the investigation of full-field deformation at the micro/nano scale [116–118]. However, it is a challenge to create DIC speckle patterns to obtain accurate deformation results for specimens at microscale. The patterns could be identified from the microstructure surface features on the imaged sample in some cases [117]. In other cases, where little contrast of features on the measured surface is present, a speckle pattern can be made using either electron beam or focused ion beam assisted deposition [104]. In this work, the inherent high contrast pattern generated by the npg ligaments structure could be used as a traceable speckle pattern for DIC analysis without surface modification. This is a significant advantage for npg.

In addition to the speckle pattern, another critical challenge is the SEM imaging artifacts such as electron beam rastering, image drift, and image distortions [116]. Image drift is naturally present in SEM imaging, and beam rastering inconsistencies may lead to image distortions between subsequent image scans. Moreover, SEM images can suffer from substantially more noise than optical images. These artifacts can significantly impact the quality of the results and must be accounted for in order to perform accurate SEM–DIC experiments. In this work, the displacement measurement uncertainties of DIC due to the SEM imaging artifacts were examined by imaging the sample surface using SEM conditions that were identical to those used for the *in-situ* micromechanical testing. For example, for the microbeam bending testing, a series of 260 images of the side surface of the microbeam were obtained over the span of approximately 10 minutes, which is comparable to the time of one microbending testing.

3.4 FEM simulation

3.4.1 FEM model meshing

The 3D reconstructions were meshed for finite element simulations using the Amira software. Basically, triangular surface meshes were firstly created on the surface of the reconstruction. The mesh size was controlled by changing the number of triangular faces on the surface using the “surface simplification” editor in Amira. A small number of faces leads to coarse meshes, which may not represent the ligament geometry adequately. A fine mesh preserves the geometry of the ligaments, however, it requires high computation capability. Then secondly, the mesh was optimized using the “surface editor” option to ensure that there were no intersecting triangles. Additionally, other options for mesh quality optimization were

used as well, such as the aspect ratio of triangles (ratio of radii of the circumcircle and the incircle for each triangle), the dihedral angle (angle between adjacent triangles at their common edge) and the aspect ratio of tetrahedrons (ratio of radii of the circumsphere and the inscribed sphere). Finally, the volume enclosed by the surface mesh was filled with tetrahedrons using the option of “TetraGen”.

It should be noted that 3D meshes obtained from Amira consist of 4-node linear tetrahedron elements (C3D4). The C3D4 element is too stiff and extremely fine meshes are required to obtain accurate results. For tetrahedral element meshes, it is recommended to use the second-order or the modified tetrahedral elements, i.e., C3D10 (10-node quadratic tetrahedron) or C3D10M (10-node modified tetrahedron) [126]. In this study, C3D4 meshes were converted into C3D10 meshes in Abaqus v.6.14 (Dassault Systems Simulia Corp).

3.4.2 Boundary conditions and material parameters

Finite element simulations on the 3D reconstructions were carried out in Abaqus v.6.14. Symmetry boundary conditions were applied to the nodes on the planes $x=0$, $y=0$ and $z=0$, as illustrated in Figure 3.15(a). The load was applied as a homogeneous displacement of all nodes on the top side of the model. All nodes on the side faces were free to move to capture the boundary conditions of a uniaxial compression experiment.

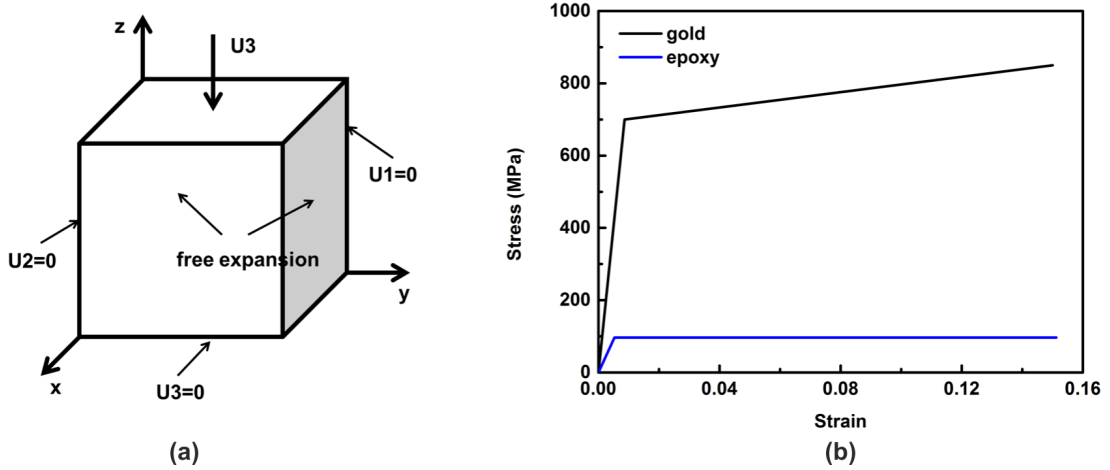


Figure 3.15: (a) Symmetry boundary conditions were applied to the nodes on the planes $x=0$, $y=0$ and $z=0$. U_1 , U_2 , U_3 are displacements in x , y , z direction, respectively; (b) black line: constitutive law of gold with yield stress $\sigma_{y,gold}=700$ MPa, elastic modulus $E_{gold}=81$ GPa and work hardening rate $\dot{\gamma}_{gold}=1000$ MPa; blue line: constitutive law of epoxy with yield stress $\sigma_{y,epoxy}=97$ MPa, elastic modulus $E_{epoxy}=4.7$ GPa and without work hardening.

The constitutive laws for the gold ligaments and the epoxy for the simulations are not clear. Due to the known size effect of gold [17, 25, 26], the determination of

an accurate constitutive law is itself a great challenge. Moreover, the mechanical behavior of epoxy is rate and time dependent. Since the objective of the FEM simulations in the present work is to investigate the influence of the microstructural parameters on the mechanical behavior of the 3D structural geometry, not much effort was made to develop an accurate material model. A simple isotropic elastic–linear plastic stress–strain relation was adopted. Figure 3.15(b) shows the material properties used in the study. The yield stress of gold $\sigma_{y,gold}$ is 700 MPa. The elastic modulus of gold E_{gold} is 81 GPa and work hardening rate $\dot{\gamma}_{gold}$ is 1000 MPa. This extremely high work hardening rate is suggested in [35], which gave a reasonable fit to the experimental results. The yield stress and elastic modulus of epoxy were taken from nanoindentation testing of a pure epoxy, which was also used for the infiltration process of npg–epoxy composites. It is assumed that there is no work hardening and the hardness/yield stress ratio is 3 for the epoxy sample. Additionally, the Poisson’s ratio of gold and epoxy are 0.42 and 0.35, respectively.

4. 3D Microstructural Characterization of Npg

In this chapter, the systematic quantitative structural analyses carried out for the 3D reconstructions of sample composite_20nm, composite_50nm, composite_200nm, composite_350nm and composite_400nm are presented. Characteristic microstructural parameters such as relative density, diameter distribution, specific surface area, connectivity density and directional tortuosity are quantified for the gold phase of the reconstructions. With such quantitative information, representative volumes (RVs) of the npg structure are identified, assuming that the infiltration of epoxy does not significantly alter the geometry of the npg network. The results from the quantitative analyses of the RVs are then presented and discussed.

4.1 Image processing

The open source image processing software Fiji [127] and the commercial 3D reconstruction software Amira 4.1 package (Mercury Computer Systems, Inc.) were used for the image processing, including registration, segmentation, 3D visualization and 3D skeletonization. Before implementing these processes, it is necessary to remove the image noises using some filtering schemes or adjust the brightness and contrast of the images firstly. For the cross section images of npg-epoxy composites, it was demonstrated that little efforts were needed for the original images as long as the slicing and imaging conditions stated previously were properly adjusted for this bicontinuous structure.

4.1.1 Registration

After acquiring the stack of images, the first step is to align the sequential slices relative to each other spatially to eliminate the offset of the images, which is called registration. During the image acquisition, any small changes in the SEM viewing area due to random beam shift and/or sample drift can translate to significant in-plane image displacements between successive image slices. In this work, a sub-pixel registration algorithm was used, which is based on the gray intensity of the stack of images using the plugin of “stackreg registration” in

the Fiji software [127, 128]. Because of the highly distinguishable gold and epoxy structures in the 2D slices, the image alignment is quite feasible using this plugin. Figure 4.1(a) illustrates a stack of images with a nominal spacing of about 23 nm after registration.

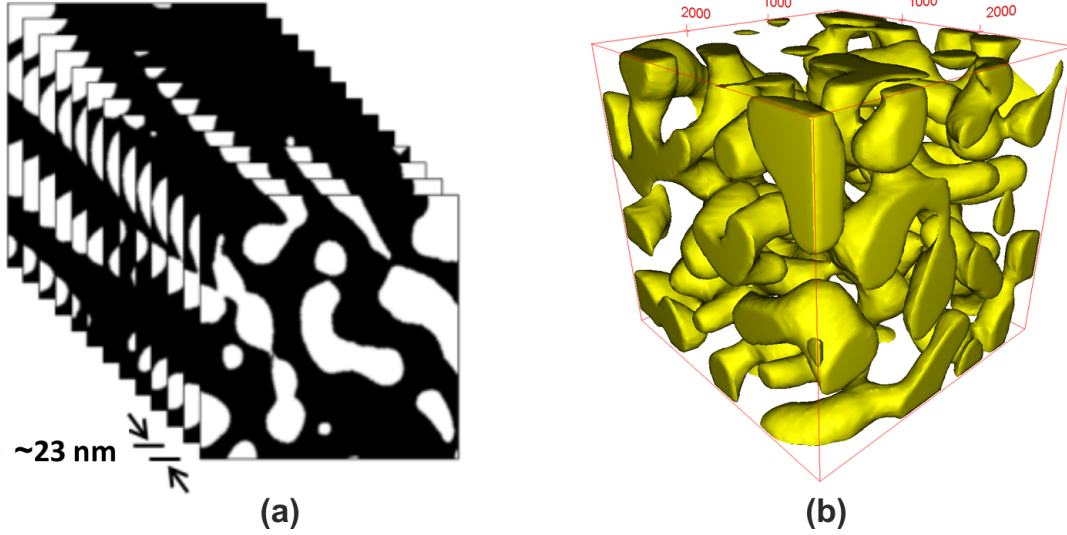


Figure 4.1: (a) 2D cross section images with a nominal spacing of about 23 nm. The bright field is the gold phase and the dark field is the epoxy phase; (b) 3D visualization of the reconstructed npg structure with a mean ligament diameter of 421 nm. The cubic volume is $(3 \mu\text{m})^3$.

4.1.2 Segmentation

After registration, segmentation was carried out for the voxel based dataset, which is to partition regions with respect to the different phases on the images. It enables accurate determination of whether each pixel is occupied by the gold or the epoxy phase. The easiest segmentation technique is the use of a threshold value, i.e., all voxels having a grayscale value within a certain range are partitioned into the same segment. Segmentation with a uniform threshold value demands for an excellent image quality without image shadowing artefacts [129]. The threshold segmentation method is particularly useful for npg–epoxy composites because of its highly distinguishable ligament and epoxy structures on the 2D slices.

In this work, the threshold option of Fiji software was used for the segmentation. The threshold value for the 3D reconstructions of the five samples were determined by a careful comparison of the ligament geometry in the original slices and the slices after segmentation with a specific threshold value. After segmentation, the images were binarized with two gray values left: 255 for the gold phase in white and 0 for the epoxy phase in black. Figure 3.5(c) shows the image after application of the segmentation process to image 3.5(b). There is no obvious difference between the two images in terms of the ligament geometry.

4.1.3 3D visualization

The 3D visualization was performed with the 3D viewer options of either the Fiji or the Amira software. Figure 4.1(b) shows the 3D rendering of a reconstruction of the gold phase of a npg-epoxy composite. The 2D slices that consist of the reconstruction are shown in Figure 4.1(a). Figure 4.2 shows orthogonal cross section images through a reconstruction. The XY plane is the original slice obtained from the experiment. The YZ and XZ planes are the slices created from the reconstruction. Assuming the structure is isotropic, obvious microstructural differences among the three plane views cannot be seen, which indicates that a good quality 3D reconstruction was obtained.

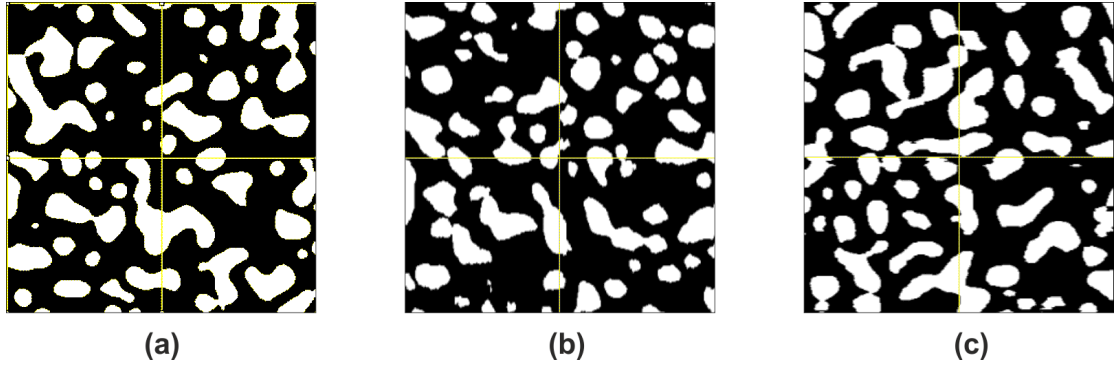


Figure 4.2: Orthogonal cross sections through a reconstruction. The (a) XY plane is the original slice obtained from the SEM imaging. The (b) YZ and (c) XZ planes are the slices created from the reconstruction. Obvious microstructural differences among the three plane views cannot be seen.

From the 3D reconstructions, both surface and volume meshes of the gold phase can be obtained for various investigations. On the one hand, the surface meshes were used for surface properties determination, such as specific surface area and surface normal distribution. On the other hand, the volume meshes were used as input for finite element simulations.

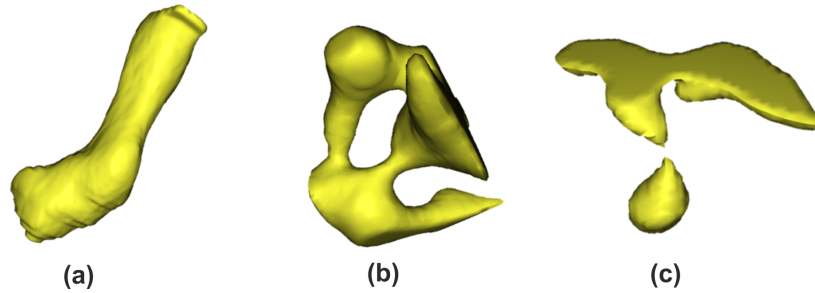


Figure 4.3: Ligaments extracted from the 3D reconstructions: (a) a ligament with a large aspect ratio (length/diameter) of about 8; (b) a interconnected ring structure with varying diameters; (c) disconnected ligaments.

Various ligament structural features were observed in the 3D reconstructions. As shown in the 3D visualization, some of the ligaments are interconnected via thick nodes. Mostly, it is very hard to distinguish the nodes from the ligaments. Some of the ligaments at the edge of the given volume are not fully interconnected because they are cropped from a bigger volume. Most of the ligaments have an irregular shape with varying diameter. Deformation will be localized within the ligaments with smaller diameters. Figure 4.3 shows the 3D view of three kinds of ligaments from the reconstructions: (a) a ligament with a large aspect ratio (length/diameter) of about 8, (b) a interconnected ring structure with varying diameters and (c) disconnected ligaments.

4.1.4 3D skeletonization

As observed from the 3D visualization of the reconstructions, it is not easy to distinguish the nodes from the ligaments since they have irregular shapes. The 3D skeletonization gives a more direct and clear representation for the 3D reconstruction by abstracting the nodes and ligaments into a skeleton.

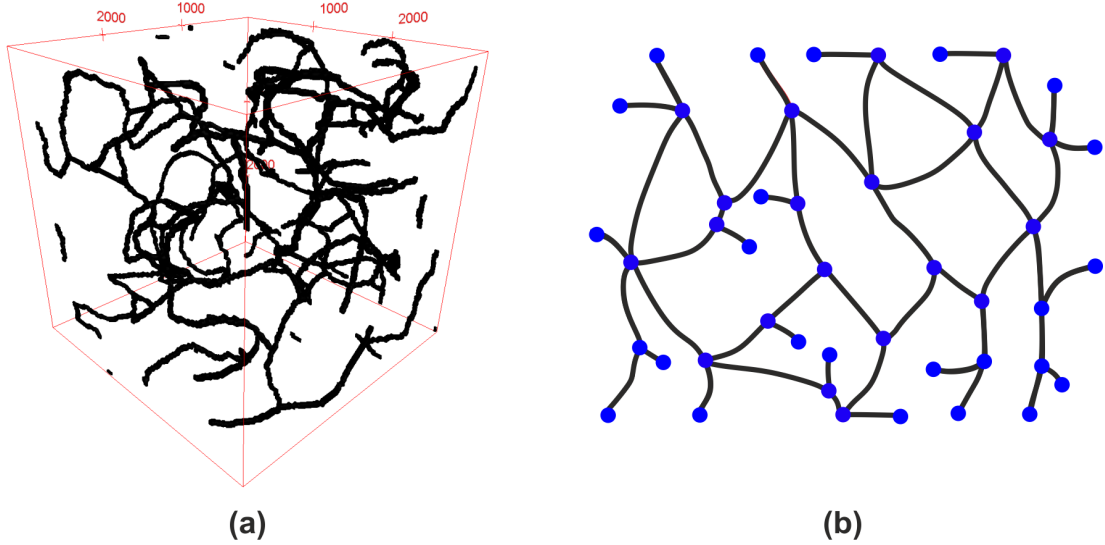


Figure 4.4: (a) 3D skeletonization of a npg structure obtained from the Fiji software. The ligament skeletons are shown as black branches. The corresponding 3D reconstruction is shown in Figure 4.1(b); (b) a 2D schematic illustration of the ligament skeletons. The black branches are connected by the blue nodes.

The open source software Fiji with the “Skeletonize3D” [130] and the “AnalyzeSkeleton” [131, 132] plugins were used for the visualization and analysis of the 3D skeletons of npg structures. Firstly, a thinning algorithm [133] was used to find the centerlines of the features of the structure for the binary stack of images. Basically, the surfaces of the features are eroded iteratively and symmetrically until only the medial position remains, such that the connection of the object is

preserved. Figure 4.4(a) gives the 3D skeletonization of the npg structure shown in Figure 4.1(b). A 2D schematic illustration of the skeletons is shown in Figure 4.4(b), where the black branches are connected by the blue nodes. The “AnalyzeSkeleton” plugin of Fiji was used for the skeleton to obtain some quantitative information, including the number of branches, the 3D coordinates of the two nodes which connect each branch and the branches length.

4.2 Geometrical microstructural parameters definition

Usually the quantitative analysis of geometrical microstructure of materials is divided into two categories [134]: (1) the analysis of metric properties, and (2) the analysis of topological properties. Metric properties are those values which depend on the details of shape of the features in the structure, such as relative density, size distribution and specific surface area. Topological properties are those values which are descriptions of the skeleton of the features in the structure, such as connectivity. Except for these two categories, the directional tortuosity can be used to describe the direction related properties. In this section, the approaches of determining these microstructural parameters for the gold phase of npg–epoxy composites are briefly introduced.

4.2.1 Relative density

The solid relative density can be determined by various methods, such as mercury injection method, imbibition method and gas expansion method [135]. For npg, it is normally estimated based on the amount of composition of Au in Au–Ag alloy or using equation (2.1). However, macroscopic volume shrinkage up to 30 vol.% is observed during the dealloying of Au–Ag alloy [136]. If the volume shrinkage is not considered, the relative density can be significantly underestimated. It is also estimated by stereological analysis using the relation: $\rho_{np}/\rho_s = S_A$, where S_A is the area fraction of the gold phase on a 2D image. With the voxel based 3D reconstructions, the gold relative density is directly determined by the ratio of the number of voxels in the gold phase and the total number of voxels in the given volume. An image processing error of $\pm 2\%$ was found by manually changing the image contrast, brightness and threshold value for the segmentation process.

4.2.2 Ligament diameter distribution

The ligament diameter D is usually estimated based on measurements on SEM micrographs of the ligament cross sections using the measurement tool of SEM operation interface or image processing softwares, which is not easy to probe the internal microstructure information. In the present study, it is defined as the thick-

ness at one point within a feature, which is the diameter of the greatest sphere that fits within the feature and includes the point [137]. For example, Figure 4.5 shows a point p in the feature. It is in the sphere that fits within the feature and centers at point o with radius of r . The maximum diameter of the sphere is the thickness of the feature at point p .

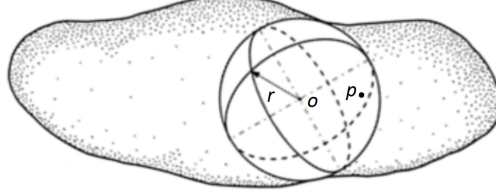


Figure 4.5: Thickness at one point within a feature is defined as the diameter of the greatest sphere that fits within the feature and includes the point. (from [137], reprinted with permission from John Wiley & Sons, Inc.)

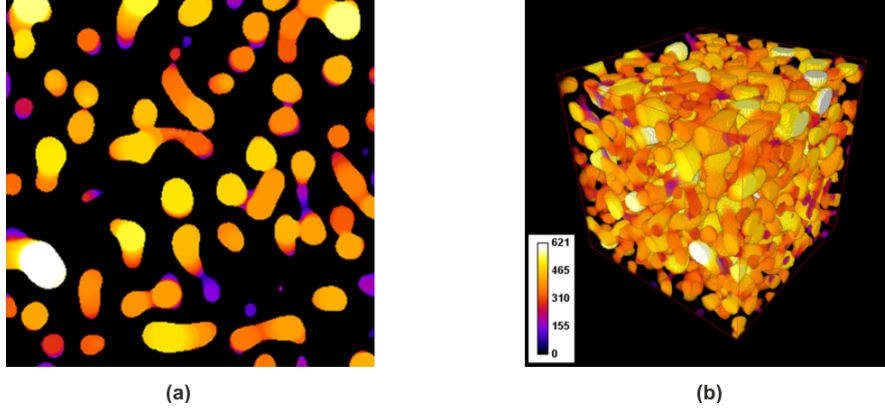


Figure 4.6: (a) Ligament diameter color map of a 2D slice of the 3D reconstruction of sample composite_400nm; (b) ligament diameter color map of a 3D reconstruction of sample composite_400nm. The color bar shows the diameter in nanometer.

For a voxel based 3D reconstruction, at each voxel of a ligament, there is a greatest sphere with a specific diameter that fits within the ligament and includes the voxel. The diameter values vary at different voxels in the ligament structure, creating a ligament diameter distribution. It is worth noting that this method does not handle anisotropic voxels according to the description of the algorithm [137]. Therefore, before calculating the ligament diameter distribution of the reconstructions, the datasets need to be resampled to obtain isotropic voxels. For example, the datasets of sample composite_350nm is resampled by scaling the voxel size from $25.0 \times 25.0 \times 20.0 \text{ (nm)}^3$ to $20.0 \times 20.0 \times 20.0 \text{ (nm)}^3$. This can be easily carried out by increasing the amount of pixels with a factor of $(1.25)^2$ for the stack of images in Fiji. Figure 4.6 shows an example of the ligament diameter color map of the 3D reconstruction of sample composite_400nm. Different colors indicate different

diameter values, which can be obtained to create a ligament diameter distribution. The pore/epoxy diameter distributions can be obtained and visualized using the same approach. It should be noted that since it is not possible to distinguish the ligaments from the nodes, the term “ligament diameter” in this thesis actually means the “solid diameter” of the structure, including the ligaments and the nodes diameter.

4.2.3 Specific surface area

The specific surface area S_V determination is related to various applications of npg associated to the high surface area to volume ratios, such as catalysis, sensing and actuation [1, 2, 5]. A well known approach to determine the specific surface area of nanoporous materials is the Brunauer, Emmett and Teller (BET) method. It is based on the adsorption of nitrogen molecules onto the material surface [138]. Although this method is very reliable, the setups used for the measurement require at least a few hundred milligrams of porous material for a reliable evaluation, which is too much for npg used for common experiments. An analytic, computational and experimental approach using a dimensional analysis for the determination of the surface area based on the information of mean ligament size and relative density was developed recently [139].

With the advantages of the 3D reconstruction, the net surface area of the gold can be determined directly by calculating the surface area of a meshed structure. The specific surface area is determined by calculating the area of the surface meshes S_{gold} per total volume of the sample, including both the gold and the epoxy phases ($V_{total} = V_{gold} + V_{epoxy}$), as shown in equation (4.1).

$$S_V = \frac{S_{gold}}{V_{total}} \quad (4.1)$$

4.2.4 Topology properties

There are two classes of structural aspects related to the topological properties [134]: (1) the amount of fully interconnected parts of the feature in a unit volume of the structure. It can be simply quantified as relative density of the fully interconnected features V_S^* , and (2) the connectivity C of the features in the structure.

When determining the topology properties of a 3D network structure which has been cut from a big volume, one must be aware that the connections will be lost and that isolated components may be created from the cutting process. Figure 4.7(a) and 4.7(b) show the 3D reconstructions of the gold network of sample composite_20nm with a volume of $(600 \text{ nm})^3$ and sample composite_400nm with a volume of $(6 \text{ }\mu\text{m})^3$, respectively. The yellow regions are the interconnected

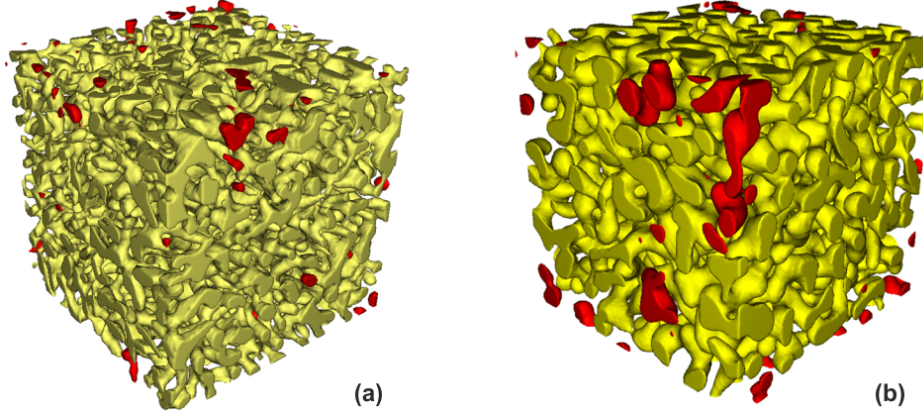


Figure 4.7: (a) A 3D reconstruction of the gold network of sample composite_20nm with a volume of $(600 \text{ nm})^3$; (b) a 3D reconstruction of the gold network of sample composite_400nm with a volume of $(6 \mu\text{m})^3$. The yellow regions show the interconnected gold ligaments, while the red are gold phase, which are not fully interconnected to the remaining structure within the given volume. The volume fractions of the red regions in the left and right figures are 0.2% and 1.1%, respectively.

gold phase, while red are gold phase, which are not fully interconnected to the remaining structure within the given volume. The volume fractions of these “free floating” parts in the left and right figures are 0.2% and 1.1%, respectively. Therefore, the gold ligaments in the given volumes are 99.8% and 98.9% interconnected for the reconstructions (a) and (b), respectively.

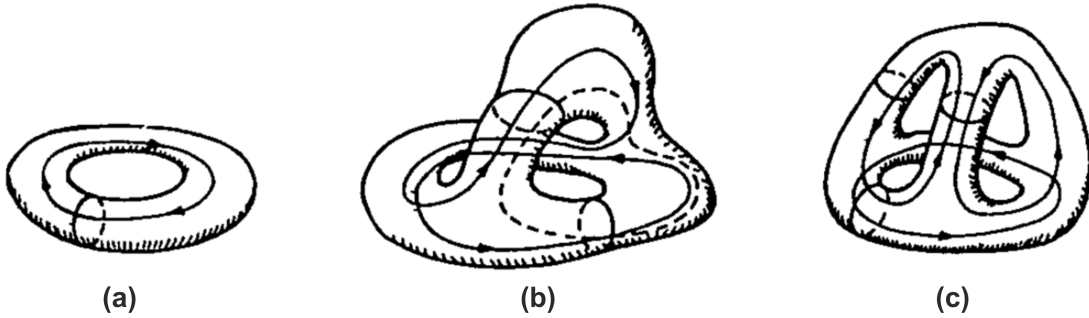


Figure 4.8: Basic understanding of connectivity C and genus G (assume there are no enclosed voids in the features): (a) $C=G=1$; (b) $C=G=2$; (c) $C=G=3$. (from [135], reprinted with permission from Elsevier)

Connectivity is a measure of the degree to which the structure under study is multiply connected. It is defined as the number of nonredundant closed-loop paths by which all regions inside the structure can be inspected [135]. Redundant loops are those that do not give access to any new parts of the structure. The basic topology theorem states that the connectivity of a closed structure is equal to its genus G , assuming that there are no enclosed voids in the features. The genus is the maximum number of branches that may be cut without separating

the structure into disconnected parts [134]. The existence of an enclosed void in the feature results in a decrease of the genus by 1. Connectivity and genus can be simply thought of as the number of ring structures in the volume. A direct understanding of connectivity and genus of a multiply connected and closed structure is shown in Figure 4.8. The first structure is a torus which has one nonredundant closed-loop and can only be cut once without separating it into two pieces. Thus, it has a connectivity or genus of 1. The structure in Figure 4.8(b) has two nonredundant closed-loops and it can be cut twice until it is separated into two parts. The dashed line loop is actually a redundant loop which doesn't occupy any new parts of the structure. Therefore, the connectivity of this structure is 2. Figure 4.8(c) gives an example of a connectivity 3. For npg, the connectivity is important because during microstructure evolution, connectivity may decrease because of ligament pinch-off events [140].

The Euler number χ is the key to the determination of connectivity mathematically. It is related to connectivity and the number of components as shown in equation (4.2):

$$\chi = \beta_0 - \beta_1 + \beta_2 \quad (4.2)$$

where β_0 is the number of components, β_1 is the number of nonredundant closed-loop paths, which equals to the connectivity, and β_2 is the number of enclosed voids fully surrounded by the components, respectively. The Euler number can be calculated from the voxel-based datasets of the 3D reconstructions. If the isolated components are removed in a purification step due to the very low volume fraction and only the fully interconnected components are considered in the analysis, i.e., no isolated parts are taken into account ($\beta_0 = 1$), and the possible existence of enclosed voids are neglected ($\beta_2 = 0$), equation (4.2) simplifies to:

$$\chi = 1 - \beta_1 \quad (4.3)$$

In a voxel-based 3D reconstruction, the Euler number χ can be determined from the number of voxel corners α_0 , voxel edges α_1 , voxel faces α_2 , and voxel volumes α_3 as:

$$\chi = \sum (-1)^i \alpha_i = \alpha_0 - \alpha_1 + \alpha_2 - \alpha_3 \quad (4.4)$$

Thus, β_1 , i.e. the connectivity can be resolved with equation (4.3) and (4.4).

It should be noted that the cutting process stated previously leads to a biased estimation of connectivity since for a structure with limited volume, it is impossible to know exactly how the volume is connected by its boundaries. For example, on the one hand, the ligaments at the edge of the volume might have connected with each other, however, because of the cutting process, the connections are destroyed. On the other hand, there might be not any connections among the ligaments at the edge as well. The correct value of connectivity of the structure should be between

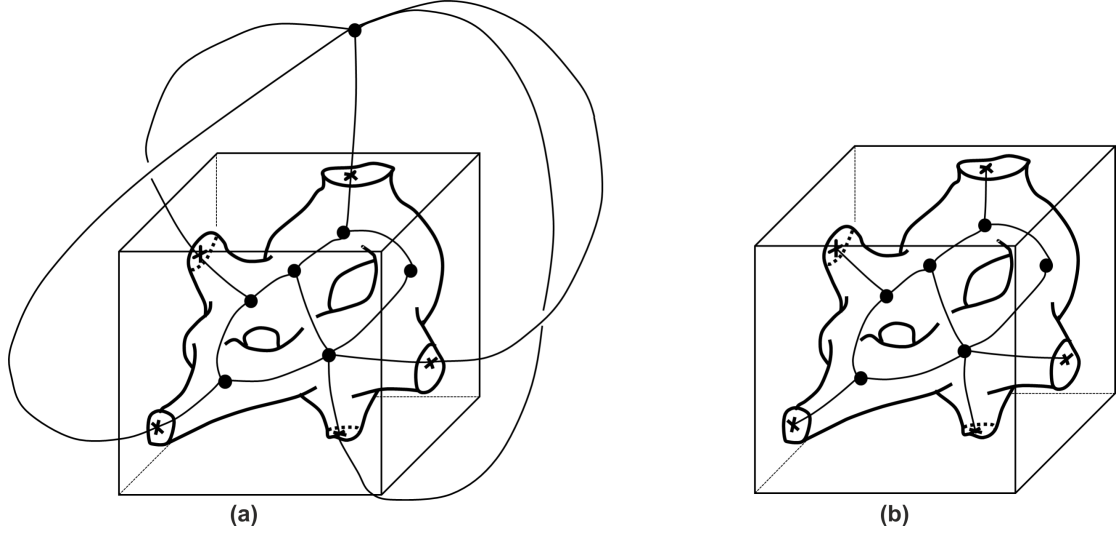


Figure 4.9: A schematic illustration of the two extremes of connectivity: (a) all branches crossing the boundary connected to the external node, $C=6$; (b) all branches capped at the sample surface, $C=2$. (from [134], reprinted with permission from John Wiley & Sons, Inc.)

these two extremes [134], which are shown schematically in Figure 4.9. This edge problem can be considered by using the *addition theorem* to estimate the Euler characteristic of the intersection of two sets S_1 and S_2 [141], as expressed as:

$$\chi(S_1 \cup S_2) = \chi(S_1) + \chi(S_2) - \chi(S_1 \cap S_2) \quad (4.5)$$

It shows that the intersections of lower dimensional elements on the volume surface must be taken into account.

In the present study, an unbiased quantification of connectivity that is free of geometric assumptions was carried out for the voxel based dataset of the 3D reconstructions using the algorithm described in [134, 141, 142]. This algorithm has been implemented into the BoneJ plugin for the Fiji software. It firstly uses voxel neighbourhoods to calculate the Euler characteristic of the volume χ as if it is floating in space. Then it calculates the contribution of the volume to the Euler characteristic of the entire structure it was cut from by checking the lower dimensional elements at the intersections, such as corners, edges and faces on the voxels [143]. The contribution $\Delta\chi$ is expressed as:

$$\Delta\chi = \chi - \frac{1}{2} \sum_1^6 \chi(F) + \frac{1}{4} \sum_1^{12} \chi(E) - \frac{1}{8} \sum_1^8 \chi(P) \quad (4.6)$$

where $\chi(F)$, $\chi(E)$ and $\chi(P)$ are the Euler characteristic of the face, the edge and the corner on the voxels at the intersect surface of the volume, respectively. A face is shared by two voxels, an edge is shared by four voxels, and a corner

is shared by eight voxels, which is the reason of different denominators in the equation [141]. The details of the algorithm can be found in [134, 141, 142]. The fully interconnected ligaments were taken into account by deleting the floating ligaments using the “purify” option of Fiji. Since the connectivity naturally scales with the volume, the connectivity density C_V is used, giving the connectivity per unit sample volume.

4.2.5 Directional tortuosity

Tortuosity usually describes the influence of the morphology of a porous media on its effective transport properties [144]. There are many definitions of tortuosity [145]. The most straightforward and frequently used definition is the distance metric tortuosity τ , which is the ratio of the actual path length of a curve along certain direction and the linear distance between the end points [146], as given by:

$$\tau = \frac{l_0}{L_0} \quad (4.7)$$

where l_0 is the actual path length and L_0 is the linear distance. Thus, a straight channel gives tortuosity of 1. A curved pore channel inside a porous material increases the length of the transport paths and therefore increase the tortuosity.

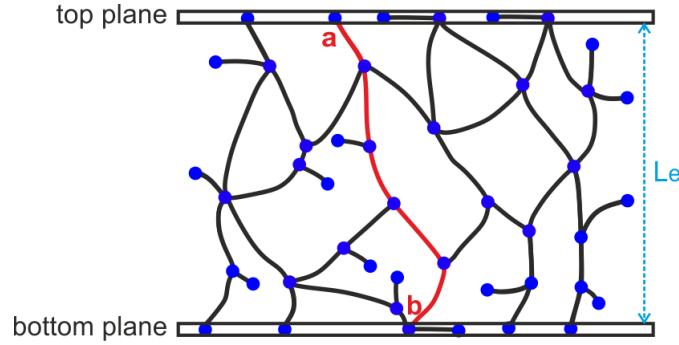


Figure 4.10: A 2D schematic graph of a skeleton shows the dead-end nodes, nodes on the sample surface plane, triple junctions and quadruple junctions. The shortest path L_p from node a to b is shown in red and the distance between the top and the bottom plane is L_e . The directional tortuosity between a and b is L_e/L_p . The average directional tortuosity between the node pairs on the top and the bottom planes give the directional tortuosity of the entire skeleton.

In the present work, it is of interest to investigate how the load may be transferred through the gold network structure. The directional tortuosity τ_D serves as such a characteristic, which can be correlate to the mechanical response. It is defined as the ratio of the averaged shortest path length L_p between two parallel planes of the volume over all pairs of nodes on the top and the bottom planes of the volume to the euclidean distance between the top and the bottom plane L_e . Figure 4.10 is a 2D schematic of a skeleton of ligament structure showing

dead-end nodes, nodes on the sample surface planes, triple nodes and quadruple nodes. The highlighted path in red gives an example of the shortest path. Apparently, there are several paths from node a to node b . However, the shortest length is shown in red. Each node on the top plane can find a shortest path to reach a corresponding node on the bottom plane. The average length of all the shortest paths in the loading direction is obtained and is used for the calculation of directional tortuosity in this direction.

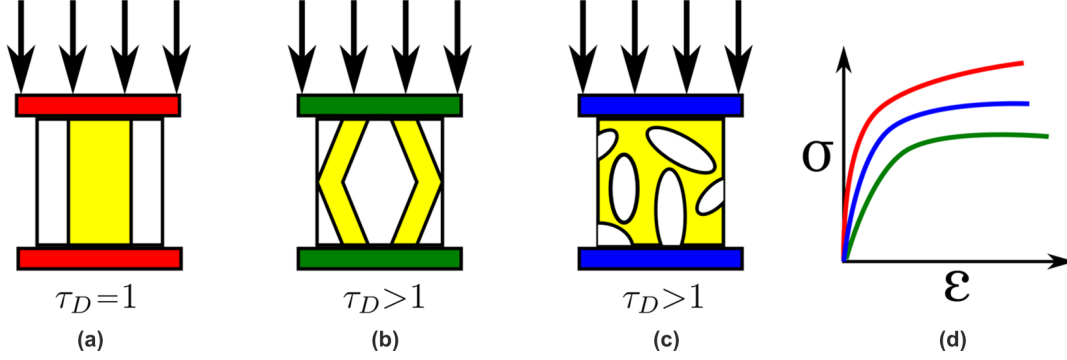


Figure 4.11: Schematic showing how structures with constant volume fraction but different directional tortuosity exhibit different stress-strain behaviors: (a) $\tau_D=1$; (b) $\tau_D>1$; (c) $\tau_D>1$; (d) possible stress-strain curves.

The directional tortuosity reflects the load transfer capability of the structure in different directions. Figure 4.11 shows schematically how can three equivalent volume fraction microstructures be distinctively arranged. Figures 4.11(a), 4.11(b), and 4.11(c) show the material with three different microstructures but the same volume fractions. The same amount of load is applied in the same direction. The possible stress-strain curves are shown in Figure 4.11(d). It can be imagined that with a smaller directional tortuosity, the structure is stiffer due to a shorter load transfer path. Even with the same directional tortuosity, the mechanical response can be different, depending on other structural parameters, such as the size distribution and the connectivity.

Practically, only fully interconnected ligaments within the investigated volume are taken into consideration, so that any nodes are accessible from any other arbitrary nodes within this volume. Graph theorists have developed a number of algorithms to calculate the shortest path and corresponding distance between all pairs of nodes in a graph. These can then be averaged after division by the distance between the top and the bottom surface to determine the tortuosity in the loading direction. Using graph theory requires a very clear representation of the network of the structure, which can be achieved from the 3D skeletonization analysis, as introduced in section 4.1.4. Before implementing the skeletonization process, the floating ligaments of the volume were deleted using the “purify” option of Fiji, such that the branches of the ligament skeleton are fully interconnected.

In order to calculate all the shortest paths and their length based on the 3D skeleton, a Python language script was written using a modified Dijkstra algorithm based on the Python language software package NetworkX, which has already been used for studying complex network structures [147]. Directional tortuosities along different directions in the reconstructions were calculated and their influence on the mechanical anisotropy of the npg network was presented in Chapter 5.

4.3 Representative volumes

A critical problem in quantitative 3D microstructural analysis is establishing a statistically representative structure. This problem might be caused by limited volume of analyzed material. A representative volume (RV) is defined as a volume sufficiently large to be statistically representative of the entire sample's microstructure, and it represents the mechanical behavior of the sample with a desirable accuracy. The mechanical behavior of RVs are introduced in Chapter 5 based on finite element simulations on the meshed 3D reconstructions. Here the determination of microstructural RVs of the 3D reconstructions of the five samples and their quantitative analyses are presented.

4.3.1 RVs determination

The microstructural RVs were identified from the microstructural parameters of the gold phase, i.e., relative density, mean ligament diameter, specific surface area and connectivity density. In order to quantify the 3D structures systematically, considering both spatial variations and volume dependence, the 3D reconstruction datasets of each sample were divided into 6 cubic regions with a constant volume, as shown in Figure 4.12. The volume of each region is summarized in Table 4.1. Each region was subdivided into 8–15 smaller cubes with increasing cubic length. The microstructural parameters of each cube were analyzed. The combined spatial variations and volume dependent analyses were carried out for the 3D reconstructions of the five samples.

Figures 4.13–4.17 show the analyzed microstructural parameters as a function of the cubic length of the 3D reconstructions of the five samples. The results of the six regions are plotted with the same colors as the region numbers shown in Figure 4.12. As can be seen, for all the five reconstructions, the parameters exhibit big variations until they converge to constant levels with increasing cubic length. The cubic volume corresponding to the point of convergence defines the RV of the gold network. The RV sizes are summarized in Table 4.1. The same analysis can be performed for epoxy phase. Since the npg–epoxy composites have bicontinuous structure, the volume of the epoxy phase is the difference of the total volume of the cube and the volume of the gold phase, and the epoxy phase has the same

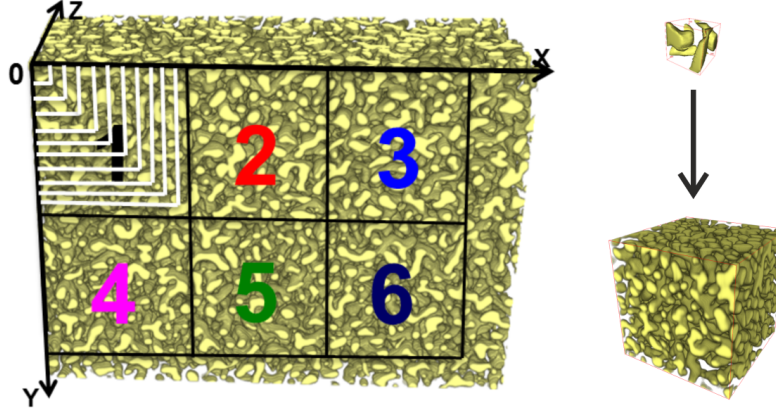


Figure 4.12: A combined spatial variation and volume dependent analysis of the gold network: the 3D reconstruction datasets of each sample were divided into 6 cubic regions with constant volume, and each region were subdivided into 8–15 smaller cubes with increasing cubic length. Each cube was quantitatively analyzed in terms of its microstructural parameters to determine the microstructural RVs.

specific surface area and topology properties as the gold phase. The RV sizes of the gold phase are applicable to the epoxy phase as well.

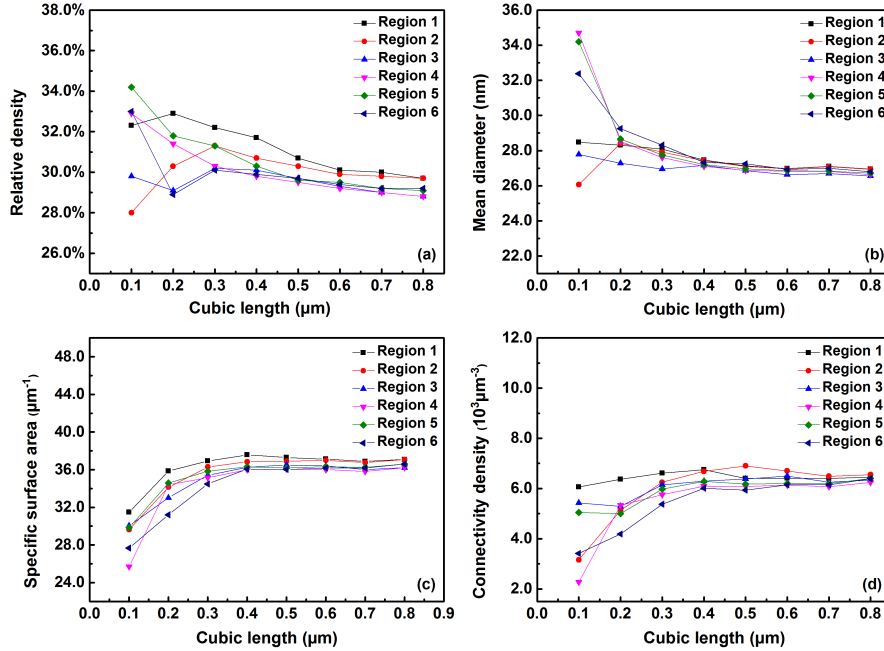


Figure 4.13: Microstructural parameters of the gold phase as a function of cubic length of sample composite.20nm: (a) relative density; (b) mean diameter; (c) specific surface area; (d) connectivity density. The parameters converge to constant levels when the cubic length is beyond 0.4 μm. The microstructural RV size was estimated as ~ 0.6 μm.

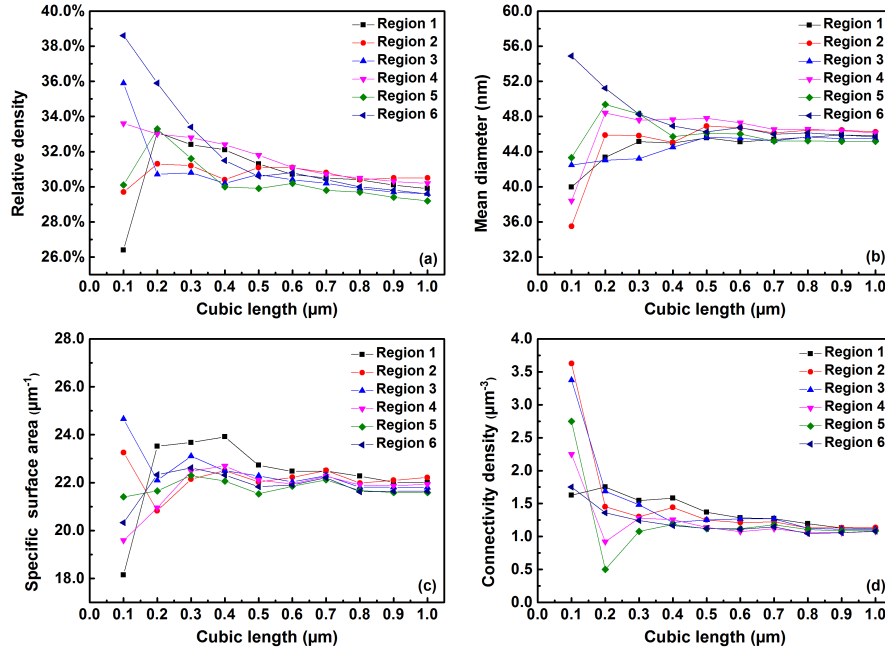


Figure 4.14: Microstructural parameters of the gold phase as a function of cubic length of sample composite_50nm: (a) relative density; (b) mean diameter; (c) specific surface area; (d) connectivity density. The parameters converge to constant levels when the cubic length is beyond $0.5 \mu\text{m}$. The microstructural RV size was estimated as $\sim 0.7 \mu\text{m}$.

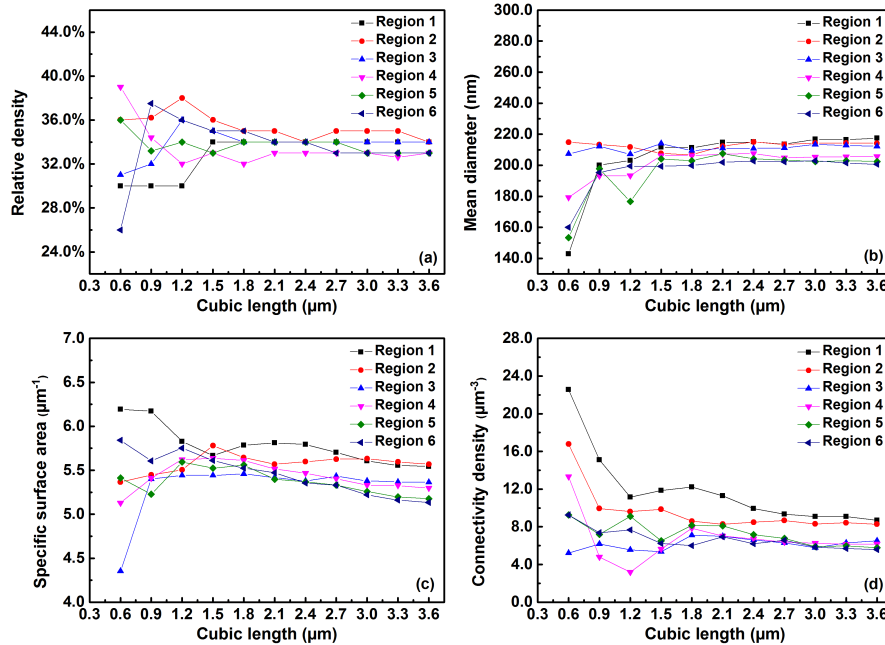


Figure 4.15: Microstructural parameters of the gold phase as a function of cubic length of sample composite_200nm: (a) relative density; (b) mean diameter; (c) specific surface area; (d) connectivity density. The parameters converge to constant levels when the cubic length is beyond $1.8 \mu\text{m}$. The microstructural RV size was estimated as $\sim 2.1 \mu\text{m}$.

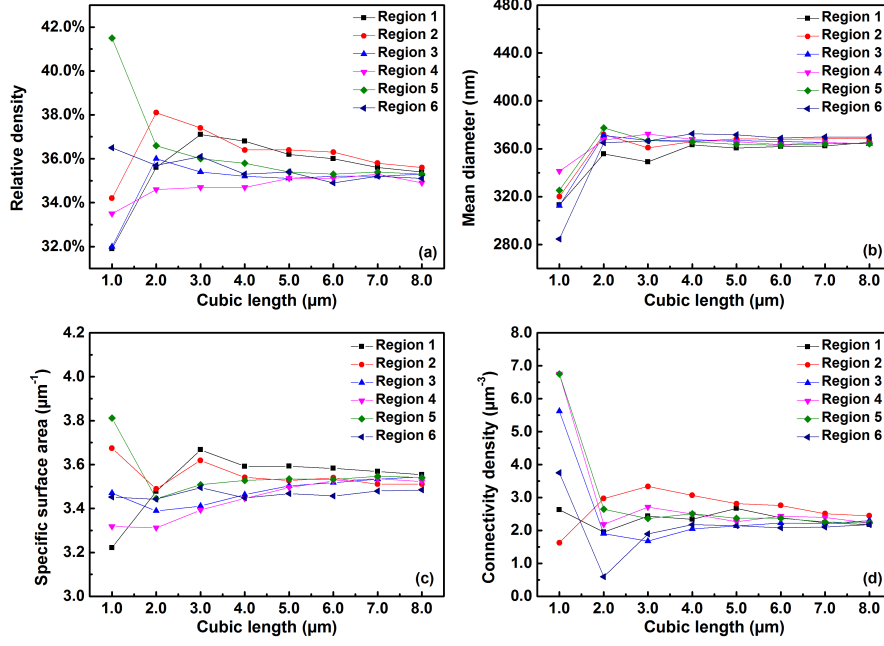


Figure 4.16: Microstructural parameters of the gold phase as a function of cubic length of sample composite_350nm: (a) relative density; (b) mean diameter; (c) specific surface area; (d) connectivity density. The parameters converge to constant levels when the cubic length is beyond 4.0 μm . The microstructural RV size was estimated as $\sim 6.0 \mu\text{m}$.

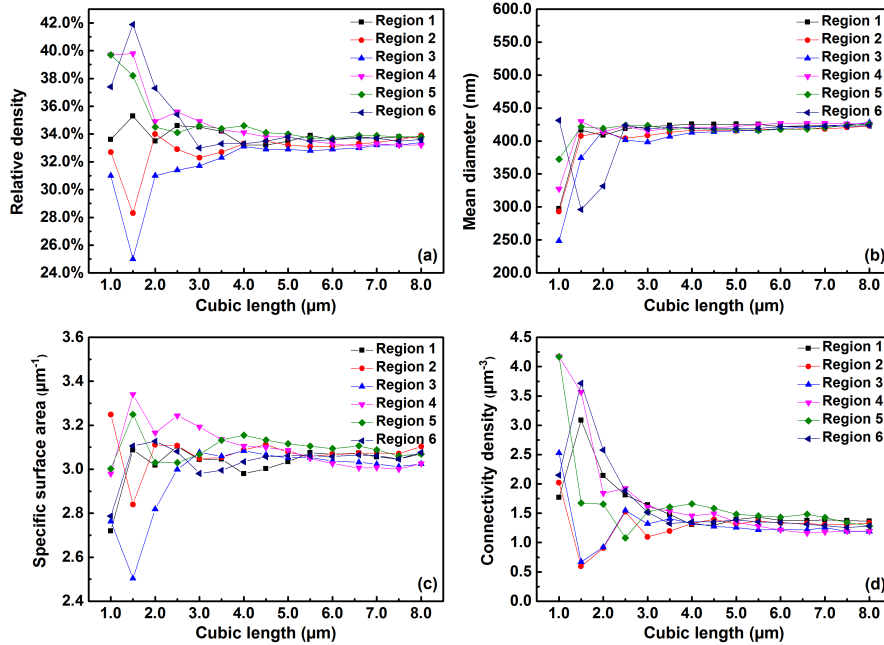


Figure 4.17: Microstructural parameters of the gold phase as a function of cubic length of sample composite_400nm: (a) relative density; (b) mean diameter; (c) specific surface area; (d) connectivity density. The parameters converge to constant levels when the cubic length is beyond 4.0 μm . The microstructural RV size was estimated as $\sim 6.0 \mu\text{m}$.

Table 4.1: Volume of each region shown in Figure 4.12, and microstructural RVs of the gold phase determined from quantitative analyses of the 3D reconstructions of the five samples.

Sample	Volume of each region	Volume of RVs
composite_20nm	$(0.8 \mu\text{m})^3$	$(\sim 0.6 \mu\text{m})^3$
composite_50nm	$(1.0 \mu\text{m})^3$	$(\sim 0.7 \mu\text{m})^3$
composite_200nm	$(3.6 \mu\text{m})^3$	$(\sim 2.1 \mu\text{m})^3$
composite_350nm	$(8.0 \mu\text{m})^3$	$(\sim 6.0 \mu\text{m})^3$
composite_400nm	$(8.0 \mu\text{m})^3$	$(\sim 6.0 \mu\text{m})^3$

4.3.2 Quantitative analyses of RVs

Since the RVs are supposed to capture representative microstructural information, the quantitative results of RVs are considered to represent the microstructure properties of the correspondent material. Table 4.2 summarizes the RVs size of each sample and the correspondent relative density, mean diameter, specific surface area and connectivity density of the gold phase. These results are derived

Table 4.2: Quantitative microstructural analyses results of the gold phase RVs of the five samples (L_{RV} : cubic length of a RV; ρ_{np}/ρ_s : relative density; $\langle D \rangle$: mean ligament diameter; S_V : specific surface area; C_V : connectivity density).

Sample	$L_{RV} (\mu\text{m})$	ρ_{np}/ρ_s	$\langle D \rangle (\text{nm})$	$S_V (\mu\text{m}^{-1})$	$C_V (\mu\text{m}^{-3})$
composite_20nm	~ 0.6	$(29.6 \pm 0.4)\%$	27 ± 0	36.5 ± 0.5	$(6.4 \pm 0.2) \times 10^3$
composite_50nm	~ 0.7	$(30.4 \pm 0.4)\%$	45 ± 1	22.3 ± 0.2	$(1.2 \pm 0.1) \times 10^3$
composite_200nm	~ 2.1	$(34.0 \pm 0.6)\%$	210 ± 5	5.5 ± 0.2	8.1 ± 1.7
composite_350nm	~ 6.0	$(35.5 \pm 0.6)\%$	365 ± 3	3.5 ± 0.0	2.4 ± 0.2
composite_400nm	~ 6.0	$(33.4 \pm 0.3)\%$	421 ± 4	3.1 ± 0.0	1.3 ± 0.1

from the average results of the six regions at the RV size, and the error is the standard deviation. It was found that the gold relative density is ranging from 29%–35% for the five samples. The results are actually very consistent for all the samples if image processing errors ($\pm 2\%$) are considered. As can be seen from Table 4.2, the specific surface area decreases with increasing the mean ligament diameter. The difference between the smallest and the biggest ligament diameter samples is more than one order of magnitude. The possible influences of specific surface area on the mechanical behavior of npg–epoxy composites were discussed in Chapter 6. The inverse of specific surface area scales linearly with the mean ligament diameter, as shown in Figure 4.18.

The scaling effect is also reflected in the mean ligament diameter. It was found that the cubic length of the RVs scales with the mean ligament diameter with a factor of around 15. This observation of linearly scaling supports the self-similarity of the npg network, as revealed by the visually indistinguishable structures shown

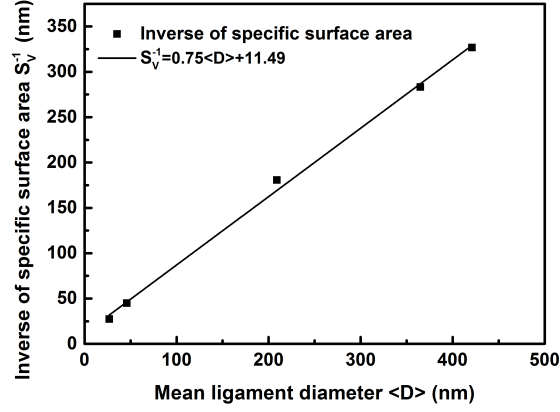


Figure 4.18: Plot of the inverse of specific surface area S_V^{-1} vs. the mean ligament diameter $\langle D \rangle$. A linear fit to the data points reflects the direct proportionality of S_V^{-1} and $\langle D \rangle$.

in Figure 4.7. The quantitative analysis of the self-similarity of npg coarsening has been investigated in terms of its metric and topological structural properties, i.e., ligament diameter distribution and scaled connectivity density [148]. The scaled ligament diameter distribution of a RV of sample composite_400nm is shown in Figure 4.19(a). It is normalized to area 1 and could be fitted by a Gaussian function. Figure 4.19(b) shows the scaled ligament diameter distributions of the RVs

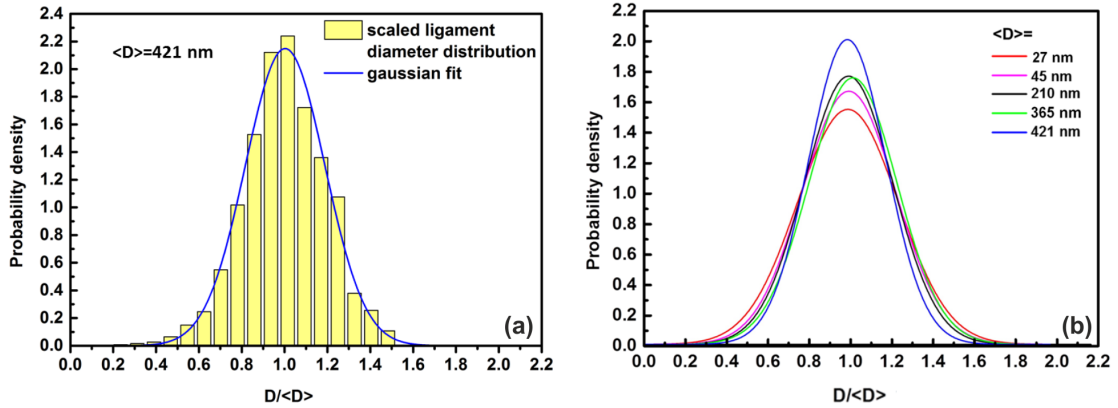


Figure 4.19: (a) Scaled ligament diameter distribution, normalized to area 1 and Gaussian fits for the RV of sample composite_400nm (ligament diameter 3D color map is shown in Figure 4.6); (b) Gaussian fits to the scaled ligament diameter distributions normalized to area 1 for the RVs of the five samples.

of the five samples. As can be seen, the center positions are very close to one and the full width at half maximum values of the Gaussian fits are nearly constant, which indicates that ligament diameter distributions of the RVs of as-dealloyed and isothermally annealed npg structures are nearly self-similar, at least in the investigated early and mid stages of coarsening. The differences of the distributions might be attributed to the 3D reconstruction error in the slicing direction,

as introduced in Chapter 3. The spacing between the slices which compose the 3D reconstructions may significantly deviating from the constant value set in the “auto slice and view” script or the average value, as used in the present study. The constant slice thickness used in the reconstruction may lead to a bigger ligament diameter and a larger spread in the ligament diameter distribution compared to a reconstruction using the actual slice thickness, which was accurately determined recently by using a well-defined wedge-shaped geometry trench for the volume of interest of a npg sample in the “auto slice and view” procedure [149]. This error analysis was not taken into account in the present work. Nevertheless, an kinetics analysis of the coarsening behavior of the five samples revealed that the growth exponent of the npg structure is very close to 4 [148]. This value is expected for surface diffusion dominated coarsening which support the view of self-similar npg microstructure evolution [140, 148, 150].

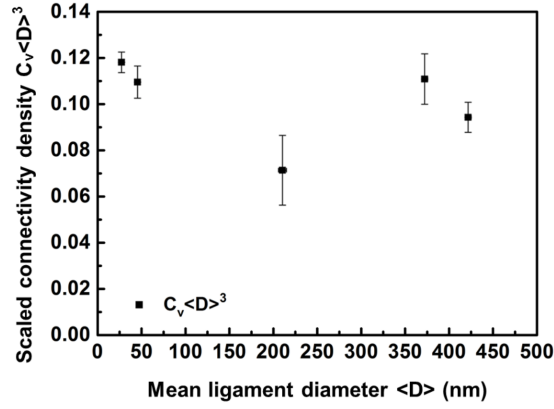


Figure 4.20: The scaled connectivity density of the five samples are nearly constant at around 0.1, which indicates that the npg structure are nearly topologically self-similar.

The topology properties are also very important for the understanding of the self-similar coarsening behavior. During the microstructure evolution, topologically singular events such as ligaments collapse and pinch-offs must occur in order to establish the self-similarity [140, 148, 151]. This will lead to the loss of connectivity with coarsening time. It was found that the difference of connectivity density between the smallest and the biggest mean ligament diameter samples in the present work are more than 3 orders of magnitude, as can be seen from Table 4.2. Interestingly, the inverse of the connectivity density actually reflects the total volume per ring structure, including the ligament and the pore. Thus, the number of rings in a characteristic volume $\langle D \rangle^3$ is $C_V \langle D \rangle^3$ [148]. $C_V \langle D \rangle^3$ is a dimensionless parameter that enables to compare npg microstructure with varying mean ligament diameters directly. The effects due to the varying length scales of ligaments as the microstructure evolution is avoided. That is to say, the changes of the scaled connectivity density are due to the topological evolution during the

coarsening process instead of a change in the ligament length scale. For the five samples used in the present studies, it was found that the scaled connectivity density are nearly constant at around 0.10 [148], as shown in Figure 4.20. This indicates that the npg structure is topologically self-similar as well. The self-similarity has also been discussed in terms of the principle curvatures of the ring structure recently [152]. It enables to identify the critical structural parameters which can be used to describe the mechanical behavior of the global npg structure over varying length scales. Thus, it is possible to investigate the applicability of Gibson–Ashby scaling relations for the prediction of the mechanical properties of npg.

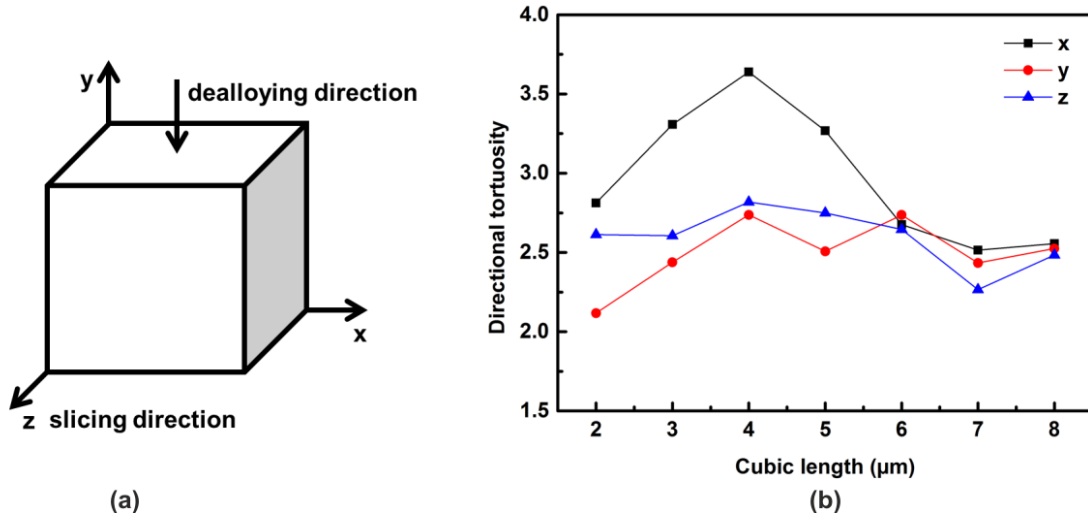


Figure 4.21: Directional tortuosity results of the gold network in region 1 of sample composite_400nm: (a) three directions (x, y, z) of the reconstructions: y is the dealloying direction and z is the FIB slicing direction; (b) directional tortuosity as a function of cubic length of the 3D reconstruction. The differences of directional tortuosities in the three directions decrease remarkably when the cubic length approaches 6 μm .

It should be noted that the RVs determination presented in this section considers three metric properties and one topology property, which are descriptions of the global structure of the gold phase. Apart from these, the directional tortuosity was analyzed to investigate the direction related microstructure property. Figure 4.21(b) shows the directional tortuosities in the three directions (x, y, z) as a function of cubic length of the npg 3D reconstructions of sample composite_400nm region 1. The cubic length is ranging from 2 to 8 μm . As shown in Figure 4.21(a), y is the dealloying direction of the npg sample synthesis, and z is the FIB slicing direction in the FIB–SEM tomography experiment. As can be seen from Figure 4.21(b), the differences of directional tortuosities in the three directions decrease remarkably when the cubic length approaches 6 μm , which is

in the range of RV size of sample composite. 400nm determined previously. The strong anisotropy results below RV size could be a finite volume effect. Above the RV size, the slight differences of the directional tortuosities in the three directions of each cube might be attributed to the inherent nature of npg microstructure and possible image processing error. It is observed that the smallest directional tortuosity always appears in the z direction, which is the FIB slicing direction of the “auto slice and view” procedure. This procedure may lead to errors in the voxel size determination, which degrade the accuracy of the 3D reconstructions. As a consequence, the directional tortuosities in this direction differ from others. Additionally, it is unknown how the dealloying process influences the directional property, which is out of the scope of the present work.

4.4 Conclusions

In this chapter, a 3D microstructural characterization approach for npg network structure was established using FIB–SEM tomography for the npg–epoxy composite samples, which were produced from as–dealloyed to isothermally annealed npg with mean ligament diameters of 27 nm, 45 nm, 210 nm, 365 nm and 421 nm. The 3D reconstructions were quantitatively analyzed. With the 3D microstructure information, RVs of the gold phase structure of the composites, which is assumed to be equivalent to the pure npg structure were determined. The RV sizes were about 15 times the mean ligament diameter. It was found that the npg structure coarsens in a nearly self–similar manner in terms of the ligament diameter distribution and the scaled connectivity density. The self–similarity allows to identify critical structural parameters that can be used to describe the npg structure with varying length scale. Importantly, the meshed 3D reconstructions allow for investigating the correlation between the structural geometry and the mechanical behavior directly by FEM simulations, which will be introduced in Chapter 5 and 6.

In conclusion, it is the first time that npg from as–dealloyed to isothermally annealed structures were characterized in three dimensions systematically. The work presented in this chapter is the basis for the understanding of mechanical behavior of npg and npg–epoxy composites in this thesis.

5. Mechanical behavior of Npg

In order to identify the critical structural parameters which can be used to describe the mechanical behavior of npg, a combined experimental and FEM simulation approach is presented in this chapter. It is assumed that the microstructure of the pure npg is well described by the ligament network of the infiltrated npg–epoxy composite. Therefore, it is possible to use the structural geometry of the npg 3D reconstructions to represent the microstructure of pure npg. Additionally, as discussed in Chapter 4, npg coarsens in a nearly self-similar manner, which allows to take the npg structure with a specific mean ligament diameter as the model system for the investigations. In this chapter, the npg network with a mean ligament diameter of about 400 nm was focused on. The sample npg_400nm and the 3D reconstructions of the gold phase of sample composite_400nm were used. Firstly, the micromechanical experiments for sample npg_400nm is presented. FEM simulations on the meshed 3D reconstructions of the gold phase RV of sample composite_400nm are compared with the experimental results of the pure npg sample secondly. Finally, the correlations between mechanical behavior and structural parameters and their implications on the Gibson–Ashby scaling relations were discussed.

5.1 Micromechanical characterization

5.1.1 Nanoindentation

Nanoindentation testing with a Berkovich and a flat punch indenter were carried out for sample npg_400nm. The load–displacement curves of the Berkovich indentation in CSM mode are shown in Figure 5.1(a). The mean elastic modulus measured from 10 measurements with the indentation depths ranging from 1000 to 3000 nm is (227 ± 30) MPa and the mean hardness is (10 ± 1) MPa. The load–displacement curves of the flat punch indentation testing are shown in Figure 5.1(b). As can be seen, the elastic modulus increases as the indentation depth increases, ranging from 160 MPa to 250 MPa, which indicates densification of the npg structure, as expected.

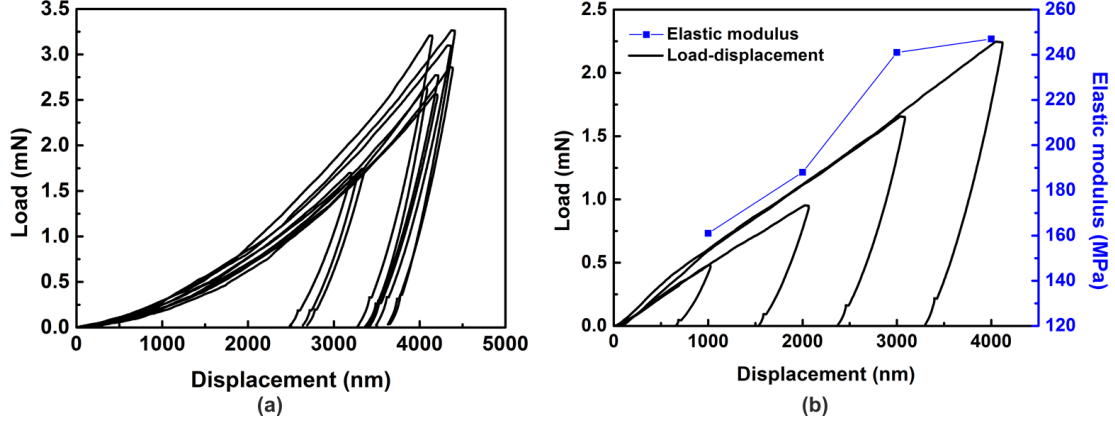


Figure 5.1: Load–displacement of nanoindentation testing with (a) a Berkovich indenter, the elastic modulus and the hardness from CSM are (227 ± 30) MPa and (10 ± 1) MPa, respectively; (b) a flat punch indenter, the elastic modulus determined from the unloading segment is ranging from 160 MPa to 250 MPa.

5.1.2 *In-situ* microcompression

An *in-situ* microcompression experiment on sample npg_400nm was carried out in an InSEM nanoindentation system (Nanomechanics, Inc.), equipped with a $20 \mu\text{m}$ diameter flat punch indenter. The loading profile consists of four loading–unloading segments at different strains, followed by compression to a maximum displacement of about 23% of the column height at a strain rate of 0.05/s and a full unloading finally. During the test, high resolution SEM images of the surface with a normal perpendicular to the loading axis and parallel to the electron beam were captured for a digital image correlation analysis.

Figure 5.2(a) shows the rectangular microcolumn with a height of $17 \mu\text{m}$ and a width of $7 \mu\text{m}$. The flat punch indenter starts touching the top surface of the microcolumn. The geometry of the microcolumn at maximum displacement is shown in Figure 5.2(b). It was observed that some of the ligaments on the side surface contacted with each other, while the width of the microcolumn remains constant, which indicates the densification of npg, and this will lead to stiffening of the material.

For the DIC analysis, the ligament network structure was used as a speckle pattern, which allows to measure the displacement and the strain distribution in the side plane. A DIC subset radius of 28 pixels and a spacing of 2 pixel were used in the analysis. The DIC error analysis for the SEM images of the microcolumn side plane before loading shows that the displacement and the strain field due to the SEM imaging artifacts are quite small compared to the total displacement and the applied deformation of the microcompression testing. Figure 5.2(c) shows the lateral strain distribution of the microcolumn. It was found that the global lateral strain ε_{xx} is close to zero which indicates that there is almost no lateral expansion.

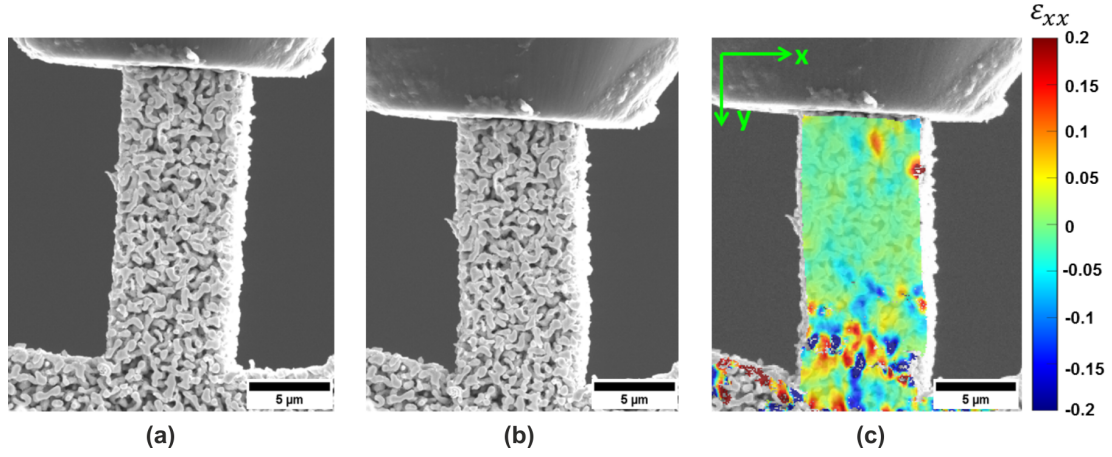


Figure 5.2: (a) A rectangular microcolumn with a height of $17\ \mu\text{m}$ and a width of $7\ \mu\text{m}$. The flat punch indenter starts touching the top surface; (b) the microcolumn at maximum displacement shows densification and little lateral expansion; (c) the DIC strain map of the microcolumn at maximum displacement shows near zero global lateral strain and strain localizations.

This confirms the near zero Poisson's ratio of npg observed from other investigations [24,27]. Additionally, there are strain localizations at some ligaments, which are attributed to their irregular structure.

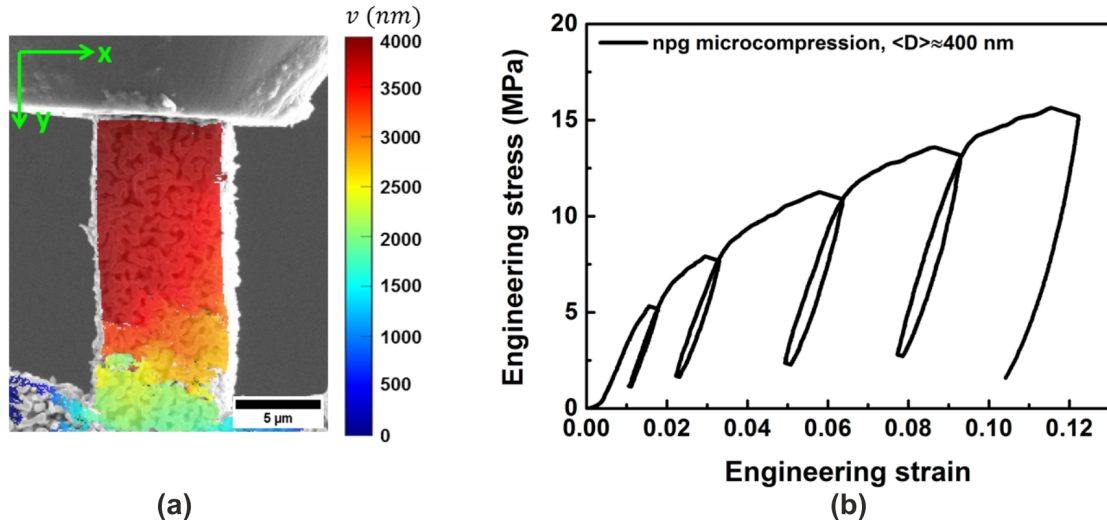


Figure 5.3: (a) The DIC displacement map of the microcolumn in the loading direction at maximum displacement. The actual displacement of the microcolumn calculated by taking the difference of the top and the substrate displacement of the microcolumn is about $2000\ \text{nm}$, which indicates that the displacement taken directly from the indenter was about 50% overestimated; (b) calibrated engineering stress-strain of the *in-situ* microcompression testing of sample npg_400nm.

Since it was observed that there is a strong deformation of the substrate under-

neath the microcolumn, the axial displacement of the microcolumn was calibrated by the DIC measurement, as shown in Figure 5.3(a). It was found that the displacement taken directly from the indenter was about 50% overestimated. The calibrated stress-strain curve of the microcompression testing is shown in Figure 5.3(b). The elastic modulus determined from the first unloading segment was about 650 MPa and the yield stress around 8 MPa. The ratio of the hardness taken from nanoindentation and the yield stress taken from microcompression is close to 1, which supports the similar argument that stated in the literature [24, 27]. The difference of elastic modulus obtained from the nanoindentation and the microcompression testing might be attributed to the different mechanical properties of the material on the surface and in the internal volume of the sample. Nevertheless, all the elastic moduli are around a few hundred MPa, which are significantly lower than most of the experimental results previously reported, as plotted in Figure 2.3. Additionally, a hysteresis is observed in the unloading-reloading segments, which might be caused by local plastic deformation and residual stress.

5.2 Mechanical behavior of structural geometry

FEM simulations were carried out for the 3D meshed reconstructions in order to understand the mechanical behavior of npg structural geometry. In this section, the mechanical behavior RV determination, the mechanical anisotropy and the mechanical behavior of a RV of the npg network with a mean ligament diameter of 421 nm are presented firstly. The mechanical behavior self-similarity of the RVs are discussed secondly, focusing on the npg networks with mean ligament diameters of 45 nm, 210 nm and 421 nm.

5.2.1 Determination of a mechanical RV

In Chapter 4, the microstructural RVs of the gold phase were identified for each composite sample. The RV is defined as the minimal material volume that represents the microstructure of the global npg structure. It is interesting to know if these microstructural RVs also serve as mechanical RVs. That is to say, that the mechanical response is no longer dependent on the volume of the material. Similar to the determination of microstructural RVs, a sampling scheme was implemented to the 3D reconstructions to explore the effect of finite volume in terms of the mechanical response. Figure 5.4(a) shows the 3D mesh of a microstructural RV ($6 \times 6 \times 6 \mu\text{m}^3$) of npg with a mean ligament diameter of 421 nm. The floating ligaments produced by the volume cut at the edges which do not carry load and account for less than 2% of the whole npg volume were deleted, such that the ligament structures under investigation were fully interconnected. As illustrated in Figure 5.4(b), a big square region of sample composite_400nm was divided into

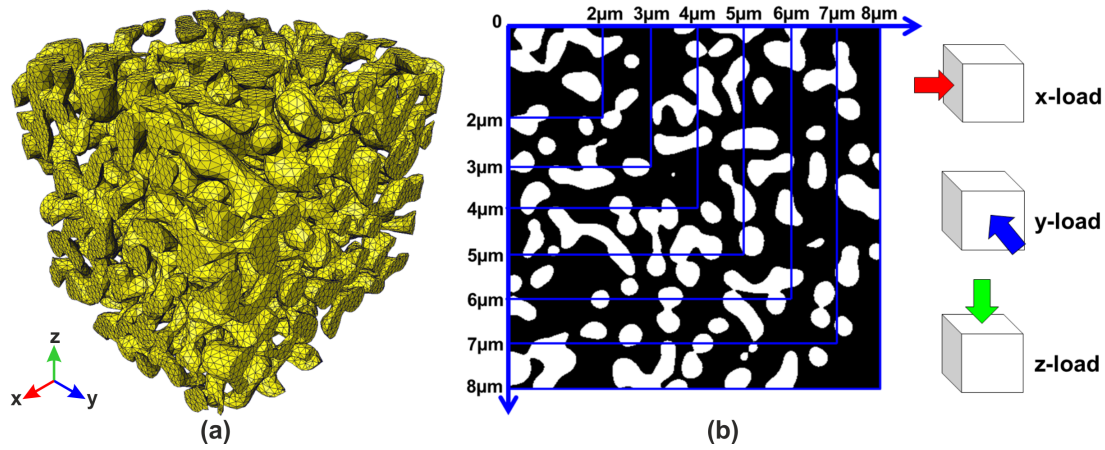


Figure 5.4: (a) 3D mesh of a reconstructed RV ($6 \times 6 \times 6 \mu\text{m}^3$) of the gold network. Floating ligaments at the edges were deleted; (b) mechanical behavior RV determination and mechanical anisotropy investigation: the 3D reconstructions were divided into cubes with length of 2–8 μm for the simulations. Each cube was loaded in three orthogonal directions.

7 smaller regions with a length ranging from 2 to 8 μm . These regions were then reconstructed into 3D and the gold network is meshed for FEM simulations using the same boundary conditions and material properties. The mechanical responses in the x, y and z directions from the simulations were obtained.

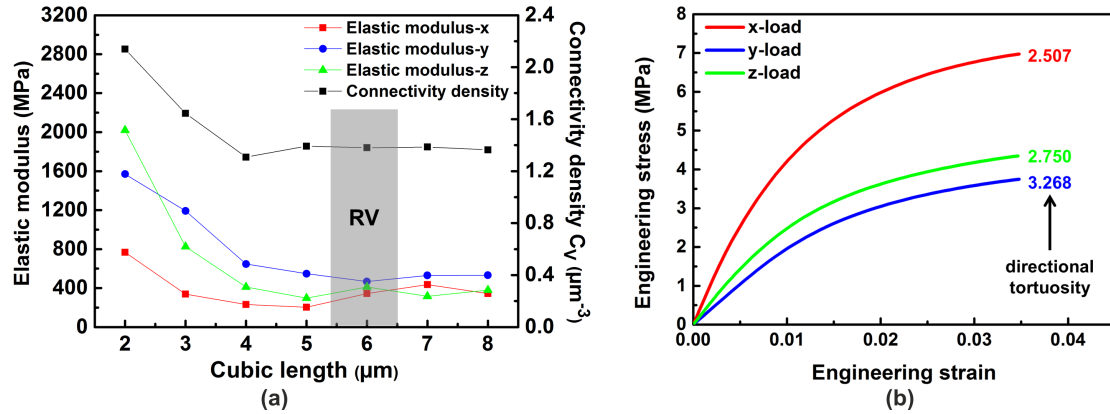


Figure 5.5: (a) Elastic moduli of the 3D reconstructions in three directions as a function of the cubic length. The cubic length of the mechanical behavior RV is around 6 μm , which is consistent with the microstructural RV size; (b) engineering stress–strain curves of a 3D reconstruction with cubic length of 5 μm uniaxially compressed in x, y and z direction: mechanical anisotropy is correlated with directional tortuosity.

The elastic moduli of the 3D reconstructions in the three directions were determined from the slope of the initial linear part of the loading segment at the strain range of 0 to 0.002 of the engineering stress–strain curves obtained from the FEM simulations. The results as a function of the cubic length are shown in Figure 5.5(a). It is found that as the cubic length increases, the elastic moduli

decrease until nearly constant levels are reached, where the cubic length is around $6 \mu\text{m}$. This size is exactly in the microstructural RV range of npg network of sample composite_400nm. One example is given in the plot for comparison. As shown in Figure 5.5(a), the connectivity density C_V values of the 7 reconstructions were plotted as a function of the cubic length. As the cubic length increases, C_V decreases until the RV size is reached. It has the same tendency as the elastic modulus. Therefore, it seems that the mechanical behavior RV of the gold phase is consistent with the microstructural RV. Finite volume effect reflected both in the microstructure and the mechanical response. Moreover, it was found that the cubic length of the mechanical behavior RV is consistent with the observation from the open- and the closed-cell foams that the modulus reaches a plateau level when the ratio of the sample size and the cell size is about 6 [153]. The cell size of npg structure can be quantified as the sum of the mean diameter of the ligaments and the pores. The mean pore diameter is about 15–25% larger than the mean ligament diameter, as quantified using the approach presented in section 4.2.2. Thus, the length of npg mechanical behavior RV should be about 12–14 times of the mean ligament diameter, which is close to the results in the present work that the mechanical behavior RV of npg network is about 15 times of the mean ligament diameter. Although the determination of the mechanical behavior RV is made by only considering the fully interconnected ligament structure, the deleted floating ligaments at the edges of the model don't play an important role since their volume fraction is less than 2% and they don't carry load within the volume investigated.

5.2.2 Mechanical anisotropy

The mechanical responses in the x, y and z directions obtained from the simulations allow to explore a possible mechanical anisotropy of the 3D reconstructions. From Figure 5.5(a), it is noticed that there are variations of the elastic modulus in the three directions, which indicates that there are mechanical anisotropy. Figure 5.5(b) shows the engineering stress-strain curves of a 3D reconstruction with a cubic length of $5 \mu\text{m}$ uniaxially compressed in x, y and z directions. The mechanical anisotropy is revealed by the non-overlapped curves. Above the RV size, these variations are significantly reduced. However, the mechanical anisotropy doesn't negate that a volume is representative of the whole structure. The relation between the mechanical anisotropy and the structural parameters of npg will be discussed in section 5.3.2.

5.2.3 Mechanical behavior of a RV

Simulation results of the gold network RV with cubic length of $6 \mu\text{m}$ of sample composite_400nm were analyzed, which are supposed to be representative of the

mechanical behavior of the corresponding npg structural geometry. Figure 5.6 shows the Von Mises stress contours of the RV, uniaxially compressed to different engineering strains. The engineering stress–strain curve is shown in Figure 5.7. Figure 5.6(a) shows the original geometry of the npg structure from one of the side surfaces of the RV. When it is compressed to 3% strain, it was observed that some of the ligaments have already been yielded (green) since the yield stress input for the simulation is 700 MPa. When it was compressed to 6% strain, some of the ligaments rotated and contacted with each other. Some of them overlapped, as illustrated in the red circle. When the strain was 15%, there were more overlapped ligaments. This was caused by the undefined contact condition of ligaments in the simulation. It can be imagined that the ligament contacts will lead to stiffening of the whole volume. Investigations on the contact problem is out of scope of the present study. Throughout the compression, it was observed that plastic deformation was located at the internal ligaments of the model mostly. The “plastic hinges” were formed at the junctions where 3–4 ligaments joined together, as shown in Figure 5.6(e), which indicates bending dominated deformation at the ligaments. Ligaments at the cut surface of the volume show low stress compared to the internal ligaments since they were less constrained and contribute little to the load transfer within the network structure. In addition, there was almost no lateral expansion which indicates that the Poisson’s ratio of the model is close to zero.

5.2.4 Mechanical behavior self–similarity of RVs

As discussed in Chapter 4, npg structures with different mean ligament diameters are both geometrically and topologically self–similar. It is expected that the structures with different mean ligament diameters are self–similar in terms of the mechanical response as well in the same FEM simulation conditions. Here, following the observation of section 5.2.1 that the mechanical behavior RV is equivalent to the microstructural RV, FEM simulations for the meshed 3D reconstruction RVs of the npg network of sample composite.50nm and composite.200nm were carried out using the same simulation conditions as that implemented for the RV of sample composite.400nm. The loads are applied in the x direction. The engineering stress–strain curves from the three simulations were compared, as shown in Figure 5.7. As can be seen, the mechanical behavior of the 3D structural geometry of npg at the early, the mid, and the last stage of coarsening investigated in this work are quite similar. The elastic modulus results taken from the unloading slope and the yield stresses identified using the usual 0.2% strain offset convention are between 400–500 MPa and 5–6 MPa, respectively, which are close to the micromechanical testing results presented previously. Since the simulations investigated here only considered structural geometry and the size dependent be-

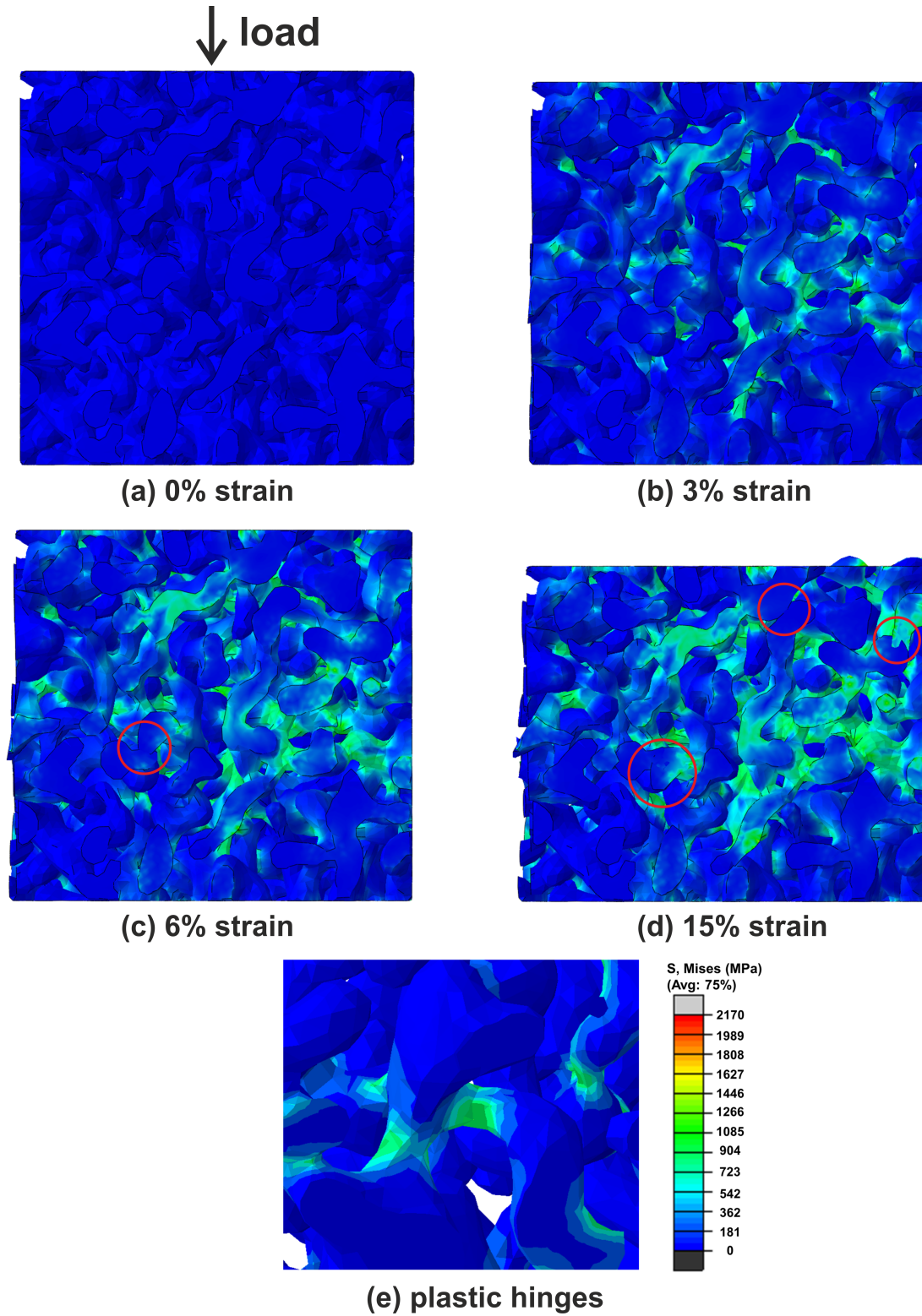


Figure 5.6: Von Mises stress contour of a RV ($6 \times 6 \times 6 \mu\text{m}^3$) uniaxially compressed to (a) 0% strain; (b) 3% strain; (c) 6% strain; (d) 15% strain; (e) plastic hinges near a triple junction. Some of the ligaments are contacted and overlapped with each other, as shown in the red circle. This was caused by the undefined contact condition of ligaments in the simulation. The “plastic hinges” formed at the junctions indicates bending dominated deformation in the ligaments.

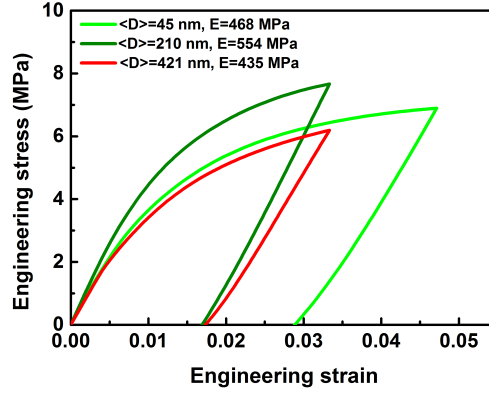


Figure 5.7: Engineering stress–strain curves obtained from FEM simulations loading in the x direction of npg 3D reconstruction RVs with mean ligament diameter of 45 nm, 210 nm and 421 nm are nearly self-similar. The elastic modulus results taken from the unloading slope are close to the experimental results presented in section 5.1.

havior which has been related to the surface stress, the dislocation nucleation and starvation mechanisms [25, 27, 46, 47] were not taken into account, the simulation results strongly support the self-similarity of npg structural geometry. Therefore, it is possible to identify structural parameters that can be used to describe the mechanical behavior of the npg structure without considering the different length scales.

5.3 Correlation between microstructure and mechanical behavior

From the nanoindentation and the *in-situ* microcompression testing, it was found that the elastic modulus of npg with mean ligament diameter of about 400 nm is ranging from 200 to 650 MPa, and the yield stress is around 8 MPa. A reasonable fit between the FEM simulations on the 3D reconstruction RV of the gold network of sample composite_400nm and the *in-situ* microcompression experiment was found, as shown in Figure 5.8(b). The yield stress input of the gold is 700 MPa and other material parameters are described in Chapter 3. The high yield stress of gold is consistent with results from micromechanical testing [17, 20, 25, 27]. The elastic modulus determined from the unloading segment of the stress–strain curve of the simulation is about 440 MPa and the yield stress is about 5 MPa. These results are comparable to the micromechanical testing results presented in this work but significantly lower than most of the experimental results reported previously, as reviewed in section 2.1.2. Additionally, the Gibson–Ashby scaling predictions are much higher, which give an elastic modulus of 8.6 GPa and

a yield stress of 39 MPa for npg with a solid relative density of 32.6%, a gold yield stress of 700 MPa and a gold elastic modulus of 81 GPa. Considering the complex microstructure of the ligament network of npg, it is important to understand why the scaling law fails to predict the mechanical behavior and what are the critical structural parameters in determining the mechanical behavior of npg.

5.3.1 Role of effective relative density

As reviewed in Chapter 2, the Gibson–Ashby scaling relations were derived based on an interconnected rectangular beam model using beam bending theory. A FEM simulation on a Gibson–Ashby model with $(3 \times 3 \times 3)$ unit cells, which is considered to be a representative volume of this structure, was compared to that on a 3D reconstruction RV of the npg network with mean ligament diameter of 421 nm using the same simulation conditions. Figure 5.8(a) shows the meshed

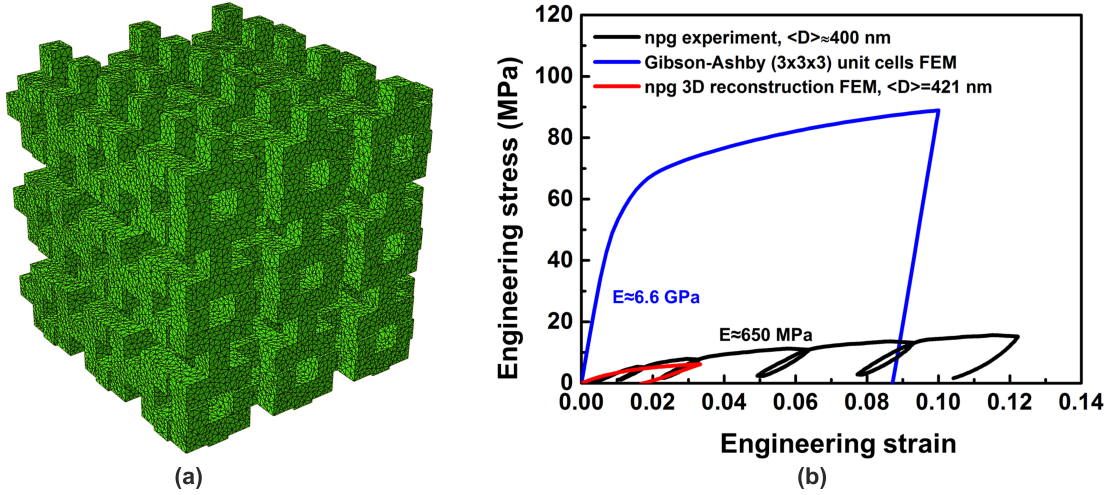


Figure 5.8: (a) A meshed $(3 \times 3 \times 3)$ unit cells of the Gibson–Ashby model structure with a solid relative density of 32.8%; (b) engineering stress–strain of the *in-situ* microcompression testing for sample npg_400nm with a solid relative density of about 30%, the simulations for the npg 3D reconstruction RV with a solid relative density of about 32.6% and the Gibson–Ashby model. The elastic moduli from the experiment and the 3D reconstruction simulation are one magnitude lower than that from the Gibson–Ashby model simulation.

Gibson–Ashby model with a solid relative density of 32.8%, which is quite close to that of the npg 3D reconstruction RV (32.6%) and the pure npg sample ($\sim 30.0\%$). The correspondent engineering stress–strain curves are shown in Figure 5.8(b). For the Gibson–Ashby model, the elastic modulus taken from the unloading segment is about 6.6 GPa and the yield stress taken from 2% strain offset is about 50 MPa. These results are strongly comparable to the Gibson–Ashby scaling predictions for npg. However, there is a difference of an order of magnitude to the npg 3D reconstruction simulations and the experimental results. In order to understand the

reason of this significant discrepancy, a direct comparison in terms of the structural geometry between the two models was made.

When the Gibson–Ashby scaling model structure is under load, all the beams which compose the network structure contribute to the load bearing. The solid relative density is the sole structural parameter needed in determining the mechanical behavior. However, from the RVs of the npg 3D reconstructions, it was found that not all the ligaments contribute to the load transfer since there are some dangling ligaments in the network. Figure 5.9(a) shows a 2D representation of the skeleton of a 3D reconstruction. The fully interconnected ring skeletons in red contribute to the load bearing instead of the black dangling branches. In the real structure shown in Figure 5.6, it was found that the stress is transferred mostly in the internal ligaments, and the stresses in the dangling ligaments, which can be directly observed near the side surface of the volume in the figures, are close to zero.

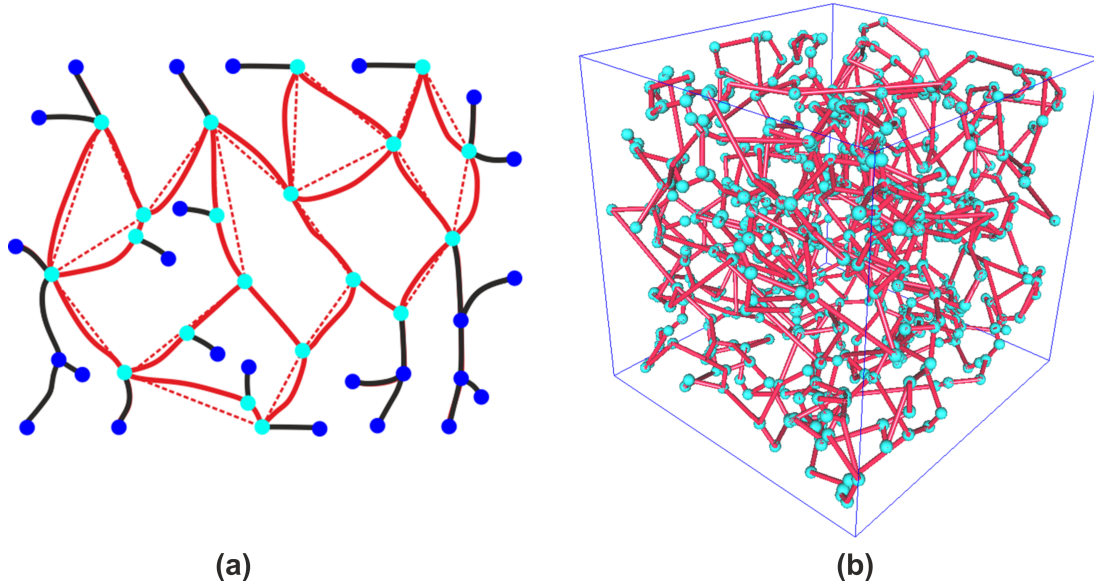


Figure 5.9: (a) A 2D schematic graph of a npg skeleton structure showing the fully interconnected load-bearing ring skeleton in red and the dangling branches in black. The nodes belonging to the ring structure are shown in cyan and belonging to the dangling ligaments in blue. The Red dashed line shows the Euclidean distance between the cyan nodes; (b) skeletonization of a 3D reconstruction RV of the npg network of sample composite_400nm, revealing a fully interconnected ring structure. The nodes are shown in cyan, and the ligaments are shown in red.

In order to quantify the volume fraction of the fully interconnected load bearing structure, which was named as effective relative density ρ_{eff} , a cylinder shape assumption for the ligaments based on the 3D skeletonization analysis of the structure was employed [148]. A Python language script was written to extract the skeleton of the ring structure and delete the dangling branches. The ring struc-

ture is taken as a set of interconnected ligaments with cylindrical shape. The cylinder diameters are the same as the mean ligament diameters quantified from the 3D reconstructions. The cylinder lengths are defined as the Euclidean distance between two nodes. The 3D skeleton of the load bearing structure of the npg 3D reconstruction RV of sample composite_400nm is shown in Figure 5.9(b). It has the same connectivity as the 3D reconstruction since it is the abstraction of the 3D structure. However, it should be noted that with this assumption, there are overlap volumes at the junctions of the ligaments, which need to be subtracted from the total volume of the ring structure.

In order to estimate the overlap volume, each ligament is considered to be a cylinder with two half spheres at the ends, as schematically illustrated in 2D in Figure 5.10(a). The sphere has the same diameter as the cylinder. The blue dashed line shows the cylinder length. Figure 5.10(b) shows that two ligaments

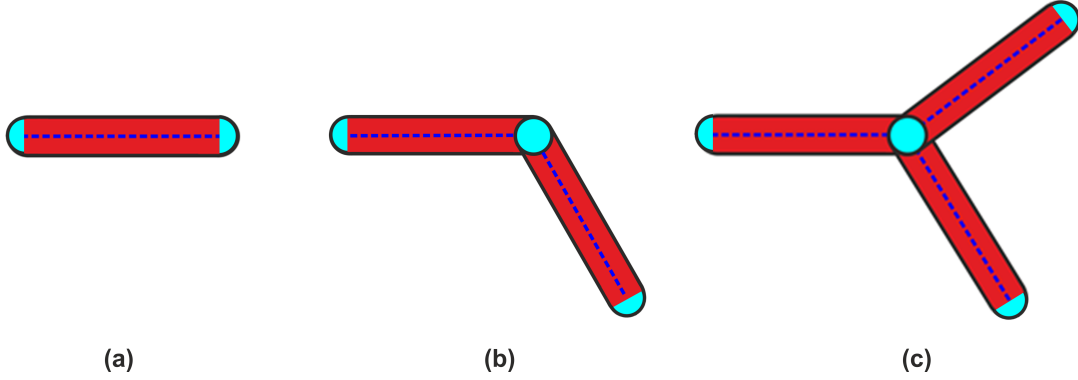


Figure 5.10: (a) The ligament is considered to be a cylinder with two half spheres at the ends. The blue dashed line shows the cylinder length; (b) two ligaments are connected by a sphere node. The overlap volume is estimated to be the volume of a sphere; (c) three ligaments join together, the overlap volume is estimated to be the volume of two spheres.

are connected by a sphere node. The overlap volume is estimated to be the volume of a sphere. When three ligaments join together, as shown in Figure 5.10(c), the overlap volume is estimated to be the volume of two spheres. With the skeletonization results, the number of ligaments which share the same nodes can be obtained. Thus, the overlap volume at the junctions of the ring structure can be obtained.

Based on the cylindrical assumption analyses, it was found that the effective relative density of the npg network structure shown in Figure 5.9(b) is about 15.0%. That means, near half of the volume composes the load bearing structure and half of it is less able to contribute to the load transfer of the entire volume. Applying this effective relative density result to the Gibson–Ashby scaling relations, it was found that the predicted elastic modulus is about 1.8 GPa and the yield stress is

about 12.2 MPa. These values are relatively close to the FEM simulations results of the npg 3D reconstruction RVs. Similar analyses were carried out for the gold network 3D reconstruction RVs of sample composite_50nm, composite_200nm, as summarized in Table 5.1. It was found that the results from the Gibson–Ashby scaling predictions are still higher than the results from the 3D reconstruction based FEM simulations. The difference might be attributed to the cylindrical geometry assumption for the ring structure when determining its effective relative density. On the one hand, the ligaments along the load transfer paths are irregular with broad diameter distributions, as shown in Figure 4.19. Deformation tends to be localized at ligaments with smaller diameter. The constant diameter of the cylindrical assumption used in the analysis might lead to big deviations of the mechanical response. On the other hand, in the cylindrical assumption, the load is transferred along the straight cylinders, which is the most efficient load transfer paths and the tortuosity equals to 1. However, this is not realistic since the ligaments in the real structure have tortuosity higher than 1. The stiffness of the npg RVs should be lower than the predictions using the effective relative density as the input, and the results should be closer to the simulations results of the 3D reconstruction RVs. Nevertheless, compared to the predictions using the solid relative density as the input, the difference is significantly reduced when using the effective relative density as the input. This indicates that when using the Gibson–Ashby scaling relations to predict the mechanical behavior of the npg structure, the effective relative density should be applied instead of the solid relative density.

5.3.2 Role of directional tortuosity

It was found that a correlation between directional tortuosity τ_D and mechanical anisotropy of the 3D reconstructions may exist. The directional tortuosity analysis discussed in Chapter 4 reveals that the 3D reconstructions exhibit microstructure anisotropy, as shown in Figure 4.21(b). As can be seen from Figure 5.5(b), τ_D results in each direction are shown with the same color as the stress–strain curve in correspondent direction. It was observed that smaller τ_D correlates with a higher elastic modulus. This is quite reasonable since smaller τ_D simply means the effective load transfer path in the loading direction is shorter, which makes the material stiffer compared to the path with higher τ_D . However, it should be noticed that this conclusion is based on the assumption that the ligament diameter along the load transfer paths are constant. As discussed in Chapter 4, ligaments have irregular shape with broad diameter distribution. Deformation tends to be localized at ligaments with smaller diameter. Thus, τ_D alone is not enough to explain the mechanical anisotropy. Further study on the ligament diameter distribution along the shortest path is necessary.

5.4 Conclusions

The main objective of this chapter was to understand the influence of the ligament network structure on the mechanical response of npg through coupling micromechanical experiments on sample npg_400nm and FEM simulations on the 3D meshed reconstructions of the npg network RV of sample composite_400nm. The key findings can be summarized as follows:

- The mechanical behavior of the 3D reconstructions exhibited a finite volume effect with the RV sizes similar to the microstructural RV sizes. The RVs showed mechanical anisotropy which was found to be correlated with the directional tortuosity. Plastic deformation of the RV was located at the internal ligament structure of the model mostly. Bending dominated deformation was located at junctions which connected 3–4 ligaments and the “plastic hinges” were formed. Little lateral expansion was found which indicates that the Poisson’s ratio of npg is close to zero. This supports the *in-situ* microcompression and nanoindentation testing results. By comparing the FEM simulations for the 3D reconstructions with different mean ligament diameters, it was found that the npg structure is self-similar in terms of the mechanical response.
- A reasonable fit between the simulations and the experimental stress–strain curves was achieved. It was found that the elastic modulus and the yield stress of npg and its 3D reconstructions are more than one order of magnitude lower than predicted by the Gibson–Ashby scaling model and most of the results reported in the literatures.
- A correlation between microstructure and mechanical behavior of npg structure was investigated to explain the significant discrepancy. The effective relative density of the load bearing ring structure was found to be the critical parameter that determine the mechanical behavior of npg, instead of the solid relative density of the entire volume.

Table 5.1: Ligament relative density (ρ_{np}/ρ_s), effective relative density (ρ_{eff}), elastic modulus (E_{GA}), yield stress (σ_{GA}) from Gibson–Ashby scaling predictions using effective relative density as the input structural parameter, and elastic modulus (E_{np}), yield stress (σ_{np}) from FEM simulations of npg network structures with different mean ligament diameters, and the Gibson–Ashby model.

3D model	ρ_{np}/ρ_s	ρ_{eff}	E_{GA} (GPa)	E_{np} (GPa)	σ_{GA} (MPa)	σ_{np} (MPa)
npg network, $\langle D \rangle = 45$ nm	$(30.4 \pm 0.4)\%$	$\sim 17.4\%$	~ 2.5	0.5	~ 15.2	~ 5
npg network, $\langle D \rangle = 210$ nm	$(34.0 \pm 0.6)\%$	$\sim 14.6\%$	~ 1.7	0.6	~ 11.7	~ 6
npg network, $\langle D \rangle = 421$ nm	$(33.4 \pm 0.3)\%$	$\sim 15.0\%$	~ 1.8	0.4	~ 12.2	~ 5
Gibson–Ashby model	32.8%	32.8%	~ 8.7	~ 6.6	~ 39.4	~ 50

6. Mechanical behavior of Npg–Epoxy Composites

Having investigated the influences of the structural geometry on the mechanical behavior of npg, the next objective is to explore the influences of the infiltrated epoxy phase, which up until now has been explicitly ignored. As introduced in Chapter 2, npg shows considerable compressive ductility but brittle failure under tension. After infiltration with epoxy, the resultant npg–epoxy composite exhibits tensile ductility and ligament length scale dependent effect on the strength [42]. Figure 6.1 shows a 2D structural representation of npg–epoxy composites. The gold and epoxy phases, along with the interface between them are shown in different colors. In order to understand the influences of the epoxy phase on the mechanical behavior and the mechanisms of deformation and failure, nanoindentation based micromechanical testing, 3D microstructural characterization and FEM simulations were carried out for npg–epoxy composites.

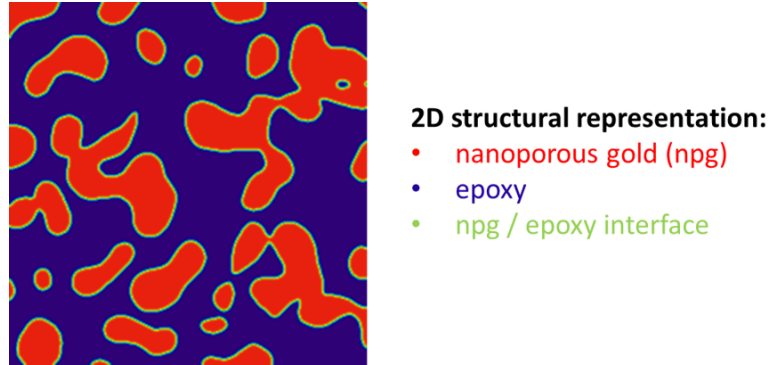


Figure 6.1: 2D structural representation of npg–epoxy composites shows npg, epoxy and interface between them.

6.1 Micromechanical characterization

6.1.1 Nanoindentation

Hardness and elastic modulus

The hardness and elastic modulus of the npg–epoxy composites were measured by nanoindentation testing. Figure 6.2(a) shows six Berkovich indentations on a

well prepared surface of sample composite_200nm. Figure 6.2(b) shows an enlarged view of one of the indents. A thin Pt layer deposited on the indentation allows to make a clear FIB cross section cut for the indent, as shown in Figure 6.2(c). The solid and dashed lines in green illustrate the indent morphology. The composites microstructure under the indenter seems to be not densified. The ligament area fraction of the region surrounded by the red dashed lines on the cross section was measured. The area of this region is big enough to represent the microstructure of the cross section. The difference of the ligament area fraction in this region and that in an undeformed region with the same area was found to be less than 1%. This is not surprising since unlike pure npg, the densification of npg-epoxy composites is significantly suppressed because of the epoxy infiltration.

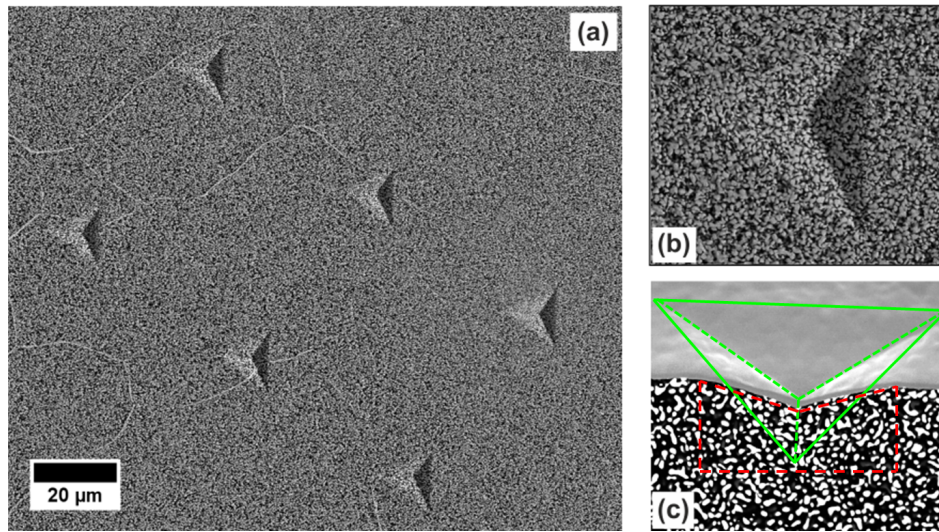


Figure 6.2: SEM images of Berkovich indentations on sample composite_200nm: (a) 6 indentations on the surface; (b) an enlarged view of the indent; (c) FIB milled cross section view of the indent. The solid and dashed lines in green illustrate the indent morphology. The difference of the ligament area fraction of the region surrounded by the red dashed lines and that in an undeformed region with the same area was found to be less than 1%, which indicates that the densification of npg-epoxy composite is significantly suppressed.

Load-displacement curves of the five composite samples together with one epoxy sample are shown in Figure 6.3. Generally, the measurements are quite reproducible for each sample. Figure 6.4 shows an example of the elastic modulus and hardness as a function of displacement into the surface for sample composite_400nm from 16 nanoindentation tests, as achieved with CSM. As can be seen, the modulus and hardness values have large variations when the displacements are less than 300 nm. Some of the curves show an exponential decay in modulus and hardness as a function of displacement until a plateau appears, whereas other curves show modulus and hardness values decreasing to a low value rapidly at

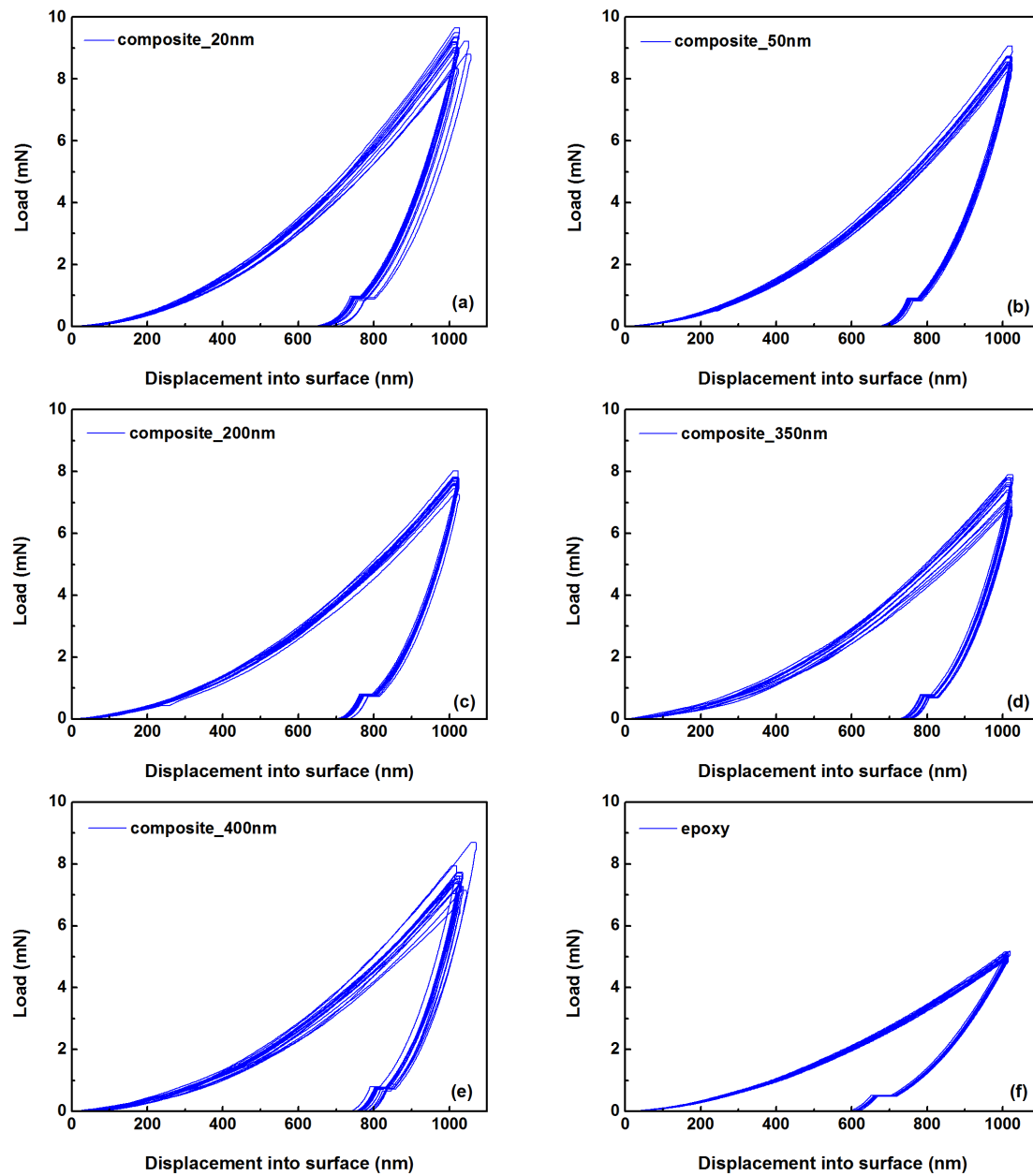


Figure 6.3: Load–displacement curves from 16 nanoindentation tests of (a) sample composite_20nm; (b) sample composite_50nm; (c) sample composite_200nm; (d) sample composite_350nm; (e) sample composite_400nm; (f) epoxy sample.

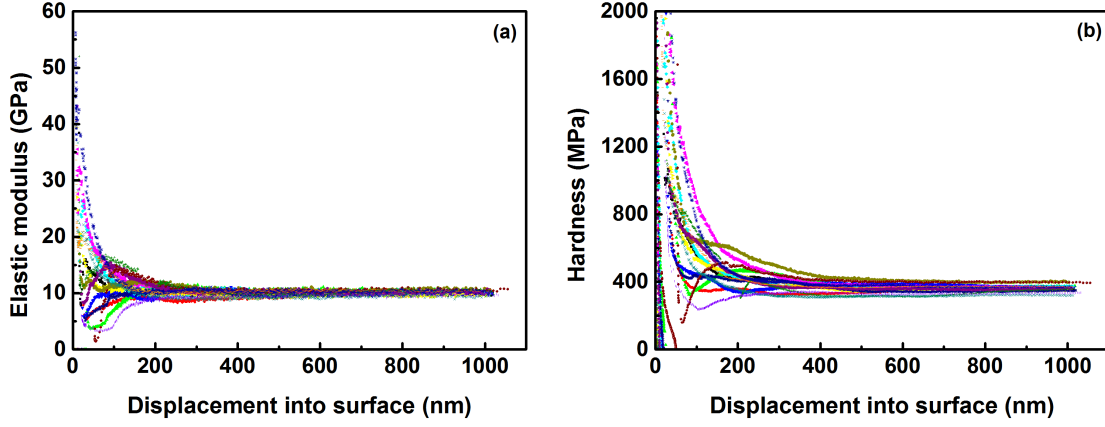


Figure 6.4: (a) Elastic modulus and (b) hardness from continuous stiffness measurement (CSM) as a function of displacement into the surface for sample composite_400nm from 16 nanoindentation tests.

first, then increase to reach the plateau.

The large variations at small depths could be understood in a few possible aspects: surface roughness, mechanical damage from surface preparation, and microstructure length scale.

- (1) The sample surface might be rough at the scale of the indenter contact dimension, which may lead to significant errors in the determination of contact area. Accurate and meaningful measurements can be made only when the indentation depth is large compared to the surface roughness [154];
- (2) There might be work hardened layers at the mechanically polished surface which lead to a increase in hardness at small depth [154];
- (3) The Berkovich tip typically has a radius of curvature on the order of 50–100 nm, which is close to the ligament diameters. At the beginning of loading, the tip might indent into a single ligament, which gives a high hardness and modulus value. It might also indent into the epoxy phase or the boundary of gold and epoxy, which is much softer than the individual ligament. As the displacement increases, the indentation volume increases with more ligaments and epoxies touching the indenter, and the modulus and hardness are approaching the inherent value of the composites until a plateau appears.

Therefore, the modulus and hardness results of each test were taken from the plateau regions. The results are summarized in Table 6.1 and Figure 6.5. It was found that all the five npg-epoxy composite samples show a similar elastic modulus of around 10 GPa, whereas the hardness values show an intrinsic size effect, i.e., the hardness decreases as the mean ligament diameter increases.

Table 6.1: The hardness and elastic modulus results of the five npg-epoxy composite samples and one epoxy sample.

Sample	Hardness (MPa)	Elastic modulus (GPa)
composite_20nm	489 ± 32	10.2 ± 0.4
composite_50nm	468 ± 21	9.9 ± 0.2
composite_200nm	405 ± 18	9.7 ± 0.2
composite_350nm	381 ± 27	10.0 ± 0.4
composite_400nm	361 ± 16	10.0 ± 0.3
epoxy	291 ± 12	4.7 ± 0.1

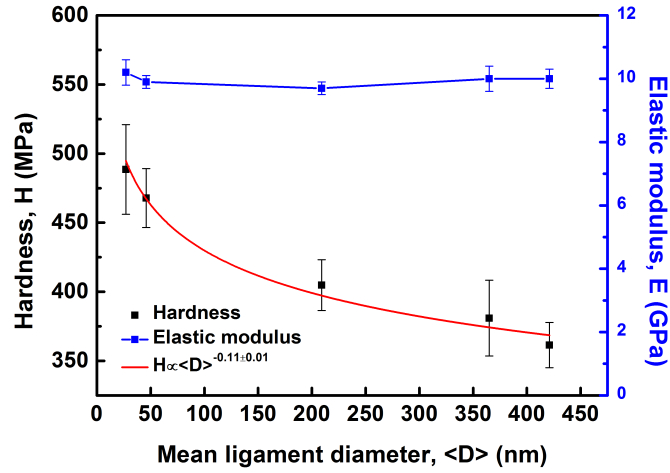


Figure 6.5: Summary of the hardness and elastic modulus results: elastic modulus values of the five npg-epoxy composite samples are all around 10 GPa; the hardness shows an intrinsic size effect: the hardness decreases as the mean ligament diameter increases. This size effect can be described by a power law relation: $H \propto \langle D \rangle^{-0.11 \pm 0.01}$.

Effect of strain rate

The hardness and elastic modulus results at different strain rates were summarized in Figure 6.6. As can be seen from Figure 6.6(a), as the strain rate $\dot{\epsilon}$ increases, the hardness increases as well, whereas the elastic modulus remains at around 10 GPa. Figure 6.6(b) shows the log-log plot of the hardness versus the strain rate. The linear fit to these data gives a strain-rate sensitivity of $m=0.056$, which indicates that the npg-epoxy composite is not strongly strain rate sensitive.

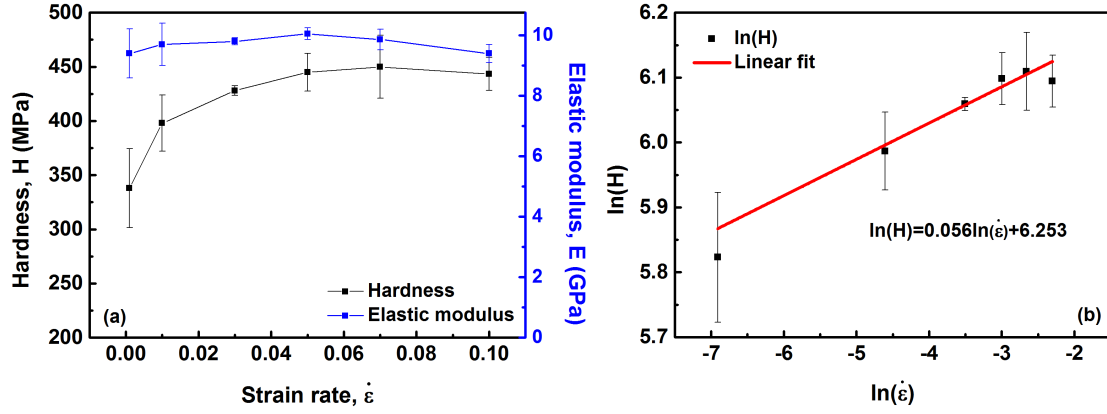


Figure 6.6: (a) The hardness and elastic modulus as a function of strain rates from 0.001/s to 0.1/s for sample composite_200nm; (b) the log-log plot of the hardness versus the strain rate. The linear fit to these data gives a strain-rate sensitivity of $m=0.056$.

6.1.2 Microcompression

Yield stress and elastic modulus

The yield stress and elastic modulus of the npg-epoxy composites with varying mean ligament diameters were determined by microcompression testing. Figure 6.7 and Figure 6.8 show the SEM images of microcolumns of sample composite_200nm with diameters of 2 μm , 3 μm , 5 μm , 8 μm , 10 μm and 12 μm before and after microcompression. The microcolumns have well controlled cylindrical shapes with a height/diameter ratio of about 3. Very limited redeposition on the column surface was observed. Gold and epoxy phases are very easy to be recognized. A circular fiducial marker was fabricated on a thin layer of Pt on top of some of the microcolumns for a better position recognition by the lathe milling script. The Pt layer has a thickness of about 100 nm, which has a negligible influence on the mechanical behavior of the entire microcolumn. After microcompression, some of the microcolumns are collapsed, which could be attributed to the misalignment between the flat punch indenter and the microcolumns. The rest show a double barrel deformation, which seem to be localized at the top and the bottom. This

can be clearly observed from the 12 μm diameter microcolumn after deformation shown in Figure 6.8(f).

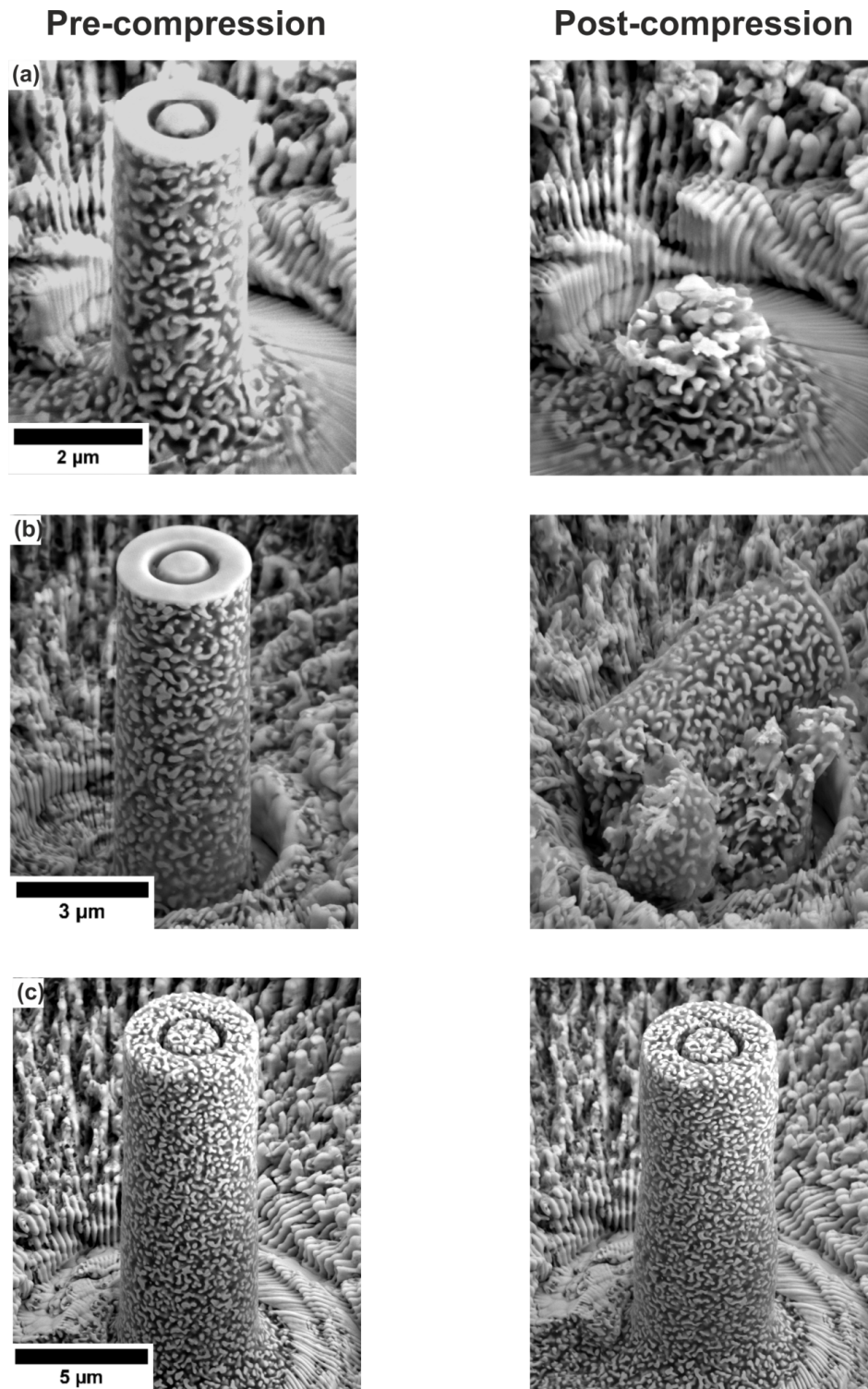


Figure 6.7: SEM images of lathe milled microcolumns with different diameters (D_0) of sample composite_200nm before compression (left column) and after compression (right column): (a) $D_0=2\ \mu\text{m}$, (b) $D_0=3\ \mu\text{m}$, (c) $D_0=5\ \mu\text{m}$.

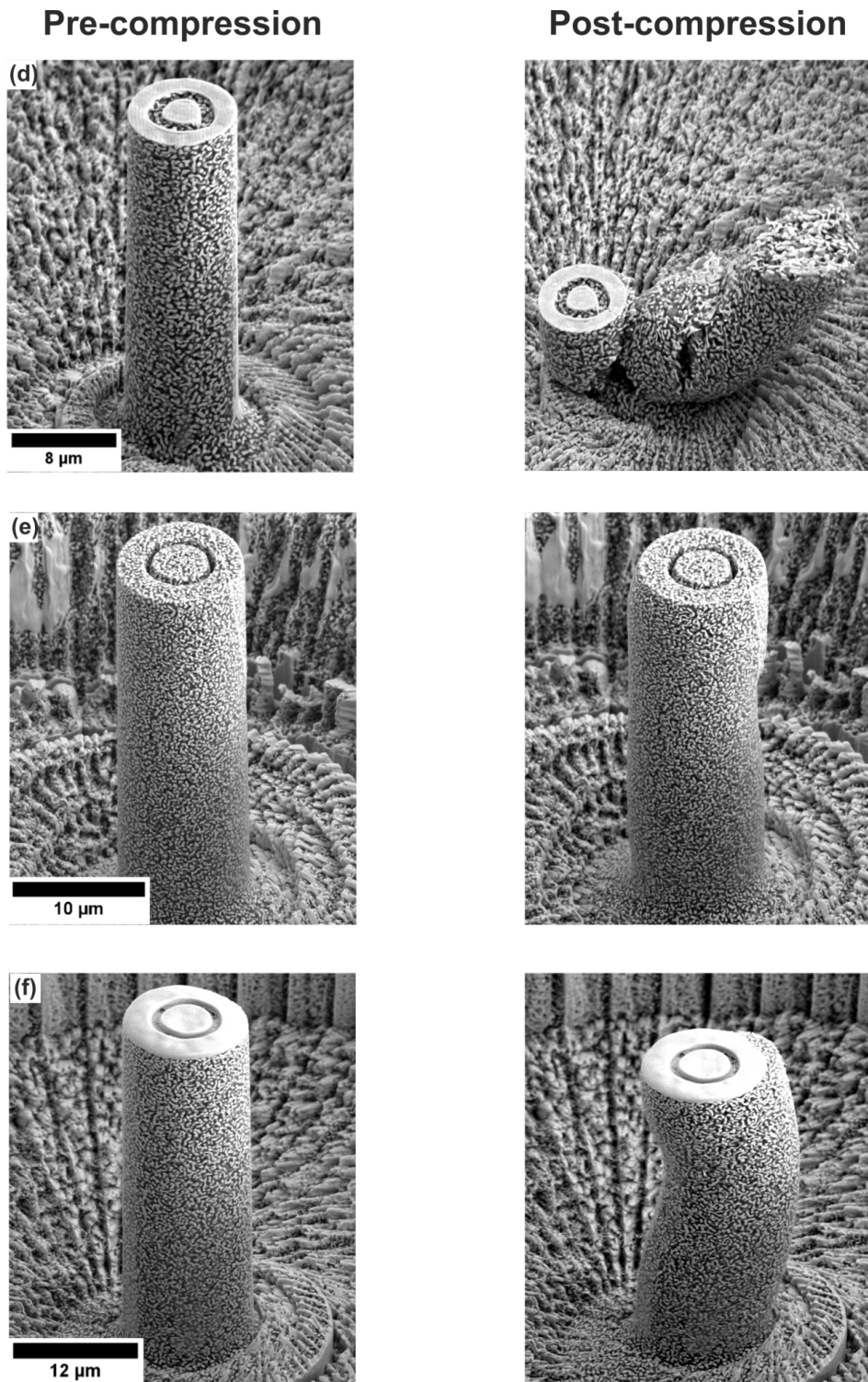


Figure 6.8: SEM images of lathe milled microcolumns with different diameters (D_0) of sample composite_200nm before compression (left column) and after compression (right column): (d) $D_0=8\ \mu\text{m}$, (e) $D_0=10\ \mu\text{m}$, (f) $D_0=12\ \mu\text{m}$.

Representative stress–strain curves of the microcompression testing for the sample composite.200nm are shown in Figure 6.9(a) with different colors denoting different microcolumn diameters. They are quite reproducible for microcolumns with same diameters. The transition from elastic to plastic deformation is quite smooth without apparent yield point, followed by a near constant plastic flow. The yield stress and elastic modulus determined using the approach introduced in Chapter 3 are plotted in Figure 6.9(b). A significant dependence of the yield stress on the microcolumn dimension, i.e., extrinsic size effect is observed. Similar observations were reported for single crystalline materials [14, 17, 21]. It is different from pure npg whose mechanical behavior is controlled by the ligament size (intrinsic size effect) but not by the microcolumn dimension [26]. The average yield stress of the microcolumn is about 157 MPa when the diameter is beyond 8 μm where a yield stress plateau begins.

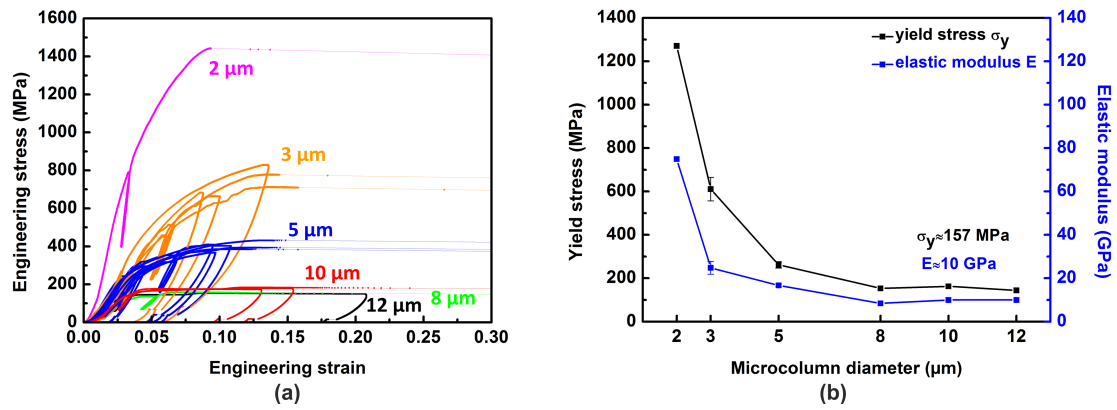


Figure 6.9: (a) Stress–strain curves of microcolumns with diameters from 2 μm to 12 μm of sample composite.200nm; (b) yield stress and elastic modulus as a function of microcolumn diameters for sample composite.200nm show significant extrinsic size effect.

It is surprising that the elastic modulus determined from CSM also shows an extrinsic size effect, which could be attributed to the FIB damage on the composite materials during the microcolumn fabrication. As already stated, Ga^+ damage during FIB milling needs to be considered or can be ignored, depending on the material and the tested volume. It was reported that Ga^+ beam milling of epoxy results in stiff surface wrinkles whose thickness is size independent when the same ion beam density is used [93, 155]. A microcompression study on a Bisphenol epoxy resin sample shows that this stiff surface skin leads to size effects in the elastic modulus, where the modulus increases with decreasing microcolumn diameter, as observed here. As the microcolumn diameter increases, the volume fraction of the stiff surface skin decreases relative to the volume of the microcolumns. Thus, the influence of the surface stiffening effect on the elastic modulus of the microcolumns decreases until the microcolumn is big enough such that the stiffening effect can

be ignored. It can be seen from Figure 6.9(b), once the microcolumn diameter increases beyond $8\text{ }\mu\text{m}$, the elastic modulus levels off to an average value of around 10 GPa, which is consistent with the results from nanoindentation testing. As for the yield stress, it was reported that only when the epoxy microcolumn diameter is at the submicron scale, there is strong size effect even if the surface stiffening effect is excluded [155]. For the epoxy microcolumns with diameters above $1\text{ }\mu\text{m}$, the yield stress is size independent. It should be noted that all the microcolumns that have been subsequently analyzed are at the micron scale with a volume bigger than the RVs determined from the microstructural analyses and the FEM simulations. The reason for the extrinsic size effect in the yield stress of the composites could be the surface stiffening effect due to the ion beam damage. It is not clear how the dislocation activities influence the extrinsic size effect.

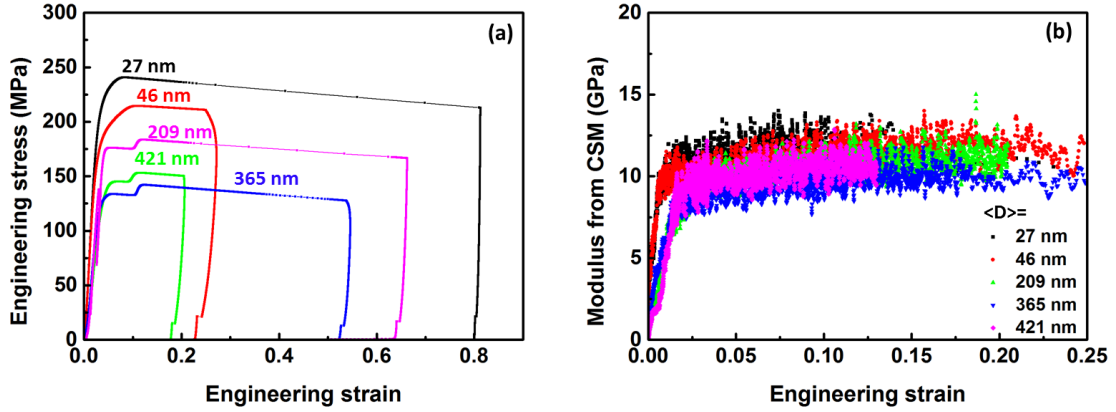


Figure 6.10: (a) Stress-strain curves and (b) elastic modulus from CSM of microcolumns with a diameter of $10\text{ }\mu\text{m}$ of npg-epoxy composite samples with different mean ligament diameters $\langle D \rangle$. A strong size dependence of the yield stress with respect to the ligament diameters can be observed and the elastic modulus of all samples is around 10 GPa.

Since the elastic modulus is size independent, it can be used as a validation of the ion beam damage and the stress-strain analysis. Since the microcompression testing on the microcolumns with diameters beyond $8\text{ }\mu\text{m}$ give elastic moduli close to the nanoindentation results, the mechanical behavior of the npg-epoxy composites were assessed using microcolumns with diameters larger than $8\text{ }\mu\text{m}$ in this work. Microcolumns with diameters of $10\text{ }\mu\text{m}$ were chosen for the testing for all the samples. The stress-strain curves and the elastic modulus from CSM of samples with different mean ligament diameters are shown in Figure 6.10. The yield stress and the elastic modulus of the five npg-epoxy composite samples were summarized in Table 6.2 and Figure 6.11. A strong size dependence of the yield stress with respect to the ligament diameters can be observed and the elastic modulus of all samples is around 10 GPa. Compare the microcompression with the nanoindentation testing results, it was found that the ratios of hardness to

yield stress are between 2 and 3, as shown in Figure 6.11. These ratios are consistent with that of full dense material, which confirms that the densification of npg–epoxy composites is significantly suppressed by the infiltrated epoxy phase.

Table 6.2: The yield stress and the elastic modulus results of the five npg–epoxy composite samples from microcompression testing.

Sample	Yield stress (MPa)	Elastic modulus (GPa)
composite_20nm	~218	~10
composite_50nm	~182	~10
composite_200nm	~157	~10
composite_350nm	~126	~10
composite_400nm	~140	~10

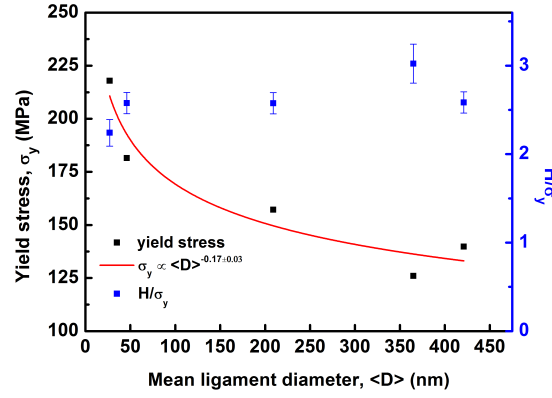


Figure 6.11: Yield stress of microcolumns with diameter of $10\ \mu\text{m}$ for npg–epoxy composites with different mean ligament diameters $\langle D \rangle$. The relationship of yield stress and mean ligament diameters can be described as $\sigma_y \propto \langle D \rangle^{-0.17 \pm 0.03}$. The ratios of hardness H to yield stress σ_y are between 2 and 3.

Failure behavior

The failure behavior of npg–epoxy composites with a mean ligament diameter of 421 nm under microcompression was analyzed by 3D microstructural characterization. Figure 6.12 shows a microcolumn with a diameter of $10\ \mu\text{m}$ before and after microcompression testing. The stress–strain curve is shown in Figure 6.10(a). As can be seen in Figure 6.12(b), lateral expansions are localized at the top and the bottom of the microcolumn after compressing to a maximum of about 17% engineering strain. This is consistent with a double barrel deformation for well aligned compression testing, due to high friction between the indenter and the sample, and the inherent constraint at the substrate.

In order to understand how the microstructure changes after deformation, FIB–SEM tomography was carried out for the deformed microcolumn. A side view of

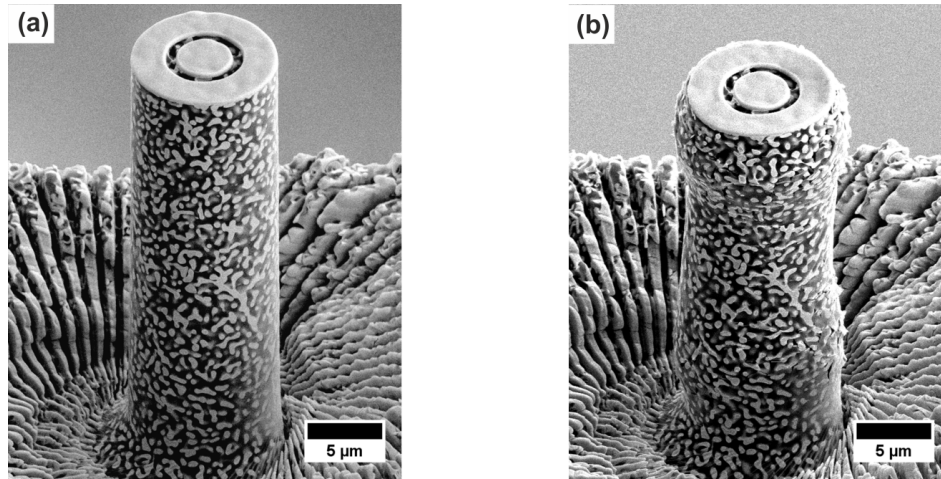


Figure 6.12: A microcolumn with a diameter of $10\ \mu\text{m}$ of sample composite_400nm: (a) before compression and (b) after compression. Lateral expansions are localized at the top and the bottom of the microcolumn.

the 3D reconstruction is shown in Figure 6.13. The differences of the microstructure between the strongly deformed and the slightly deformed regions were assessed by inspecting the 2D slices of the reconstruction. The right side of Figure 6.13 shows the 2D slices from different regions of the microcolumn. The slice with the red frame was taken from a strongly deformed region and the enlarged view shows delaminations at the gold and epoxy interface. The slice with the blue frame taken

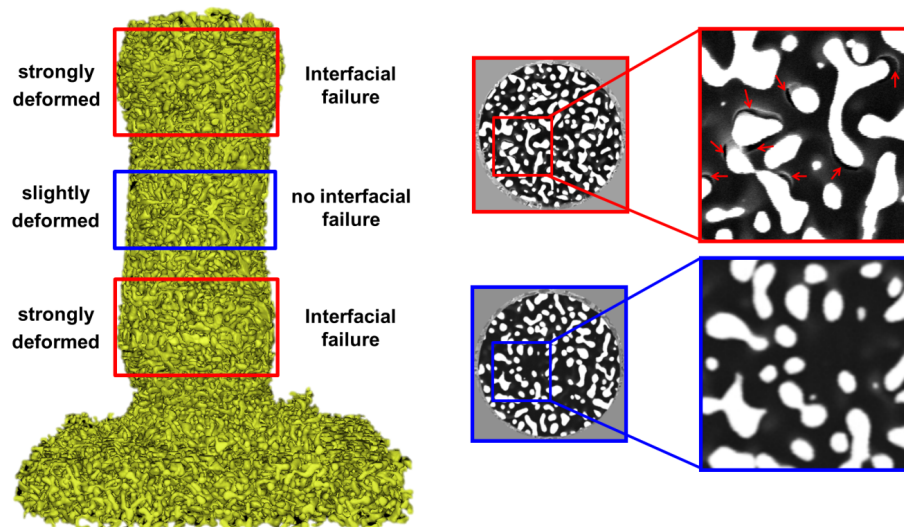


Figure 6.13: 3D FIB-SEM reconstruction of the deformed microcolumn. Yellow is the ligaments and the epoxy is transparent. 2D slices of the reconstruction show interfacial failure between gold (bright regions) and epoxy (dark regions) in the strongly deformed regions and no failure in the slightly deformed regions. No cracks either in the gold and the epoxy phases could be found. The red arrows show the locations of the interfacial failure.

from a slightly deformed region doesn't show any failures. No cracks either in the gold or the epoxy phases could be found.

The interfacial failure was analyzed from the 3D reconstruction, as shown in Figure 6.14. Figure 6.14(a) is the 3D reconstruction of a strongly deformed region

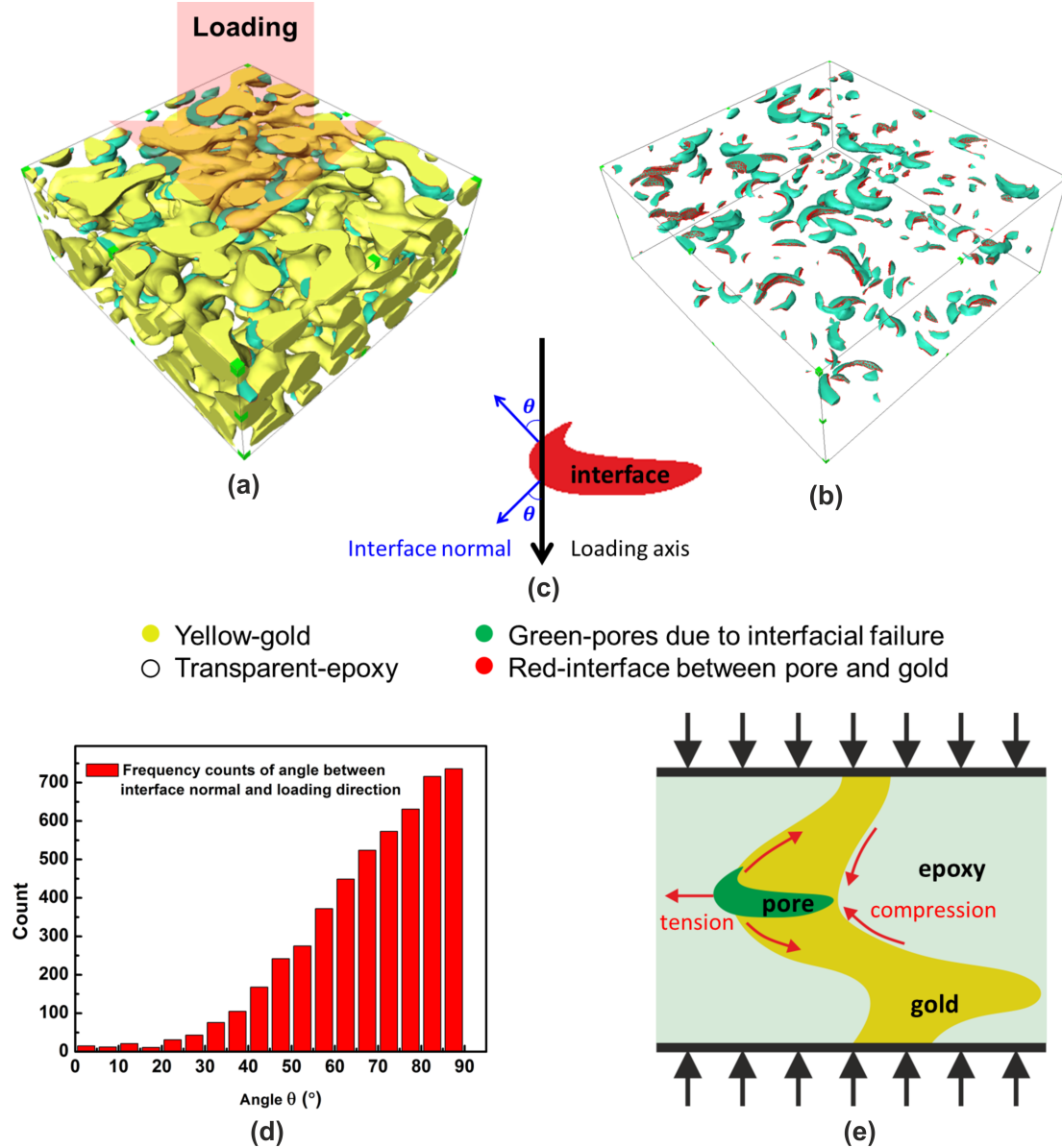


Figure 6.14: (a) 3D reconstruction of a strongly deformed region of the microcolumn: yellow–gold; green–pores due to interfacial failure. The epoxy is transparent. The load is perpendicular to the upper surface of the reconstruction; (b) pores are shown in green and gold/pore interfaces are shown in red, which have an in-plane “horse-shoe” shape; (c) a schematic illustration of the angles between the interface normals (blue arrows) and the loading axis (black arrow); (d) the frequency counts of angles between the gold/pore interface normals and the loading axis; (e) global compression of the composite and local tension in the ligament and epoxy leads to interfacial failure.

of the microcolumn. The gold ligaments are shown in yellow and the pores due to the interfacial failure are shown in green. The epoxy is transparent. The load is perpendicular to the upper surface of the reconstruction. Figure 6.14(b) shows the gold/pore interface in red. The pores are separately distributed without any connections with an in-plane “horse-shoe” shape. It is observed that most of the locations where interfacial failure happens are highly curved. The angles between the interface normals and the loading axis are calculated. As schematically illustrated in Figure 6.14(c), the angles between the interface normals and the loading axis are θ . A distribution of the angles between all the interface normals and the loading axis is shown in Figure 6.14(d). It was found that more than 90% of the angles are between 45° and 90° , and 90° appears most frequently. These information indicates that the failure is attributed to the lateral expansion of the material. The local stress state of the composites under compression is illustrated schematically in Figure 6.14(e). Under uniaxial compression, the yellow ligament is under tension on the left side and compression on the right side. The epoxy near the left side of the ligament is actually under tension, which leads to the delaminations between the gold and the epoxy phases.

6.1.3 Microbeam bending

In-situ microbeam bending

In-situ microbeam bending experiments were carried out for the sample composite_400nm, using microbeams with triangular in-plane geometry. A SEM image of the side view of such a microbeam is shown in Figure 6.15(a). A cube corner indenter tip starts touching the top surface of the beam. The distance between the position of the indent and the support is L . The thickness of the beam t is about 11 times of the mean ligament diameter, i.e., the volume investigated is representative of the global microstructure of the material. The gold ligaments microstructure was used as a speckle pattern for applying the digital image correlation. Figure 6.15(b) is a tilted view of the microbeam, from which the in-plane triangular geometry and the rectangular pad at the end can be seen. The width at the support of the beam is b_0 .

Figure 6.15(c) shows the load-displacement curve of the experiment. The beam was deflected until it broke, which happened when the displacement was about 6000 nm. As introduced in Chapter 3, a critical issue during the microbeam bending is that the sharp indenter tip makes an impression on the surface of the beam as the beam is deflected. The contribution of the indenter depth to the total displacement needs to be accounted for. For a given load, the indentation displacement into the microbeam is assumed to be the same as the displacement in the bulk material. A calibration indentation was made near the support. However, this calibration is only valid for the loading segment. The determination

of the microbeam displacement during the unloading and reloading segments are more complicated since there is partial elastic/plastic recovery of the indent [105]. This reverse mechanical behavior can be seen from the unloading–reloading segments of the load–displacement curve. Furthermore, the compliance of the support also contributes additional displacements to the beam which needs to be taken into account [110]. Figure 6.15(c) shows that at the maximum load, the indenter displacement in the bulk material is about 180 nm. Compared to the maximum displacement of the bending (~ 6000 nm), the contribution of the indentation depth is relatively small. In this study, as the digital image correlation was applied to the side surface, which provides full-field displacement measurement for the beam bending, the indentation displacement becomes less important and it was not subtracted from the data.

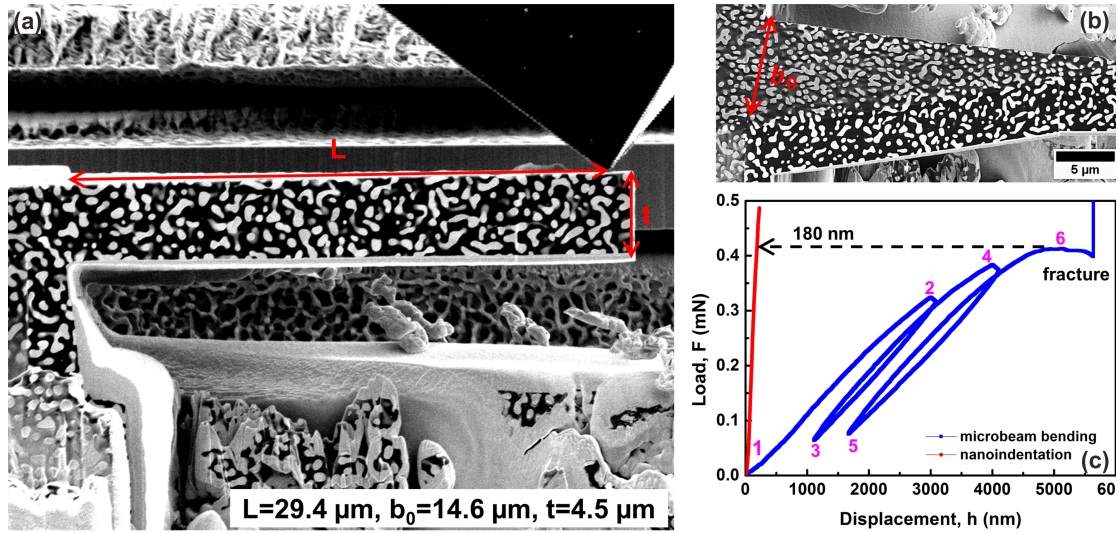


Figure 6.15: (a) Side view of the microbeam with thickness t . L is the distance of the position of the indent to the support. A cube corner indenter tip starts touching the end of the beam; (b) tilted view of the microbeam. b_0 is the width at the support; (c) load–displacement curve of the bending experiment. The microbeam was deflected to about 6000 nm when it broke. The calibration indentation displacement in the bulk material at the maximum load of the beam bending is about 180 nm, which is relatively small compared to the maximum displacement of the beam. The numbers beside the curve denote different states of the bending experiment.

Digital image correlation

A DIC subset radius of 28 pixels and subset spacing of 2 pixels were used in the DIC analysis for the region of interest on the SEM images of the microbeam side surface. Figure 6.16(a) shows one of the subsets covered on a SEM image. The special features of the ligaments were used to match the subsets on the images before and after deformation. The local displacement of the white dots were mea-

sured. Since there were large deformations during bending, the Eulerian–Almansi strain was used for the analysis. Figure 6.16(b) shows the displacement map (v) in the loading direction and Figure 6.16(c) shows the longitudinal strain map (ε_{xx}) of the microbeam after 10 minutes of imaging, which is approximately the same time spent in the bending experiment. It was found that the displacement field was ranging from -2 to 16 nm and the strain field was between -0.3% to 0.3% ,

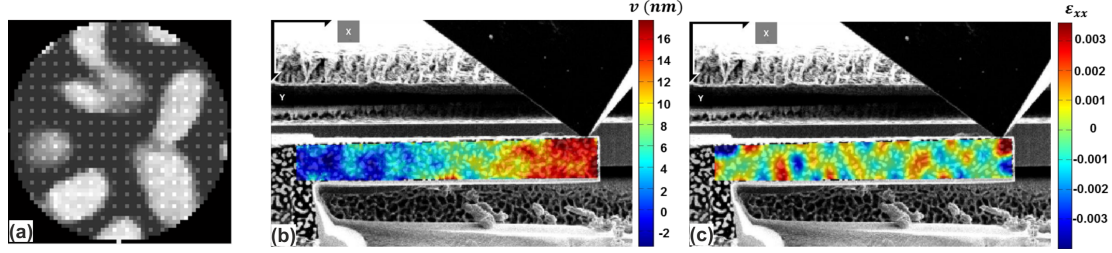


Figure 6.16: (a) A DIC subset with a radius of 28 pixels and a spacing of 2 pixels is covered on the SEM image. After 10 minutes of imaging: (b) the displacement field v in the loading direction is between -2 and 16 nm; (c) the longitudinal strain field ε_{xx} is between -0.3% and 0.3% . The error contributions are small compared to the total displacement and the applied deformation of the microbeam.

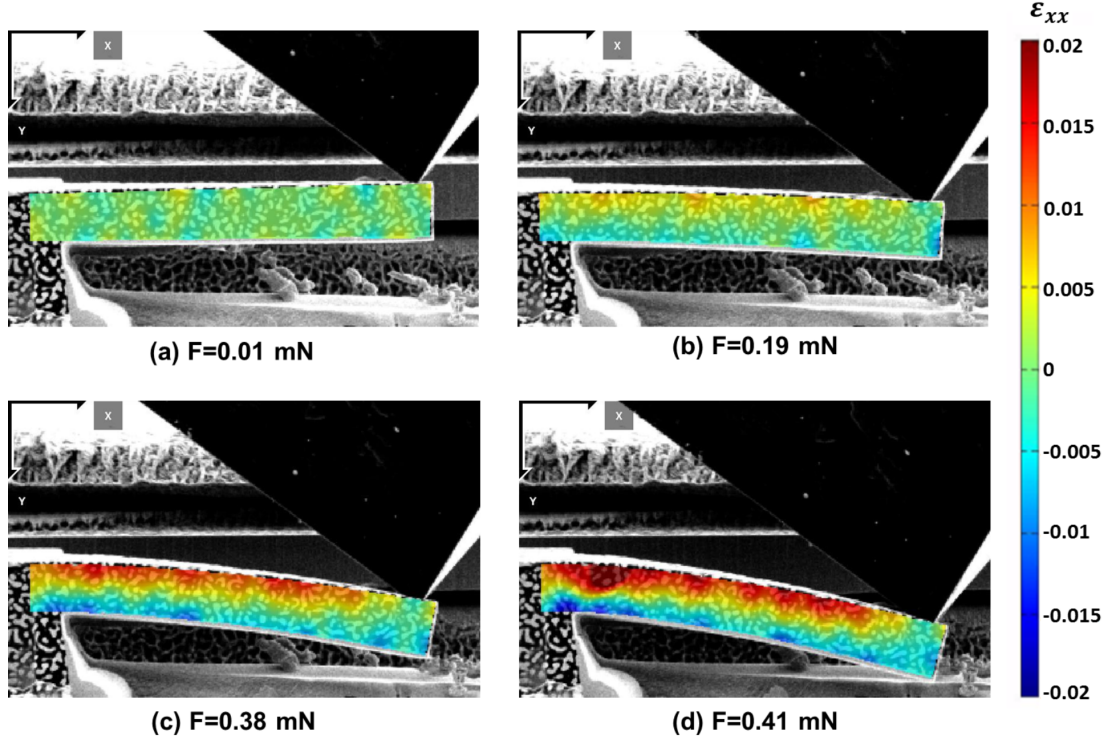


Figure 6.17: Longitudinal strain map of the microbeam at four states during the experiment: (a) the indenter tip starts touching the beam; (b) the boundary between tensile and compressive strain becomes visible; (c) at the second hold segment; (d) just before fracture.

which is quite small compared to the total displacement and the applied deformation of the beam bending experiment. Thus, the measurement error is considered negligible in this study.

The DIC measurement was applied to the images acquired from the *in-situ* experiment. Longitudinal strain maps of the microbeam side surface during the experiment were obtained. Figure 6.17 shows snapshots of the strain field of four experimental states: (a) the indenter tip starts touching the beam; (b) the boundary between tensile and compressive strain becomes visible; (c) at the second hold segment; (d) just before fracture. As can be seen, at small loads, there are strain noises on the map. As the load increases, the constant tensile strain on the top, constant compressive strain on the bottom and the neutral axis between them become more apparent. The neutral axis is not a straight line and there are strain concentrations either on the tension side or on the compression side. When the maximum load was reached, the microbeam was about to break. Figure 6.17(d) shows that near the support the strain is at the maximum level, where exactly the fracture is going to happen.

Neutral axis movement analysis

As introduced in Chapter 3, a microbeam bending experiment using a triangular in-plane geometry enables to evaluate tension-compression asymmetry of the beam by analyzing the neutral axis movement, which can be achieved by DIC measurement. The longitudinal strain at different states and different locations on the side surface of the microbeam during the experiment were measured by DIC.

Six states of the experiment illustrated in Figure 6.15(c) are analyzed: 1—the indenter tip starts touching the beam; 2—at the first hold segment; 3—at the end of the first unloading; 4—at the second hold segment; 5—at the end of the second unloading; 6—just before the fracture. For each of these experimental states, three locations on the beam were focused on, as shown in Figure 6.18: location A (near the support), location B (in the centre of the beam) and location C (near the rectangular pad). For each of these three locations at the six experimental states, longitudinal strain distributions from the top to the bottom of the beam were plotted in Figures 6.18 (1)–(6). The brown dashed lines denote the geometric mid-line of the microbeam, whereas the black dashed lines represent the neutral axis according to the definition, i.e., the axis in the cross section of a beam along which the longitudinal stress and strain are zero. At the state (1), the tension and compression sides of the three locations were not differentiated. At the first hold segment, the strain distributions were separated by the black dashed line with the maximum compressive strain lower than the maximum tensile strain. After the first unloading, the strain of location A was a little bit recovered. The neutral axis was still close to the compression side. When the beam was reloaded to 0.38

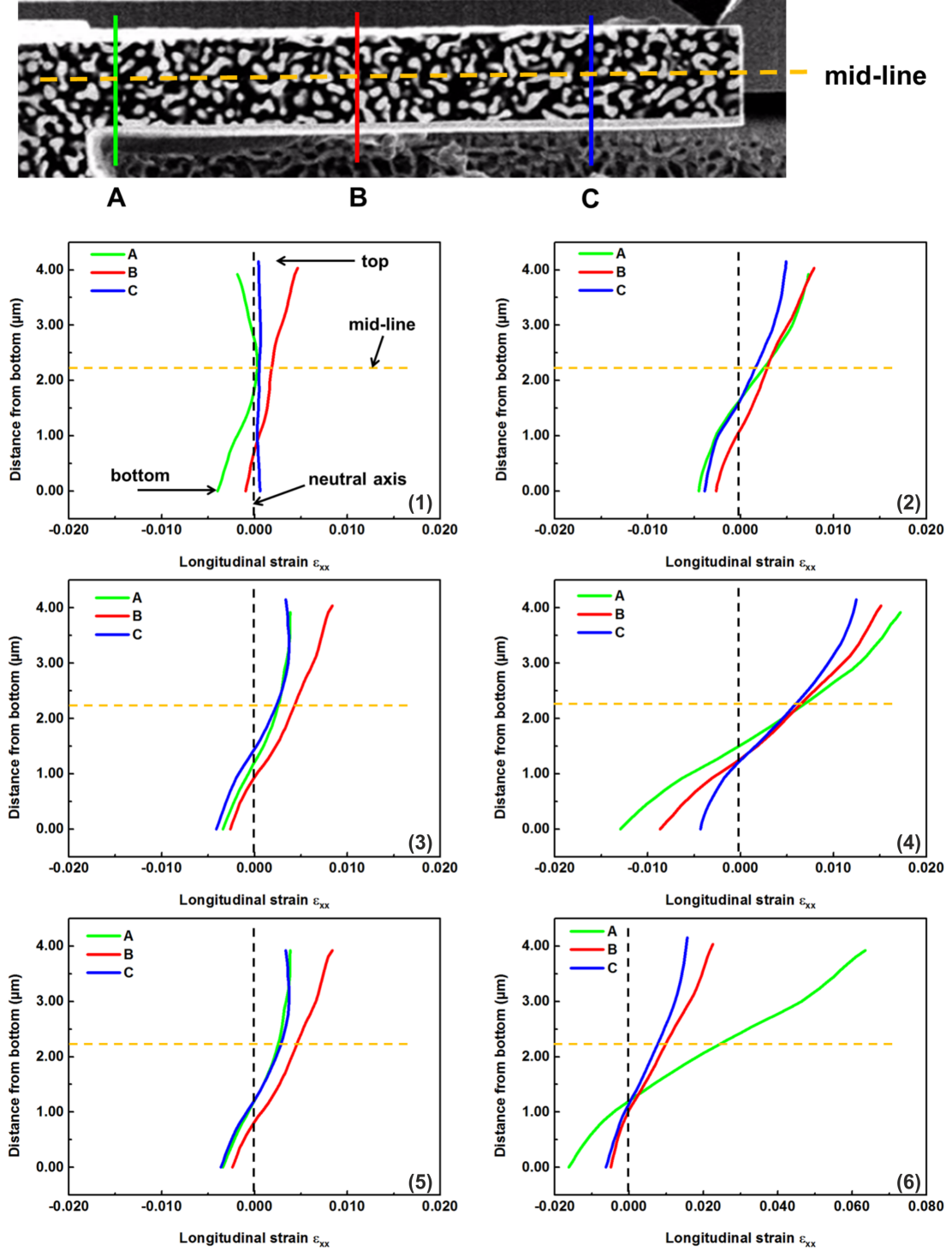


Figure 6.18: Longitudinal strain distributions at six experimental states ((1)–(6)) and three locations on the side surface of the microbeam (A, B, C) measured by DIC: (1) the indenter tip starts touching the beam; (2) at the first hold segment; (3) at the end of the first unloading; (4) at the second hold segment; (5) at the end of the second unloading; (6) just before fracture. The brown dashed lines denote the geometric mid-line of the microbeam, and the black dashed lines represent the neutral axis where $\epsilon_{xx}=0$. As the deformation progression, the neutral axis moves towards to the compression side, which indicates that sample composite_400nm is stronger in compression than in tension.

mN at the second hold segment, the tension and compression regions were both increased, especially for location A where the strain was more than doubled. At the end of the second unloading, the strain was recovered and the distributions were quite similar to that of state (3). After that, the deflection of the beam was increased further until it broke near the support, where the maximum load was 0.41 mN and longitudinal tensile strain was about 7%.

Throughout the microbeam bending testing, it was observed that as the deformation progression, the neutral axis moved towards to the compression side, which indicates that the npg-epoxy composites with mean ligament diameter of 421 nm is stronger in compression than in tension. However, it was found that there is a thin layer of redeposition at the bottom of the beam, which was formed during the microbeam fabrication, and its thickness is close to the mean ligament diameter. As already stated, in order to obtain sharp images during the experiment for the DIC measurement, the last step of the microbeam fabrication is to make a clean cross section cut for the side surface. The redeposition during this step will be accumulated on the bottom surface of the beam. It is unclear how the redeposition layer influences the mechanical response of the microbeam bending experiment at present.

Failure behavior

Interfacial failure and failure within individual phases were observed during the microbending testing. From the SEM images of the microbeam after final unloading shown in Figure 6.19, it was found that cracks formed near the support on the tension side. An enlarged view of the fracture shows that there are delaminations at the gold/epoxy interfaces, and cracks in the gold and epoxy phases. The delaminations follow the boundaries of the ligament and epoxy, and propagate into the epoxy until they meet at a ligament which resists the crack growth. Some of them are aligned with an inclined angle to the beam's length direction, which is marked as x-axis, whereas others are almost perpendicular to the x-axis. This information indicates that the failure happened under tensile and shear stress. Additionally, slip bands are observed near cracks of the individual ligaments, which indicates dislocation activities. The top view of the microbeam shows that there is significant necking with the ligaments at the fracture position, as shown in Figure 6.19(d). It seems that the stress is concentrated near the support which leads to the final fracture. However, since the bending of a triangular in-plane beam provides constant plane strain on the top and the bottom, the material is expected to yield simultaneously at all points along the beam. The reason for the nonuniform yield might be attributed to the geometry defects and ion beam damages near the support during the microbeam fabrication, except for the heterogeneous microstructure of the composite.

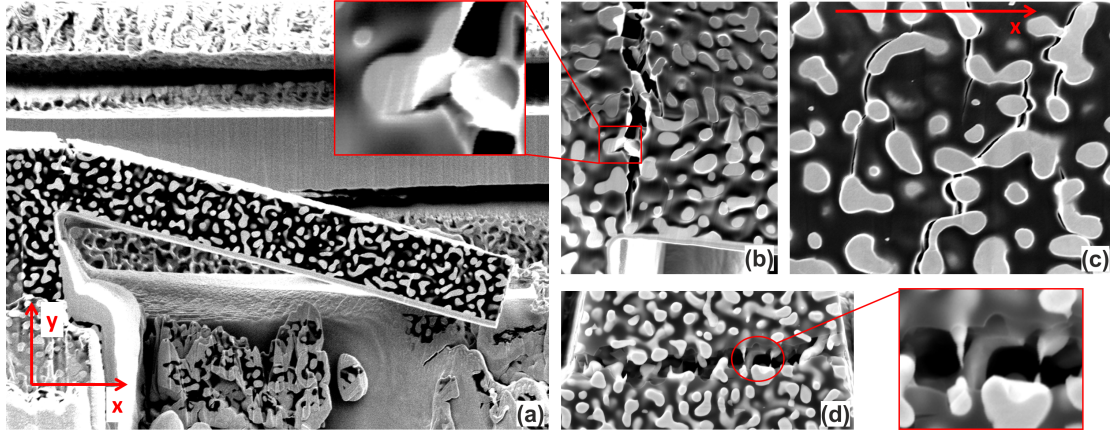


Figure 6.19: (a) A microbeam after failure with fracture near the support. The direction along the beam's length is marked as x-axis, and the y-axis is along the beam's thickness; (b) an enlarged view of the fracture shows interfacial failure at the gold/epoxy interface, and cracks in the gold and epoxy phases. Slip bands are observed in the ligaments; (c) top surface of a microbeam shows failure under tensile and shear stress at the interface and in the epoxy; (d) top view of a microbeam shows significant necking within the ligaments at the fracture position.

6.2 Mechanical behavior of structural geometry

A FEM simulation was carried out for the 3D reconstruction RV of sample composite_400nm with a cubic length of $6\text{ }\mu\text{m}$. The material constants input for the simulation were introduced in Chapter 3. The meshed 3D reconstruction shown in Figure 6.20(a) was uniaxially compressed to 6% engineering strain. The engineering stress-strain curves of the simulation and a microcompression test on the sample composite_400nm were compared, as shown in Figure 6.20(b). The elastic modulus obtained from the initial loading slope in the strain range of 0 to 0.002 of the simulation is 9.7 GPa and from CSM of the microcompression testing is about 10 GPa. The yield stress from the simulation is about 120 MPa, as determined from the 0.2% strain offset in the stress-strain curve, which is quite close to the experimental result of about 140 MPa.

The strain distributions of the gold and epoxy phases at 6% global strain obtained from one cross section of the model is shown in Figure 6.21. The load was applied perpendicular to the paper plane. It was observed that the strain in the epoxy phase is much higher than that in the gold phase, which is consistent with the big difference in the material parameters of the two phases. In the epoxy phase, there are strong strain concentrations, which are found mostly near the concave interfaces. The high strains distribute in the near-interface regions of the epoxy and part of the bulk epoxy. Near some of the convex interfaces of the epoxy, the strain is relatively small and close to that in the gold phase. In the gold phase,

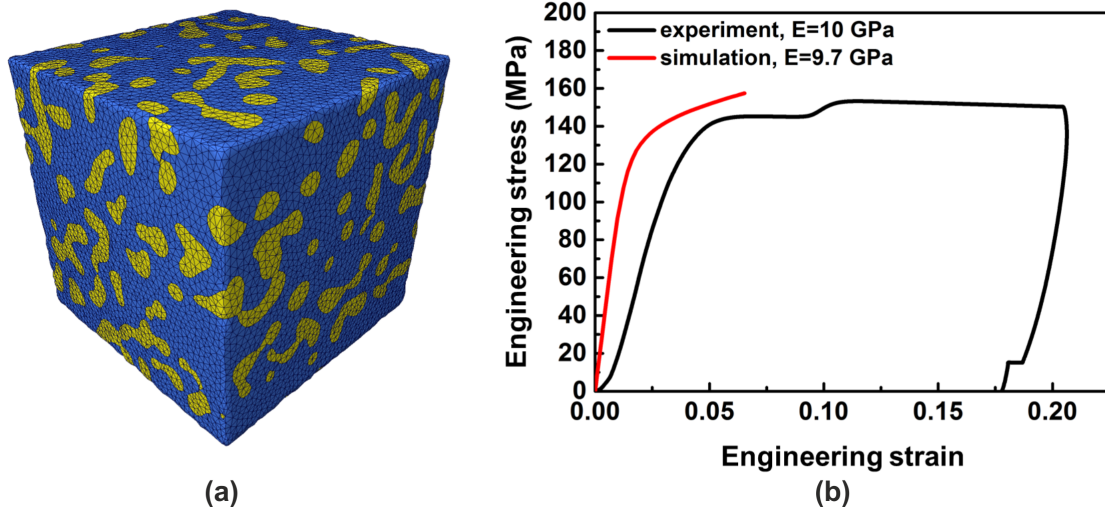


Figure 6.20: (a) 3D mesh of a reconstruction of sample composite_400nm with a cubic length of $6 \mu\text{m}$. The gold ligaments are yellow with a volume fraction of 32.6%, and the epoxy is blue; (b) engineering stress–strain curves of the FEM simulation and the microcompression testing. The elastic modulus and the yield stress of the simulation are quite close to the experimental results.

however, the strain concentrations are less intensive, which were found near the convex interfaces and the ligaments with small diameters.

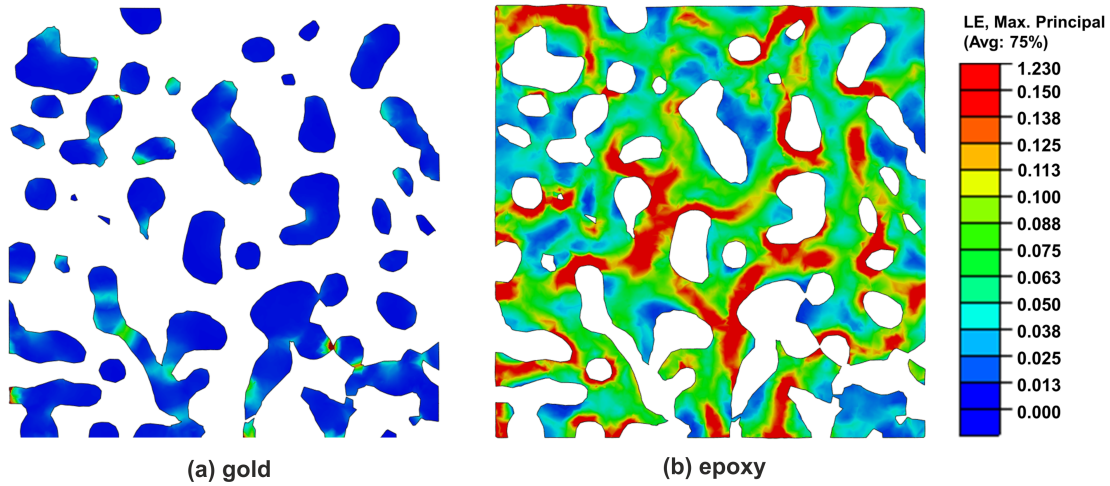


Figure 6.21: Strain distributions of (a) gold and (b) epoxy in one of the cross sections of the RV at 6% global compressive strain. The load was applied perpendicular to the paper plane. Strong strain concentrations were found mostly on the concave interfaces of the epoxy. The high strain distributes in the near-interface regions of the epoxy and part of the bulk epoxy. Near some of the convex interfaces of the epoxy, the strain is relatively small and close to that in the gold phase. In the gold phase, the strain concentrations are less intensive, which are found near the convex interfaces and the ligaments with small diameters.

6.3 Discussion

6.3.1 Size effect in hardness and yield strength

From the micromechanical testing, it was found that npg-epoxy composites exhibit size effects in the hardness and yield strength. As can be seen from Figure 6.5, the hardness and mean ligament diameter relationship can be described as a power law: $H \propto \langle D \rangle^{-0.11 \pm 0.01}$. A power law fit to the yield stress for all the samples shown in Figure 6.11 gives a relation of $\sigma_y \propto \langle D \rangle^{-0.17 \pm 0.03}$. These results are comparable to the one obtained from the Vickers hardness testing for npg-epoxy composites, which gives a power law relation of $H_v \propto \langle D \rangle^{-0.18 \pm 0.04}$ [42]. The different values of the power law exponent could be caused by different samples and test methods that were utilized in the experiments. It should be noticed that the absolute values of these power law exponents are much lower than that of the pure npg and gold microcolumns reviewed in Chapter 2, indicating that the size effects in hardness and yield strength of npg-epoxy composites is much weaker than that of pure npg and bulk gold.

Since the npg-epoxy composites consist of gold, epoxy phases, and the interface between them, the microstructure of each phase and their interactions at the interface need to be taken into account for the understanding of the size effect.

- (1) The harder phase, i.e., the gold ligaments may contribute largely to the mechanical behavior of the composite. Gold at the nanometer scale shows a strong size effect, which have been interpreted by dislocation source limited deformation [17, 49–51]. The lack of effective dislocation sources in smaller ligaments leads to higher stress to initiate yield. Additionally, the strain gradient plasticity model was proposed to explain the high strength of ligaments in npg due to the bending dominated deformation [48]. The strain gradient in the plastic hinge of the ligaments is accommodated by geometrically necessary dislocations, which obstruct the deformation and strengthen the material. As for the npg-epoxy composites, due to the infiltrated epoxy phase, it is unlikely that the dominated deformation mode is still bending. It is expected that the strain gradient hardening effect is not as strong as that in the pure npg.
- (2) The mobility of the epoxy chains is restricted by the interface, which limits the deformation and leads to the strengthening of the material [156]. This interfacial interaction between the ligament network and the epoxy chains is enhanced for the smaller ligament size samples due to the larger interface specific surface area.
- (3) The interface hinders the dislocation motions. For pure npg, dislocations may leave the ligaments' free surface and a high stress is needed for new dislocations

nucleation, which is known as the dislocation starvation mechanism [16,18,20]. However, for the npg-epoxy composites, since the ligaments are surrounded by the epoxy, once the dislocations are activated, their movements are highly constrained at the interface. The deformation is expected to occur by the nucleation and pile-up of the dislocations in the ligaments until the applied stress is large enough to break the bond between the gold and the epoxy. Samples with larger specific surface area are expected to experience stronger influences from such dislocation-interface interactions. As a result, the number of dislocations in the pile-up is increased and the stress required to move the dislocations is increased. As can be seen from Figure 4.18, the specific surface area of the interface increases with decreasing mean ligament diameter. Therefore, npg-epoxy composites with smaller mean ligament diameter is expected to experience more intensive dislocation-interface interactions, which strengthening the material. However, due to the less dislocation sources in the smaller ligaments, the number of dislocations could be much less than that in the larger ligaments. As a result, the dislocation pile-ups of the npg-epoxy composite with larger mean ligament diameter might be more intensive. That is to say, the strengthening effect due to the dislocation pile-ups in the larger ligament sample may be stronger than that in the smaller ligament sample. Therefore, it is possible that the combined effects of the dislocation activities at the interface and the dislocation source limited deformation weaken the size effect of npg-epoxy composites.

6.3.2 Elastic modulus predictions using analytical models

Various analytical models, based on idealized unit cells that are analogous to the microstructure of the composites, have been used for the predictions of the elastic modulus, as reviewed in Chapter 2. For the npg-epoxy composites with bicontinuous network microstructure, the gold ligaments act as the reinforcing phase and the epoxy acts as the matrix phase. The applicability of the analytical models on the prediction of the elastic modulus of npg-epoxy composites is discussed in this section. By comparing the results from the analytical models, the experiments and the FEM simulations, it is able to investigate the influence of the structural geometry on the mechanical behavior of npg-epoxy composites.

Figure 6.22 shows the comparison of the isostrain (black solid line) and isostress (green solid line) conditions, the two bounds of the Ravichandran model for the composites with discontinuous reinforcements (red solid line), the two bounds of the Tuchinskii model for the composites with bicontinuous phases (blue solid line), together with the experimental and FEM simulation results (intersection of the right vertical dashed line and the horizontal dashed line). As can be seen, the most idealized conditions isostrain and isostress have the most broad bounds. Both the

Ravichandran and the Tuchinskii models provide much narrower bounds. The Tuchinskii bounds are higher than that of the Ravichandran model. The experimental and the FEM simulation results are almost the same at around 10 GPa, which are close to the isostress condition and within the Ravichandran bounds. These different observations are discussed in four aspects: connectivity, effective relative density, directional tortuosity, and interface.

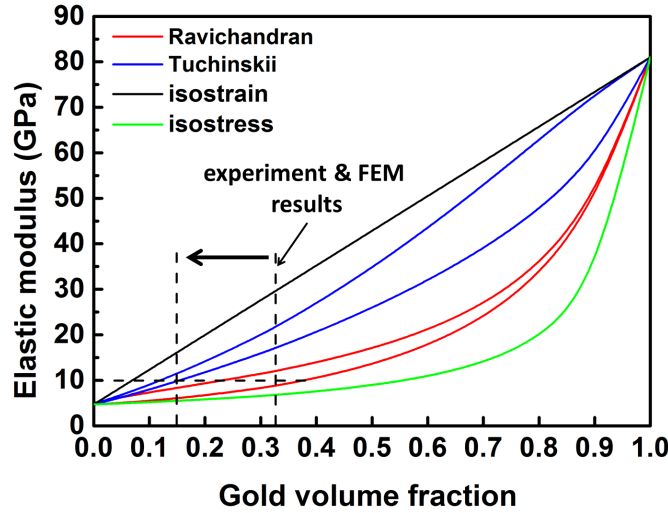


Figure 6.22: The comparison of the elastic modulus results from the isostrain and isostress conditions, the two bounds of the Ravichandran model for the composites with discontinuous reinforcements, the two bounds of the Tuchinskii model for the composites with bicontinuous phases, the experiment and the FEM simulation. When the effective relative density is used for the calculation, the results are shifted from the right dashed line to the left one, as indicated by the horizontal arrow.

Connectivity

As introduced in Chapter 2, the Tuchinskii model describes a bicontinuous composite structure using a simplified unit cell, which consists of straight interconnected rectangular beams, whereas the reinforcement in the Ravichandran model is discontinuous. The interconnectivity of the two phases with different stiffnesses in the bicontinuous composite provides a preferred stress transfer path. It was found that the stress transfer path exist completely within the stiffer phase, i.e., the reinforcement [68]. The 3D spatial connections of the reinforcement allows the stress transfer over a much larger area than in the structure with discontinuous reinforcement. Moreover, in the Tuchinskii model, all the rectangular beams contribute to the connections. This is different from the ligament network structure of the npg-epoxy composites, where only about half of the ligament volume contribute to the connections, as discussed in Chapter 5. It seems reasonable that the Ravichandran bounds, the experimental and the FEM simulation results are

lower than that of the Tuchinskii model due to their different connectivities, which is worth to be quantified for these different models in the future.

Effective relative density

The effective relative density of npg has been proved to be the critical structural parameter in determining its mechanical behavior, as discussed in Chapter 5. For the npg–epoxy composites analyzed in this section, the effective relative density of the gold network is about 15.0%. With this gold volume fraction, it was found that the experimental and the FEM simulation results are close to the lower bound of the Tuchinskii prediction, as illustrated in the intersection of the left vertical and the horizontal dashed lines in Figure 6.22. This result point to the importance of the load bearing structure of the reinforcement for the determination of the mechanical behavior of npg–epoxy composites.

Directional tortuosity

It was found that the stiffness of the npg structure is inversely proportional to the directional tortuosity, as discussed in Chapter 5. The directional tortuosity of npg is bigger than 1 due to its microstructure. However, for the Tuchinskii model, the idealized straight rectangular beam structure gives a directional tortuosity of 1, which leads to a stiffer behavior than that of the npg–epoxy composites.

Interface

It should be noticed that in the analytical models and the FEM simulations, the two phases in the composites were assumed to be perfectly bonded at the interface. So that the interface is considered to have an infinite stiffness, and a complete load transfer takes place between the reinforcement and the matrix. In reality, the interface always has a finite stiffness and prevents an effective stress transfer during loading. This is one of the possible reasons that the experimental result is lower than the Tuchinskii model prediction. Additionally, since the interfacial failure of the npg–epoxy composites observed from the experiment occurred with plastic deformation, it is not surprising that the FEM simulation result is almost equal to the experimental result.

6.3.3 Interfacial failure

The existence of interface between the gold and the epoxy phases leads to a direct implication on the failure mechanisms of the npg–epoxy composites. Due to the different mechanical properties of gold and epoxy, and the irregular geometries of the ligaments, high strains are likely to concentrate in the softer epoxy phase near the interface where the local curvature is high. It undergoes higher strains than the hard gold phase when the same global load is applied, as has been observed from the FEM simulations of the 3D reconstruction. Once the interfacial

bond strength is not strong enough to withstand the high stress concentration at the interface, debonding occurs.

It was noticed that at some of the interfaces with high local curvature, there is no failure. This may indicate that the interface with high curvature is a necessary but not sufficient condition that leads to the failure. One important issue that needs to be considered is the load bearing structure of the ligaments. As discussed in Chapter 5 and previous section, the load bearing rings of the ligaments contribute to the stiffness of the npg structure, and in the npg–epoxy composites. The stress is more likely to be transferred in the load bearing ligament structures. The dangling ligaments which don't contribute to the connectivity are less likely to be the stress concentration parts. In the FEM simulation presented in section 6.2, near some of the convex interfaces of the epoxy, the strain is relatively small, as shown in Figure 6.21. These regions might be located near the dangling ligaments which contribute little to the load bearing. The epoxy nearby experiences small strain. Thus, it is likely that the interfacial failure happens depending on the stress transmission structure as well, apart from the discrepancy of the mechanical properties of the gold and the epoxy phases, the interface geometry and the bonding strength.

6.3.4 Tension–compression asymmetry

The tension–compression asymmetry was found in both the pure npg and the npg–epoxy composites. In pure npg, it was explained by the density change in different loading states [42,46]. Under compression, there is little transverse plastic strain and the densification of the ligament network leads to stiffening of the structure and provides a stable and uniform plastic flow in the material [42]. However, under tensile stress, the plastic flow reduces the density. Local stress concentrations at the ligaments lead to shear instability and brittle failure [28].

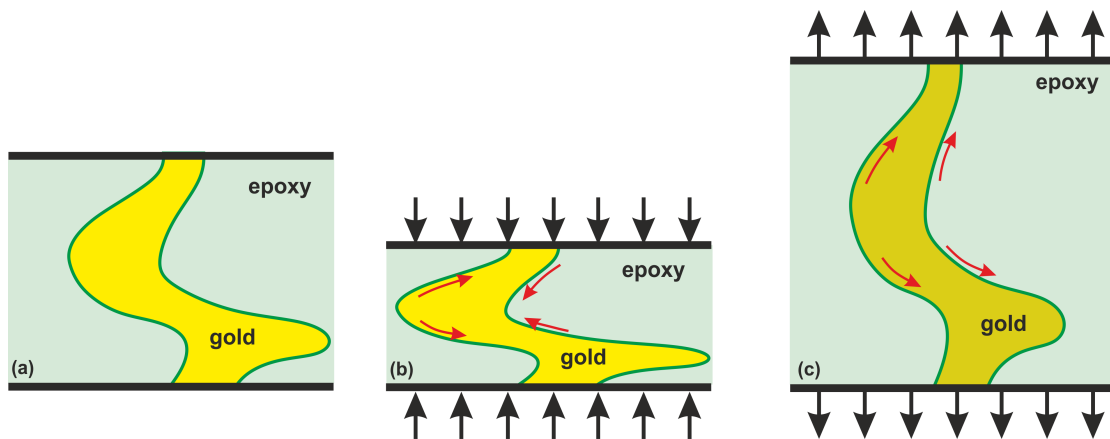


Figure 6.23: Schematic illustrations of npg–epoxy composites (a) without load; (b) under compression; (c) under tension. The interface between the gold and the epoxy phases is shown in green.

After infiltration with epoxy, the densification of the npg–epoxy composites

is strongly suppressed, as observed from the micromechanical experiments. The weaker phase in the composite, i.e., the epoxy, is basically a brittle material, whose tensile yield strength is significantly less than the compressive yield strength. The stress prefers to transfer in the stiffer phase of the composites, which is the gold. Under compression, the ligaments tend to align perpendicular to the loading axis, as schematically illustrated in Figure 6.23(b). As a result, the ligaments and the epoxy phases are compacted together, leading to geometric stiffening of the composite. However, when it is under tension, as illustrated in Figure 6.23(c), the ligaments tend to align parallel to the loading axis, and the materials near the interface are under local tensile and shear stress, which lead to failure and weakening of the material.

6.4 Conclusions

In this chapter, nanoindentation based micromechanical experiments, 3D microstructural characterization and FEM simulations were carried out for the npg-epoxy composites in order to understand the influence of the epoxy infiltration on the mechanical behavior, mechanisms of deformation and failure. The key conclusions can be drawn as follows:

- The npg-epoxy composites show weaker ligament length scale dependent hardness and yield strength than that of pure npg and bulk gold, whereas the elastic modulus remains constant. The size effect could be attributed to the dislocation source limited deformation in the ligaments, the promoted interfacial interaction between the ligament networks and the epoxy chains due to the higher specific surface area of smaller ligament size samples, and the constrained dislocation activities at the interface.
- The comparisons of the elastic moduli from the analytical models predictions, the experimental and FEM simulation results point to the influences of the connectivity, the effective relative density of the load bearing ligament structure, the directional tortuosity of the ligaments, and the interface on the elastic behavior of the npg-epoxy composites.
- It was experimentally observed that there is interfacial failure under compressive stress, which might be attributed to the combined effects of the difference of the mechanical properties of the gold and the epoxy phases, the interface geometry and the bonding strength, and the stress transmission in the load bearing ligament structure. Under tensile stress, interfacial failure and failure within individual phases were found. These failure behaviors on the one hand demonstrates the importance of the interface on the mechanical behavior of npg-epoxy composites. On the other hand, they reflect

the asymmetric mechanical properties under compression and tension of the composites.

- The tension-compression asymmetry was examined using a triangular in-plane geometry microbeam bending testing. It was found that npg-epoxy composites is stronger in compression than in tension, which was attributed to the infiltrated soft phase, i.e., the epoxy, the ligament alignments at different loading states, and the interface.

7. Summary and Future Work

7.1 Summary

A three-fold investigation of npg-epoxy composites produced from as-dealloyed to isothermally annealed npg with mean ligament diameters of 27 nm, 45 nm, 210 nm, 365 nm and 421 nm was carried out, focusing on 3D microstructural characterization using high resolution 3D FIB-SEM tomography, FEM simulations on the meshed 3D reconstructions, and nanoindentation based micromechanical testing to understand the influence of the structural geometry and the infiltrated epoxy on the mechanical response, the mechanisms of deformation and failure of npg-epoxy composites with regard to the three questions raised in Chapter 1, i.e., how do the structural length-scales and 3D geometry of the gold phase influence the mechanical behavior? how does the existence of the epoxy phase influence the composite mechanical response? What are the deformation and failure mechanisms?

In order to understand the composite microstructure, a 3D microstructural characterization approach for the npg ligament network of the five npg-epoxy composite samples was established. By quantitatively analyzing the 3D reconstructions in terms of metric properties (e.g., relative density, ligament diameter distribution and specific surface area), topological properties (e.g., connectivity density), and directional properties (e.g., directional tortuosity) in a spatial and volume dependent approach, the microstructural representative volumes of the gold phase of the composites were determined. They reflect the global structural properties of the material, and are assumed to be equivalent to the pure npg network. It was found that the cubic lengths of the RVs were about 15 times the mean ligament diameter, and the npg structure coarsens in a nearly self-similar manner in terms of the ligament diameter distribution and the scaled connectivity density. The self-similarity allows to identify the critical structural parameters that can be used to describe the mechanical behavior of npg structural geometry over varying length scales.

The critical microstructural parameters in determining the mechanical behavior of the npg network were identified with a combined experimental and FEM simulation approach. Nanoindentation and *in-situ* microcompression testing for

a pure npg sample, and FEM simulations for the meshed 3D reconstructions of the npg network structure were carried out. It was found that the mechanical behavior of the 3D reconstructions exhibits a finite volume effect with the RV sizes similar to that of the microstructure. The RVs show mechanical anisotropy which was correlated with the directional tortuosity, i.e., smaller directional tortuosity leads to a stiffer mechanical response. Both the micromechanical testing and the simulations show that there is little lateral expansion of the investigated volume, which indicates near zero Poisson's ratio of npg structure. FEM simulations on the npg 3D reconstructions of samples at the early, the mid and the last stage of annealing investigated in this work show that the mechanical response are quite similar, which strongly support the self-similarity of npg structural geometry during coarsening. A reasonable fit between the simulations and the experimental results was achieved. It was found that the elastic modulus and the yield stress of npg and its 3D reconstructions are more than one order of magnitude lower than the predictions by the Gibson–Ashby scaling relations and most of the results reported in the literature. To explain this big discrepancy, it was found that the effective relative density of the load bearing structure was the critical parameter that determine the mechanical behavior of npg structural geometry, instead of the solid relative density usually used in the Gibson–Ashby scaling relations.

Having investigated the influences of the structural geometry on the mechanical behavior of npg, the effects of the infiltrated softer phase, i.e., the epoxy was explored. The nanoindentation based micromechanical testing, i.e., nanoindentation, microcompression and microbeam bending, and 3D microstructural characterization and FEM simulations were carried out for the npg–epoxy composites. It was found that the composites show weaker size effect in the hardness and yield strength than that of pure npg and bulk gold, whereas the elastic modulus remains constant. The size effect could be attributed to the dislocation source limited deformation in the gold, the interfacial interactions between the ligament networks and the epoxy chains, and the constrained dislocation activities due to the interface. The comparisons of the elastic moduli from the analytical models predictions, the experiments, and the FEM simulations point to the influences of the connectivity, the effective relative density of the load bearing ligament structure, the directional tortuosity of the ligaments, and the interface on the elastic behavior of the npg–epoxy composites. The interfacial phenomena was actually experimentally observed. It was found that there is interfacial failure under compressive stress, which might be attributed to the combined effects of the difference of the mechanical properties of the two phases, the interface geometry and the bonding strength, and the stress transmission in the load bearing ligament structure. Under tensile stress, there are interfacial failure and failure within the individual phases. These failure behaviors on the one hand again demonstrates the

importance of the interface on the mechanical behavior of npg-epoxy composites. On the other hand, they reflect the different mechanical properties under compression and under tension of the composites. The tension-compression asymmetry of the composites was examined using a triangular in-plane geometry microbeam bending test combined with a DIC measurement. It was found that the npg-epoxy composite is stronger in compression than in tension. This was attributed to the infiltrated soft phase, i.e., the epoxy, the ligament alignments at different loading states, and the interface.

Overall, the present thesis presented a comprehensive approach for 3D microstructural characterization, FEM simulation and micromechanical testing for npg-epoxy composites. The various observations point to the important roles that the hard phase, i.e., the interconnected ligament network, the soft phase, i.e., the continuous epoxy, and the interface between them play on the mechanical behavior of npg-epoxy composites. A brief summary of the thesis is shown in Table 7.1.

7.2 Suggestions for future work

Several issues are worth noting as future work:

- Mechanical behavior of the npg structural geometry from FEM simulations and micromechanical testing presented in this thesis has big discrepancy compared to that reported in most of the literature. This might be attributed to different npg sample fabrication approaches. It was demonstrated in this thesis that the effective relative density may be the critical structural parameter that determine the mechanical behavior of npg. It might be useful to characterize such structural property of npg fabricated from different methods, in order to find the reasons of the big mechanical behavior discrepancy.
- Due to the high specific surface area between the gold and the epoxy phases, mechanical properties of npg-epoxy composites may depend on possible interphase between them, except for the interface. The interphase is a transition region where there is a high interaction between the epoxy chains and the ligament surface. It may have different properties compared to that of both the gold and the epoxy phases, and control the load transfer between both components. Advanced mechanical and microstructural characterization and modelings for the interphase are useful to understand the mechanical behavior of npg-epoxy composites.

Table 7.1: Summary of the thesis

Sample		3D microstructural characterization of npg	Mechanical behavior of npg		Mechanical behavior of npg-epoxy composites
Name	Description		approaches: nanoindentation, insitu microcompression and DIC results: elastic modulus and yield stress are more than one order of magnitude lower than the predictions by the Gibson-Ashby scaling model.	approaches: FEM simulation for the meshed 3D reconstruction of the npg network, fit to the microcompression testing data. results: (1) mechanical behavior RV consistent with microstructural RV; (2) RVs show mechanical anisotropy, correlated with directional tortuosity; (3) npg 3D reconstructions of samples at the early, the mid and the last stage of annealing investigated in this work show that the mechanical response are quite similar, which strongly support the self-similarity of npg structural geometry during coarsening; (4) the effective relative density of the load bearing structure is the critical parameter that determine the mechanical behavior of npg structural geometry.	
npg_400nm	pure npg with mean ligament diameter of about 400 nm	/		/	/
composite_20nm	(1) npg pore structure infiltrated with epoxy; (2) the gold phase structure is assumed to be equivalent to the pure npg network.	approaches: (1) FIB-SEM tomography experiments; (2) quantitative analyses of the metric properties (e.g., relative density, ligament diameter distribution and specific surface area), topological properties (e.g., connectivity density), and directional properties (e.g., directional tortuosity) of the npg network 3D reconstructions in a spatial and volume dependent approach. results: (1) cubic lengths of the microstructural RVs are about 15 times the mean ligament diameter; (2) npg structure coarsens in a nearly self-similar manner in terms of the ligament diameter distribution and the scaled connectivity density, which allows to identify the critical structural parameters that can be used to describe the mechanical behavior of npg structural geometry over varying length scales.	/		approaches: nanoindentation, microcompression, microbeam bending, DIC, 3D microstructural characterization, and FEM simulations. results: (1) npg-epoxy composites show weaker size effect in the hardness and yield strength than that of pure npg and bulk gold, whereas the elastic modulus remains constant. The size effect could be attributed to the dislocation source limited deformation in the gold, the interfacial interactions between the ligament networks and the epoxy chains, and the constrained dislocation activities due to the interface; (2) the connectivity, the effective relative density of the load bearing ligament structure, the directional tortuosity of the ligaments, and the interface may determine the elastic behavior of the composite; (3) interfacial failure under compressive stress, and interfacial failure and failure within the individual phases under tensile stress are observed; (4) tension-compression asymmetry of the composites: stronger in compression than in tension.
composite_50nm					
composite_200nm					
composite_350nm					
composite_400nm					

Bibliography

- [1] J Weissmüller, R N Viswanath, D Kramer, P Zimmer, R Würschum, and H Gleiter. Charge-induced reversible strain in a metal. *Science*, 300(5617):312–315, 2003.
- [2] Hai-Jun Jin, Xiao-Lan Wang, Smrutiranjana Parida, Ke Wang, Masahiro Seo, and Jorg Weissmüller. Nanoporous Au–Pt alloys as large strain electrochemical actuators. *Nano letters*, 10(1):187–194, 2009.
- [3] Yi Ding and Mingwei Chen. Nanoporous metals for catalytic and optical applications. *MRS bulletin*, 34(08):569–576, 2009.
- [4] J Biener, A Wittstock, LA Zepeda-Ruiz, MM Biener, V Zielasek, D Kramer, RN Viswanath, J Weissmüller, M Bäumer, and AV Hamza. Surface-chemistry-driven actuation in nanoporous gold. *Nature materials*, 8(1):47–51, 2009.
- [5] Arne Wittstock, Jürgen Biener, and Marcus Bäumer. Nanoporous gold: a new material for catalytic and sensor applications. *Physical Chemistry Chemical Physics*, 12(40):12919–12930, 2010.
- [6] Yi Ding, Y-J Kim, and Jonah Erlebacher. Nanoporous gold leaf: Ancient technology/advanced material. *Advanced materials*, 16(21):1897–1900, 2004.
- [7] Jörg Weissmüller, Roger C Newman, Hai-Jun Jin, Andrea M Hodge, and Jeffrey W Kysar. Nanoporous metals by alloy corrosion: formation and mechanical properties. *Mrs Bulletin*, 34(08):577–586, 2009.
- [8] Tobias Hanrath, Joshua J Choi, and Detlef-M Smilgies. Structure/processing relationships of highly ordered lead salt nanocrystal superlattices. *ACS nano*, 3(10):2975–2988, 2009.
- [9] Jonah Erlebacher, Michael J Aziz, Alain Karma, Nikolay Dimitrov, and Karl Sieradzki. Evolution of nanoporosity in dealloying. *Nature*, 410(6827):450–453, 2001.
- [10] Yi Ding and Zhonghua Zhang. Nanoporous metals. In *Springer handbook of nanomaterials*, pages 779–817. Springer, 2013.

- [11] Rong Li and K Sieradzki. Ductile–brittle transition in random porous Au. *Physical Review Letters*, 68(8):1168, 1992.
- [12] Warren C Oliver and Georges M Pharr. An improved technique for determining hardness and elastic modulus using load and displacement sensing indentation experiments. *Journal of materials research*, 7(06):1564–1583, 1992.
- [13] Warren C Oliver and Georges M Pharr. Measurement of hardness and elastic modulus by instrumented indentation: Advances in understanding and refinements to methodology. *Journal of materials research*, 19(01):3–20, 2004.
- [14] Michael D Uchic, Dennis M Dimiduk, Jeffrey N Florando, and William D Nix. Sample dimensions influence strength and crystal plasticity. *Science*, 305(5686):986–989, 2004.
- [15] J N Florando and W D Nix. A microbeam bending method for studying stress–strain relations for metal thin films on silicon substrates. *Journal of the Mechanics and Physics of Solids*, 53(3):619–638, 2005.
- [16] Julia R Greer and William D Nix. Size dependence of mechanical properties of gold at the sub–micron scale. *Applied Physics A*, 80(8):1625–1629, 2005.
- [17] Cynthia Ann Volkert and Erica T Lilleodden. Size effects in the deformation of sub–micron Au columns. *Philosophical Magazine*, 86(33–35):5567–5579, 2006.
- [18] William D Nix, Julia R Greer, Gang Feng, and Erica T Lilleodden. Deformation at the nanometer and micrometer length scales: Effects of strain gradients and dislocation starvation. *Thin Solid Films*, 515(6):3152–3157, 2007.
- [19] Bin Wu, Andreas Heidelberg, and John J Boland. Mechanical properties of ultrahigh–strength gold nanowires. *Nature materials*, 4(7):525–529, 2005.
- [20] Julia R Greer and William D Nix. Nanoscale gold pillars strengthened through dislocation starvation. *Physical Review B*, 73(24):245410, 2006.
- [21] Michael D Uchic, Paul A Shade, and Dennis M Dimiduk. Plasticity of micrometer–scale single crystals in compression. *Annual Review of Materials Research*, 39:361–386, 2009.
- [22] Julia R Greer and Jeff Th M De Hosson. Plasticity in small–sized metallic systems: Intrinsic versus extrinsic size effect. *Progress in Materials Science*, 56(6):654–724, 2011.

- [23] Juergen Biener, Andrea M Hodge, and Alex V Hamza. Microscopic failure behavior of nanoporous gold. *Applied Physics Letters*, 87(12):121908, 2005.
- [24] Juergen Biener, Andrea M Hodge, Alex V Hamza, Luke M Hsiung, and Joe H Satcher Jr. Nanoporous Au: A high yield strength material. *Journal of Applied Physics*, 97(2):24301, 2005.
- [25] Juergen Biener, Andrea M Hodge, Joel R Hayes, Cynthia A Volkert, Luis A Zepeda-Ruiz, Alex V Hamza, and Farid F Abraham. Size effects on the mechanical behavior of nanoporous Au. *Nano letters*, 6(10):2379–2382, 2006.
- [26] C A Volkert, E T Lilleodden, D Kramer, and J Weissmüller. Approaching the theoretical strength in nanoporous Au. *Applied Physics Letters*, 89(6):1920, 2006.
- [27] A M Hodge, J Biener, J R Hayes, P M Bythrow, C A Volkert, and A V Hamza. Scaling equation for yield strength of nanoporous open-cell foams. *Acta Materialia*, 55(4):1343–1349, 2007.
- [28] T John Balk, Chris Eberl, Ye Sun, Kevin J Hemker, and Daniel S Gianola. Tensile and compressive microspecimen testing of bulk nanoporous gold. *JOM*, 61(12):26–31, 2009.
- [29] Nicolas J Briot, Tobias Kennerknecht, Christoph Eberl, and T John Balk. Mechanical properties of bulk single crystalline nanoporous gold investigated by millimetre-scale tension and compression testing. *Philosophical Magazine*, 94(8):847–866, 2014.
- [30] Lorna J Gibson and M F Ashby. The mechanics of three-dimensional cellular materials. In *Proceedings of the Royal Society of London A: Mathematical, Physical and Engineering Sciences*, volume 382, pages 43–59. The Royal Society, 1982.
- [31] Lorna J Gibson and Michael F Ashby. *Cellular solids: structure and properties*. Cambridge university press, 1997.
- [32] Dongyun Lee, Xiaoding Wei, Xi Chen, Manhong Zhao, Seong C Jun, James Hone, Erik G Herbert, Warren C Oliver, and Jeffrey W Kysar. Microfabrication and mechanical properties of nanoporous gold at the nanoscale. *Scripta materialia*, 56(5):437–440, 2007.
- [33] Re Xia, Caixia Xu, Wenwang Wu, Xide Li, Xi-Qiao Feng, and Yi Ding. Microtensile tests of mechanical properties of nanoporous Au thin films. *Journal of materials science*, 44(17):4728–4733, 2009.

- [34] Ran Liu and Antonia Antoniou. A relationship between the geometrical structure of a nanoporous metal foam and its modulus. *Acta Materialia*, 61(7):2390–2402, 2013.
- [35] N Huber, R N Viswanath, N Mameka, J Markmann, and J Weiß müller. Scaling laws of nanoporous metals under uniaxial compression. *Acta Materialia*, 67:252–265, 2014.
- [36] Giorgio Pia and Francesco Delogu. Nanoporous Au: Statistical analysis of morphological features and evaluation of their influence on the elastic deformation behavior by phenomenological modeling. *Acta Materialia*, 85:250–260, 2015.
- [37] Nicolas J Briot and T John Balk. Developing scaling relations for the yield strength of nanoporous gold. *Philosophical Magazine*, 95(27):2955–2973, 2015.
- [38] H Rösner, S Parida, D Kramer, C A Volkert, and J Weissmüller. Reconstructing a nanoporous metal in three dimensions: An electron tomography study of dealloyed gold leaf. *Advanced Engineering Materials*, 9(7):535–541, 2007.
- [39] Takeshi Fujita, Li-Hua Qian, Koji Inoke, Jonah Erlebacher, and Ming-Wei Chen. Three-dimensional morphology of nanoporous gold. *Applied Physics Letters*, 92(25):251902, 2008.
- [40] Yu-chen Karen Chen, Yong S Chu, JaeMock Yi, Ian McNulty, Qun Shen, Peter W Voorhees, and David C Dunand. Morphological and topological analysis of coarsened nanoporous gold by x-ray nanotomography. *Applied Physics Letters*, 96(4):43122, 2010.
- [41] Yu-chen Karen Chen-Wiegart, Steve Wang, Yong S Chu, Wenjun Liu, Ian McNulty, Peter W Voorhees, and David C Dunand. Structural evolution of nanoporous gold during thermal coarsening. *Acta Materialia*, 60(12):4972–4981, 2012.
- [42] Ke Wang and Jörg Weissmüller. Composites of nanoporous gold and polymer. *Advanced Materials*, 25(9):1280–1284, 2013.
- [43] Ke Wang. *Composites of Nanoporous Gold and Polymer*. PhD thesis, Technische Universität Hamburg–Harburg, 2015.
- [44] Ke Wang, Aaron Kobler, Christian Kübel, Hans Jelitto, Gerold Schneider, and Jörg Weissmüller. Nanoporous–gold–based composites: toward tensile ductility. *NPG Asia Materials*, 7(6):e187, 2015.

- [45] David Tabor. *The hardness of metals*, volume 10. ClarendonP, 1951.
- [46] Hai-Jun Jin, Lilia Kurmanaeva, Jörg Schmauch, Harald Rösner, Yulia Ivanisenko, and Jörg Weissmüller. Deforming nanoporous metal: Role of lattice coherency. *Acta Materialia*, 57(9):2665–2672, 2009.
- [47] Masataka Hakamada and Mamoru Mabuchi. Mechanical strength of nanoporous gold fabricated by dealloying. *Scripta Materialia*, 56(11):1003–1006, 2007.
- [48] Rui Dou and Brian Derby. Strain gradients and the strength of nanoporous gold. *Journal of Materials Research*, 25(04):746–753, 2010.
- [49] D M Dimiduk, M D Uchic, and T A Parthasarathy. Size-affected single-slip behavior of pure nickel microcrystals. *Acta Materialia*, 53(15):4065–4077, 2005.
- [50] V S Deshpande, A Needleman, and E der Giessen. Plasticity size effects in tension and compression of single crystals. *Journal of the Mechanics and Physics of Solids*, 53(12):2661–2691, 2005.
- [51] A A Benzerga and N F Shaver. Scale dependence of mechanical properties of single crystals under uniform deformation. *Scripta materialia*, 54(11):1937–1941, 2006.
- [52] R Dou and B Derby. Deformation mechanisms in gold nanowires and nanoporous gold. *Philosophical Magazine*, 91(7–9):1070–1083, 2011.
- [53] Ye Sun, Jia Ye, Zhiwei Shan, Andrew M Minor, and T John Balk. The mechanical behavior of nanoporous gold thin films. *Jom*, 59(9):54–58, 2007.
- [54] Rasto Brezny and David J Green. The effect of cell size on the mechanical behavior of cellular materials. *Acta Metallurgica et Materialia*, 38(12):2517–2526, 1990.
- [55] T D Shen, C C Koch, T Y Tsui, and G M Pharr. On the elastic moduli of nanocrystalline Fe, Cu, Ni, and Cu–Ni alloys prepared by mechanical milling/alloying. *Journal of Materials Research*, 10(11):2892–2896, 1995.
- [56] A M Hodge, R T Doucette, M M Biener, J Biener, O Cervantes, and A V Hamza. Ag effects on the elastic modulus values of nanoporous Au foams. *Journal of Materials Research*, 24(04):1600–1606, 2009.
- [57] Anant Mathur and Jonah Erlebacher. Size dependence of effective Young’s modulus of nanoporous gold. *Applied physics letters*, 90(6):1910, 2007.

- [58] Xi-Qiao Feng, Re Xia, Xide Li, and Bo Li. Surface effects on the elastic modulus of nanoporous materials. *Applied Physics Letters*, 94(1):11916, 2009.
- [59] Xi Chen, Yong Xiang, and Joost J Vlassak. Novel technique for measuring the mechanical properties of porous materials by nanoindentation. *Journal of Materials Research*, 21(03):715–724, 2006.
- [60] Nadiia Mameka, Jürgen Markmann, Hai-Jun Jin, and Jörg Weissmüller. Electrical stiffness modulation—confirming the impact of surface excess elasticity on the mechanics of nanomaterials. *Acta Materialia*, 76:272–280, 2014.
- [61] Bao-Nam Dinh Ngô, Alexander Stukowski, Nadiia Mameka, Jürgen Markmann, Karsten Albe, and Jörg Weissmüller. Anomalous compliance and early yielding of nanoporous gold. *Acta Materialia*, 93:144–155, 2015.
- [62] B Roschning and N Huber. Scaling laws of nanoporous gold under uniaxial compression: Effects of structural disorder on the solid fraction, elastic poisson’s ratio, young’s modulus and yield strength. *Journal of the Mechanics and Physics of Solids*, 2016.
- [63] Diana Farkas, Alfredo Caro, Eduardo Bringa, and Douglas Crowson. Mechanical response of nanoporous gold. *Acta Materialia*, 61(9):3249–3256, 2013.
- [64] Deborah DL Chung. *Composite materials: science and applications*. Springer Science & Business Media, 2010.
- [65] Autar K Kaw. *Mechanics of composite materials*. CRC press, 2005.
- [66] David R Clarke. Interpenetrating phase composites. *Journal of the American Ceramic Society*, 75(4):739–758, 1992.
- [67] Wei Zhou, Wenbin Hu, and Di Zhang. Metal–matrix interpenetrating phase composite and its in situ fracture observation. *Materials Letters*, 40(4):156–160, 1999.
- [68] Gregory Albert Del Frari. *The influence of the microstructural shape on the mechanical behaviour of interpenetrating phase composites*. PhD thesis, University of Saskatchewan Saskatoon, 2005.
- [69] JOHN C Halpin and J L Kardos. The Halpin–Tsai equations: a review. *Polymer engineering and science*, 16(5):344–352, 1976.

- [70] Zvi Hashin and Shmuel Shtrikman. A variational approach to the theory of the elastic behaviour of multiphase materials. *Journal of the Mechanics and Physics of Solids*, 11(2):127–140, 1963.
- [71] Kakkaveri S Ravichandran. Elastic properties of two-phase composites. *Journal of the American Ceramic Society*, 77(5):1178–1184, 1994.
- [72] LI Tuchinskii. Elastic constants of pseudoalloys with a skeletal structure. *Powder Metallurgy and Metal Ceramics*, 22(7):588–595, 1983.
- [73] LD Wegner and LJ Gibson. The mechanical behaviour of interpenetrating phase composites–i: modelling. *International Journal of Mechanical Sciences*, 42(5):925–942, 2000.
- [74] Robert J Moon, Matthew Tilbrook, Mark Hoffman, and Achim Neubrand. Al–al₂O₃ composites with interpenetrating network structures: composite modulus estimation. *Journal of the American Ceramic Society*, 88(3):666–674, 2005.
- [75] Z Poniznik, V Salit, M Basista, and D Gross. Effective elastic properties of interpenetrating phase composites. *Computational Materials Science*, 44(2):813–820, 2008.
- [76] T W Clyne and P J Withers. *An introduction to metal matrix composites*. Cambridge University Press, 1995.
- [77] Zhen Qi and Jorg Weissmuller. Hierarchical nested–network nanostructure by dealloying. *ACS nano*, 7(7):5948–5954, 2013.
- [78] John C Russ and Robert T Dehoff. *Practical stereology*. Springer Science & Business Media, 2012.
- [79] Michael D Uchic, Lorenz Holzer, Beverley J Inkson, Edward L Principe, and Paul Munroe. Three–dimensional microstructural characterization using focused ion beam tomography. *Mrs Bulletin*, 32(05):408–416, 2007.
- [80] L Holzer, F Indutnyi, P H Gasser, B Münch, and M Wegmann. Three–dimensional analysis of porous BaTiO₃ ceramics using FIB nanotomography. *Journal of Microscopy*, 216(1):84–95, 2004.
- [81] Philip J Withers. X–ray nanotomography. *Materials today*, 10(12):26–34, 2007.
- [82] Lorenz Holzer and Marco Cantoni. Review of FIB–tomography. *Nanofabrication Using Focused Ion and Electron Beams: Principles and Applications*, 559201222, 2011.

- [83] Katsuyo Thornton and Henning Friis Poulsen. Three-dimensional materials science: an intersection of three-dimensional reconstructions and simulations. *MRS bulletin*, 33(06):587–595, 2008.
- [84] P R Munroe. The application of focused ion beam microscopy in the material sciences. *Materials Characterization*, 60(1):2–13, 2009.
- [85] Cynthia A Volkert and Andrew M Minor. Focused ion beam microscopy and micromachining. *MRS bulletin*, 32(05):389–399, 2007.
- [86] Lucille A Giannuzzi and Others. *Introduction to focused ion beams: instrumentation, theory, techniques and practice*. Springer Science & Business Media, 2006.
- [87] C Motz, T Schöberl, and R Pippan. Mechanical properties of micro-sized copper bending beams machined by the focused ion beam technique. *Acta Materialia*, 53(15):4269–4279, 2005.
- [88] Joachim Mayer, Lucille A Giannuzzi, Takeo Kamino, and Joseph Michael. TEM sample preparation and FIB-induced damage. *Mrs Bulletin*, 32(05):400–407, 2007.
- [89] Hongbin Bei, Sanghoon Shim, M K Miller, G M Pharr, and E P George. Effects of focused ion beam milling on the nanomechanical behavior of a molybdenum-alloy single crystal. *Applied Physics Letters*, 91(11):111915, 2007.
- [90] Jaafar A El-Awady, Christopher Woodward, Dennis M Dimiduk, and Nasr M Ghoniem. Effects of focused ion beam induced damage on the plasticity of micropillars. *Physical Review B*, 80(10):104104, 2009.
- [91] Suhan Kim, Moon Jeong Park, Nitash P Balsara, Gao Liu, and Andrew M Minor. Minimization of focused ion beam damage in nanostructured polymer thin films. *Ultramicroscopy*, 111(3):191–199, 2011.
- [92] N D Bassim, B T De Gregorio, A L D Kilcoyne, K Scott, T Chou, S Wirick, G Cody, and R M Stroud. Minimizing damage during FIB sample preparation of soft materials. *Journal of Microscopy*, 245(3):288–301, 2012.
- [93] Myoung-Woon Moon, Sang Hoon Lee, Jeong-Yun Sun, Kyu Hwan Oh, Ashkan Vaziri, and John W Hutchinson. Wrinkled hard skins on polymers created by focused ion beam. *Proceedings of the National Academy of Sciences*, 104(4):1130–1133, 2007.
- [94] FEI Company. *xT Nova NanoLab Users Manual*, 2006.

- [95] Anthony C Fischer-Cripps and Islam Mustafaev. *Introduction to contact mechanics*. Springer, 2000.
- [96] Ian N Sneddon. The relation between load and penetration in the axisymmetric Boussinesq problem for a punch of arbitrary profile. *International Journal of Engineering Science*, 3(1):47–57, 1965.
- [97] Michael D Uchic and Dennis M Dimiduk. A methodology to investigate size scale effects in crystalline plasticity using uniaxial compression testing. *Materials Science and Engineering: A*, 400:268–278, 2005.
- [98] F A Stevie, L A Giannuzzi, and B I Prenitzer. The focused ion beam instrument. In *Introduction to Focused Ion Beams*, pages 1–12. Springer, 2005.
- [99] Julia Hütsch and Erica T Lilleodden. The influence of focused-ion beam preparation technique on microcompression investigations: Lathe vs. annular milling. *Scripta Materialia*, 77:49–51, 2014.
- [100] Haitao Zhang, Brian E Schuster, Qiuming Wei, and Kaliat T Ramesh. The design of accurate micro-compression experiments. *Scripta Materialia*, 54(2):181–186, 2006.
- [101] Y S Choi, M D Uchic, T A Parthasarathy, and D M Dimiduk. Numerical study on microcompression tests of anisotropic single crystals. *Scripta Materialia*, 57(9):849–852, 2007.
- [102] Daniel Kiener, Christian Motz, and Gerhard Dehm. Micro-compression testing: A critical discussion of experimental constraints. *Materials Science and Engineering: A*, 505(1):79–87, 2009.
- [103] Daniel Kupka. *Fracture experiments of single grain boundaries in ductile metals*. PhD thesis, Technische Universität Hamburg–Harburg, 2013.
- [104] D Kupka, N Huber, and E T Lilleodden. A combined experimental–numerical approach for elasto–plastic fracture of individual grain boundaries. *Journal of the Mechanics and Physics of Solids*, 64:455–467, 2014.
- [105] D Kupka and E T Lilleodden. Mechanical testing of solid–solid interfaces at the microscale. *Experimental Mechanics*, 52(6):649–658, 2012.
- [106] F Iqbal, J Ast, M Göken, and K Durst. In situ micro-cantilever tests to study fracture properties of NiAl single crystals. *Acta Materialia*, 60(3):1193–1200, 2012.

- [107] Eralp Demir, Dierk Raabe, and Franz Roters. The mechanical size effect as a mean-field breakdown phenomenon: Example of microscale single crystal beam bending. *Acta Materialia*, 58(5):1876–1886, 2010.
- [108] Marlene W Kapp, Christoph Kirchlechner, Reinhard Pippan, and Gerhard Dehm. Importance of dislocation pile-ups on the mechanical properties and the Bauschinger effect in microcantilevers. *Journal of Materials Research*, 30(06):791–797, 2015.
- [109] Daniel Kiener, Christian Motz, Thomas Schöberl, Monika Jenko, and Gerhard Dehm. Determination of mechanical properties of copper at the micron scale. *Advanced Engineering Materials*, 8(11):1119–1125, 2006.
- [110] J N Florando. *Measurement of the mechanical properties of copper thin films by microbeam bending*. PhD thesis, Stanford University, 2003.
- [111] W H Peters and W F Ranson. Digital imaging techniques in experimental stress analysis. *Optical engineering*, 21(3):213427, 1982.
- [112] T C Chu, W F Ranson, and M A Sutton. Applications of digital-image-correlation techniques to experimental mechanics. *Experimental mechanics*, 25(3):232–244, 1985.
- [113] H A Bruck, S R McNeill, M Ae Sutton, and W H Peters Iii. Digital image correlation using Newton–Raphson method of partial differential correction. *Experimental Mechanics*, 29(3):261–267, 1989.
- [114] Bing Pan, Kemao Qian, Huimin Xie, and Anand Asundi. Two-dimensional digital image correlation for in-plane displacement and strain measurement: a review. *Measurement science and technology*, 20(6):62001, 2009.
- [115] Bing Pan. Recent progress in digital image correlation. *Experimental Mechanics*, 51(7):1223–1235, 2011.
- [116] Adam D Kammers and Samantha Daly. Digital image correlation under scanning electron microscopy: methodology and validation. *Experimental Mechanics*, 53(9):1743–1761, 2013.
- [117] Matthew R Maschmann, Gregory J Ehlert, Sei Jin Park, David Mollenhauer, Benji Maruyama, A John Hart, and Jeffery W Baur. Visualizing strain evolution and coordinated buckling within CNT arrays by in situ digital image correlation. *Advanced Functional Materials*, 22(22):4686–4695, 2012.
- [118] H Jin, W Y Lu, and J Korellis. Micro-scale deformation measurement using the digital image correlation technique and scanning electron microscope

- imaging. *The Journal of Strain Analysis for Engineering Design*, 43(8):719–728, 2008.
- [119] W A Scrivens, Y Luo, Michael A Sutton, S A Collette, Micheal L Myrick, P Miney, P E Colavita, Anthony P Reynolds, and Xiaodong Li. Development of patterns for digital image correlation measurements at reduced length scales. *Experimental Mechanics*, 47(1):63–77, 2007.
- [120] J Blaber, B Adair, and A Antoniou. Ncorr: Open-source 2D digital image correlation Matlab software. *Experimental Mechanics*, pages 1–18, 2015.
- [121] Bing Pan, Huimin Xie, Zhaoyang Wang, Kemao Qian, and Zhiyong Wang. Study on subset size selection in digital image correlation for speckle patterns. *Optics express*, 16(10):7037–7048, 2008.
- [122] Andrea Giachetti. Matching techniques to compute image motion. *Image and Vision Computing*, 18(3):247–260, 2000.
- [123] Wei Tong. An evaluation of digital image correlation criteria for strain mapping applications. *Strain*, 41(4):167–175, 2005.
- [124] Justin Blaber, Benjamin S Adair, and Antonia Antoniou. A methodology for high resolution digital image correlation in high temperature experiments. *Review of Scientific Instruments*, 86(3):35111, 2015.
- [125] R Harilal and Others. Adaptation of Open Source 2D DIC Software Ncorr for Solid Mechanics Applications. 2014.
- [126] Dassault Systemes. *Abaqus Analysis Users Manual, Volume IV: Elements*, 2011.
- [127] Johannes Schindelin, Ignacio Arganda-Carreras, Erwin Frise, Verena Kaynig, Mark Longair, Tobias Pietzsch, Stephan Preibisch, Curtis Rueden, Stephan Saalfeld, Benjamin Schmid, and Others. Fiji: an open-source platform for biological-image analysis. *Nature methods*, 9(7):676–682, 2012.
- [128] Philippe Thevenaz, Urs E Ruttimann, and Michael Unser. A pyramid approach to subpixel registration based on intensity. *Image Processing, IEEE Transactions on*, 7(1):27–41, 1998.
- [129] Andrew J Bushby, Kenneth M Y P’ng, Robert D Young, Christian Pinali, Carlo Knupp, and Andrew J Quantock. Imaging three-dimensional tissue architectures by focused ion beam scanning electron microscopy. *Nature protocols*, 6(6):845–858, 2011.
- [130] Ignacio Arganda-Carreras. <http://fiji.sc/skeletonize3d>.

- [131] Ignacio Arganda-Carreras. <http://fiji.sc/analyzeskeleton>.
- [132] Ignacio Arganda-Carreras, Rodrigo Fernández-González, Arrate Muñoz-Barrutia, and Carlos Ortiz-De-Solorzano. 3d reconstruction of histological sections: Application to mammary gland tissue. *Microscopy research and technique*, 73(11):1019–1029, 2010.
- [133] Ta-Chih Lee, Rangasami L Kashyap, and Chong-Nam Chu. Building skeleton models via 3-d medial surface axis thinning algorithms. *CVGIP: Graphical Models and Image Processing*, 56(6):462–478, 1994.
- [134] R T DeHoff, E H Aigeltinger, and K R Craig. Experimental determination of the topological properties of three-dimensional microstructures. *Journal of microscopy*, 95(1):69–91, 1972.
- [135] Dullien FaL. Porous media: fluid transport and pore structure. *Academic-Press, SanDiego*, 1:992, 1992.
- [136] S Parida, D Kramer, C A Volkert, H Rösner, J Erlebacher, and J Weissmüller. Volume change during the formation of nanoporous gold by dealloying. *Physical review letters*, 97(3):35504, 2006.
- [137] T Hildebrand and P Rüegsegger. A new method for the model-independent assessment of thickness in three-dimensional images. *Journal of microscopy*, 185(1):67–75, 1997.
- [138] Stephen Brunauer, Lola S Deming, W Edwards Deming, and Edward Teller. On a theory of the van der Waals adsorption of gases. *Journal of the American Chemical Society*, 62(7):1723–1732, 1940.
- [139] E Detsi, E De Jong, A Zinchenko, Z Vuković, I Vuković, S Punzhin, K Loos, G Ten Brinke, H A De Raedt, P R Onck, and Others. On the specific surface area of nanoporous materials. *Acta Materialia*, 59(20):7488–7497, 2011.
- [140] Kedarnath Kolluri and Michael J Demkowicz. Coarsening by network restructuring in model nanoporous gold. *Acta Materialia*, 59(20):7645–7653, 2011.
- [141] Anders Odgaard. Three-dimensional methods for quantification of cancellous bone architecture. *Bone*, 20(4):315–328, 1997.
- [142] Jesper Kabel, Anders Odgaard, B Van Rietbergen, and R Huiskes. Connectivity and the elastic properties of cancellous bone. *Bone*, 24(2):115–120, 1999.

- [143] Michael Doube, Michał M Kłosowski, Ignacio Arganda-Carreras, Fabrice P Cordelières, Robert P Dougherty, Jonathan S Jackson, Benjamin Schmid, John R Hutchinson, and Sandra J Shefelbine. BoneJ: Free and extensible bone image analysis in ImageJ. *Bone*, 47(6):1076–1079, 2010.
- [144] John Newman and Karen E Thomas-Alyea. *Electrochemical systems*. John Wiley & Sons, 2012.
- [145] Zhihao Hu and Kathy Lu. Evolution of Pores and Tortuosity During Sintering. *Journal of the American Ceramic Society*, 97(8):2383–2386, 2014.
- [146] Elizabeth Bullitt, Guido Gerig, Stephen M Pizer, Weili Lin, and Stephen R Aylward. Measuring tortuosity of the intracerebral vasculature from MRA images. *Medical Imaging, IEEE Transactions on*, 22(9):1163–1171, 2003.
- [147] NetworkX Developer team. <https://networkx.github.io/>.
- [148] Kaixiong Hu, Markus Ziehmer, Ke Wang, and Erica T. Lilleodden. Nanoporous gold: 3D structural analyses of representative volume elements and their implications on scaling relations. *Philosophical Magazine*, under review, 2016.
- [149] KR Mangipudi, V Radisch, L Holzer, and CA Volkert. A fib-nanotomography method for accurate 3d reconstruction of open nanoporous structures. *Ultramicroscopy*, 163:38–47, 2016.
- [150] LH Qian and MW Chen. Ultrafine nanoporous gold by low-temperature dealloying and kinetics of nanopore formation. *Applied Physics Letters*, 91(8):083105, 2007.
- [151] Yongwoo Kwon, Katsuyo Thornton, and Peter W Voorhees. Coarsening of bicontinuous structures via nonconserved and conserved dynamics. *Physical Review E*, 75(2):021120, 2007.
- [152] Markus Ziehmer, Kaixiong Hu, Ke Wang, and Erica T. Lilleodden. A principle curvatures analysis of the isothermal evolution of nanoporous gold: quantifying the characteristic length-scales. *Acta materialia*, under review, 2016.
- [153] L J Gibson. Mechanical behavior of metallic foams. *Annual review of materials science*, 30(1):191–227, 2000.
- [154] George M Pharr, Erik G Herbert, and Yanfei Gao. The indentation size effect: A critical examination of experimental observations and mechanistic interpretations. *Annual Review of Materials Research*, 40:271–292, 2010.

- [155] S Wang, Y Yang, L M Zhou, and Y-W Mai. Size effect in microcompression of epoxy micropillars. *Journal of Materials Science*, 47(16):6047–6055, 2012.
- [156] S C Tjong. Structural and mechanical properties of polymer nanocomposites. *Materials Science and Engineering: R: Reports*, 53(3):73–197, 2006.

Curriculum vitae

Family name	Hu
Given name	Kaixiong
Date of birth	27.09.1985
Place of birth	Wuhan, China

09/1991–07/1997	Primary school in Wuhan
09/1997–07/2000	Middle school in Wuhan
09/2000–07/2003	High school in Wuhan
09/2003–07/2007	Wuhan University of Technology, Bachelor of Material Processing Engineering
09/2007–06/2010	Institute of Metal Research Chinese Academy of Sciences, Master of Material Processing Engineering
06/2010–05/2012	Bekaert Shenyang Advanced Products Co., Ltd, China, Process Engineer
05/2012–01/2017	Helmholtz–Zentrum Geesthacht, PhD student in the department of Experimental Materials Mechanics

